Development of Scatter Reconstruction Algorithms to 3-Dimensional Positron Emission Tomography

by

Mohammadreza Teimoorisichani

A thesis submitted to the Faculty of Graduate Studies of
The University of Manitoba
in partial fulfillment of the requirements of the degree of

MASTER OF SCIENCE

Department of Physics and Astronomy

University of Manitoba

Winnipeg, Manitoba, Canada

Abstract

In 3-dimensional positron emission tomography (3D PET), the proportion of the detected photon coincidences arising from scatter can be very high, up to 60%. The scattered photons introduce noise and create a quantitative inaccuracy in the reconstructed images. A standard approach to scatter correction in 3D PET is to estimate the scattered coincidences and subtract them from the list of recorded events to generate a scatter-free list of events that will then be used as input for the image reconstruction step. More recently, novel techniques have been proposed in which the information carried by the scattered photons was extracted and directly used in the image reconstruction step. One of these techniques was developed and evaluated in 2D PET, and the other one was developed for 3D time-of-flight (TOF) PET systems. In this work, both algorithms were extended for use in non-TOF 3D PET systems and were qualitatively and quantitatively evaluated using simple digital phantoms and Monte Carlo (MC) simulations under ideal circumstances. Despite some promising initial outcomes, standard performance metrics of images reconstructed with each technique, representing the quality of images, was shown to be deteriorated under specified conditions. Further work is required to investigate potential benefits of the proposed algorithms for both ideal and clinical conditions.

Preface

To the best of my knowledge, the original idea of scatter reconstruction in positron emission tomography (PET) was first developed by Medical Physics group at the University of Manitoba and a research group at Siemens Healthcare, almost concurrently. The work presented henceforth is an extension of previous work, published in two papers (1, 2), to 3-dimensional non-time-of-flight positron emission tomography (3D non-TOF PET). The concept of scatter reconstruction in non-TOF PET systems was first published in (1) for the case of 2D PET, and the first scatter reconstruction method for 3D TOF PET systems was published in (2). Ideas presented in these two papers were extended and evaluated in this work for 3D non-TOF PET systems, so the papers mentioned were all different versions of this work.

I was the lead investigator in this research and all major steps including simulation and data acquisition, algorithm development, image reconstruction, and image analysis were done solely by me. Dr. Stephen Pistorius, as my supervisor, was among the very first inventors of the scatter reconstruction concept and along with Dr. Harry Ingleby, as my co-supervisor, contributed to concept formation of this work and revising this dissertation. Timothy Van Beek also kindly provided his ray tracing code used in the proposed image reconstruction algorithm, and contributed to the C programming in the early stages of this work. Hongyan Sun, as the main developer of scatter reconstruction idea in 2D non-TOF PET, also contributed to technical issues in 3D scatter reconstruction. Finally, Bryan McIntosh offered me his C code developed for data extraction from GATE (a Monte Carlo simulation package) output files.

Table of Contents

List of Tables

List of Figures

List of Acronyms

2/3/4D: 2/3/4 Dimensional

AC: Attenuation Correction

AD: Alzheimer's Disease

BGO: Bismuth Germanium Oxide

b-LOR: Broken-Line of Response

BP: Back Projection

CRC: Contrast Recovery Coefficient

CT: Computed Tomography

eV: Electron Volt

FBP: Filtered Back Projection

FDG: ^{18}F-Fluorodeoxyglucose

FORE: Fourier Rebinning Algorithm

FOV: Field-of-View

FWHM: Full Width Half Maximum

LLD: Lower Level Discriminator

LM: List-Mode

LOR: Line of Response

LSF: Line Spread Function

LSO: Lutetium Oxyorthosilicate

LYSO: Lutetium-Yttrium Oxyorthosilicate

MAP: Maximum a Posteriori

MC: Monte Carlo

MFP: Mean Free Path

ML-EM: Maximum Likelihood Expectation Maximization

MRI: Magnetic Resonance Imaging

MTF: Modulation Transfer Function

NM: Nuclear Medicine

OPL-EM: One-Pass List-Mode Expectation Maximization

OS-EM: Ordered-Subset Expectation Maximization

PET: Positron Emission Tomography

PMT: Photomultiplier Tube

PSF: Point Spread Function

PVE: Partial Volume Effect

RC: Resolution Recovery Coefficient

ROI: Region of Interest

SOR: Spill-Over-Ratio

SPECT: Single Photon Emission Computed Tomography

SSRB: Single-Slice Rebinning Algorithm

TCA: Two Circular Arcs

TOF: Time-of-flight

ULD: Upper Level Discriminator

US: Ultra Sound

VOI: Volume of Interest

Acknowledgements

Learning a lot more than what I knew two years ago is just a part of what I have gained during the past two years. I have met a lot of great people who kindly assisted me coping with my new life in Winnipeg and would like to thank them all. I would like to offer my sincere gratitude to my supervisors Dr. S. Pistorius and Dr. H. Ingleby, who continuously supported me, believed in me, have inspired me to continue my work in this field, and have enlarged my vision of science. It has been a great pleasure working with them, and I deeply appreciate their cooperation in providing me the vast opportunity of joining their research group.

I am also grateful to the faculty and staff of Medical Physics group who helped me throughout the research by patiently answering my questions and consulting with me. I would like specifically to thank Dr. A. Goertzen and Dr. D. Rickey for their very helpful suggestions and consultations. I also owe special thanks to Dr. A. Reader for his constructive critiques and comments on my work, T. Van Beek for sharing his ray tracing code generously and his continuous support, my cooperative lab mates, specially Bryan and Hongyan, for their technical supports and sharing thoughts with me, and my friend, Roiy for his enduring moral support.

I would also like to take this opportunity to express my sincere thanks to some special people in my life who showed me the true meaning of life and love and without them I could not accomplish my success. My parents with their constant encouragement and support, and my girlfriend, Fereshteh, who could and did change my new cold home into a very happy one.

Finally, I gratefully acknowledge financial supports from CancerCare Manitoba Foundation and the University of Manitoba.

Dedication

To my beloved parents

1. Chapter One: Introduction

1.1 Background

Medical imaging techniques such as X-ray radiography, computed tomography (CT), and ultrasound (US) were developed with the aim of observing anatomical structure. These modalities do not provide information on the metabolism and functionality of the organs. Functional imaging, on the other hand, provides information regarding metabolism. The evolution of functional imaging started with nuclear medicine (NM) techniques in the 1960s. The first tomographic images with radionuclides, which were the basis for the current well-known technique of positron emission tomography (PET) were presented in 1972 (3). Currently, PET is one of the most valuable techniques in functional imaging.

To acquire PET images, short-lived positron emitting radionuclides are used. These radionuclides are incorporated either into compounds normally used by the body such as glucose, water, or ammonia, or into molecules that bind to receptors (radiotracers). The radiotracer or radiopharmaceutical is injected intravenously into the patient and disperses through the body while decaying and emitting positrons. The decay process of the positron emitter radionuclide X can be shown as

$$ {}^{A}_{Z}X \rightarrow {}^{A}_{Z-1}Y + \beta^{+} + \nu \tag{1.1} $$

where A is the atomic mass, Z is the atomic number, Y is the daughter atom, β^{+} is the positron, and v is a neutrino.

The radiotracer starts accumulating in the organ(s) of interest and after a prescribed uptake period, the biodistribution of the tracer is evaluated by imaging with a PET scanner. For instance, ^{18}F-fluorodeoxyglucose (FDG) is a common radio-pharmaceutical used in PET and is a glucose molecule bound with the positron-emitter radioisotope ^{18}Fluorine (^{18}F). After administration of FDG, tissues with higher rates of glucose metabolism take up more FDG and, therefore, any abnormal metabolism (such as cancerous cells that have a higher rate of metabolism than normal cells) can be detected in the image. FDG PET scan is currently a very common technique in neurology and oncology.

A positron, as an anti-particle of the electron, has the same mass as an electron (9.11×10^{-31} kg) and an electric charge of 1.6×10^{-19} Coulomb (C). After the creation of a positron, it usually travels a short distance and when it comes to rest it absorbs a nearby electron. The distance, which is usually around a few millimeters for medically important positron emitters, depends on the released energy in positron emission process. The electron-positron pair forms a momentary atom called "positronium" that has the positron as its nucleus and has a lifetime of about 10^{-10} sec. The positron and electron then combine in an annihilation process and as a result of the positron-electron annihilation, two 511 kilo electron volt (keV[1]) photons are generated at almost 180 degrees to each other. The back-to-back emission of the annihilation photons is essential for the conservation of energy in the annihilation process for a stationary electron-positron pair. Since sometimes both particles are moving at the time of annihilation the photons may be emitted at a slightly different angle than 180 degrees (4). Although the annihilation photons do not have a nuclear origin, they are sometimes called annihilation gamma rays (γ-rays) which is the case in this dissertation as well. Figure 1-1 shows a schematic representation of the production of back-to-back photons in an annihilation process.

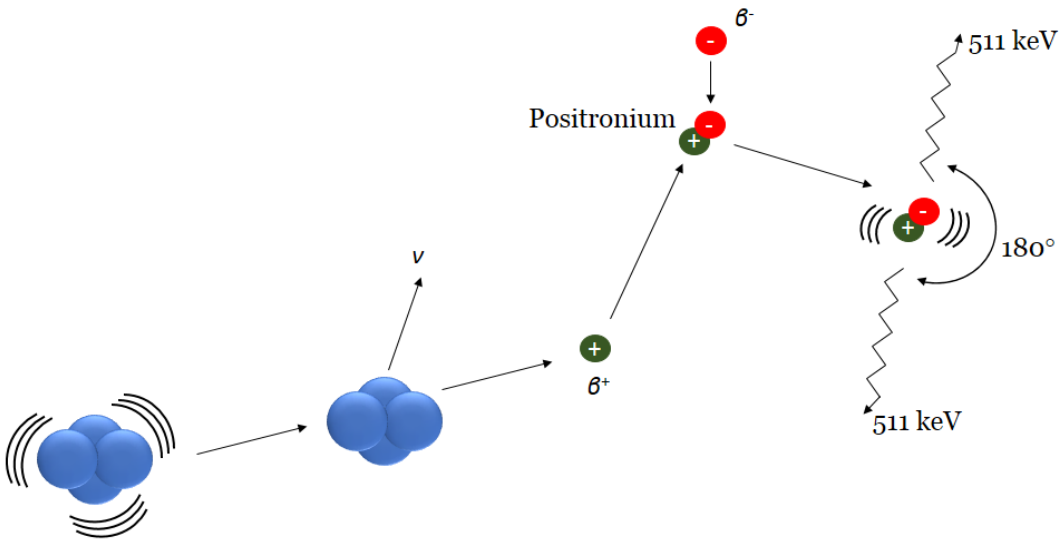

Figure 1-1. A schematic illustration of the production of an annihilation photon pair. A positron emitting nucleus (shown in blue) emits a positron (shown in green) and a neutrino. After the positron loses its kinetic energy it absorbs an electron (shown in red) and forms a positronium. The positronium then undergoes an annihilation and as a result of this phenomena two back-to-back photons are generated.

[1] 1 eV = 1.602×10^{-19} Joules

The PET system functions by detecting the pair of 511 keV back-to-back photons using a ring of photon detectors around the patient. Indeed, for each detected photon pair a straight line between two corresponding detectors represents possible positions of photon annihilation and this line is called the line of response (LOR). The process of recording a pair of back-to-back annihilation photons is called a coincidence in PET. Figure 1-2 illustrates how a PET machine works and shows an example of an LOR. Hardware structure, clinical application, and image reconstruction in PET will be discussed further in the next sections.

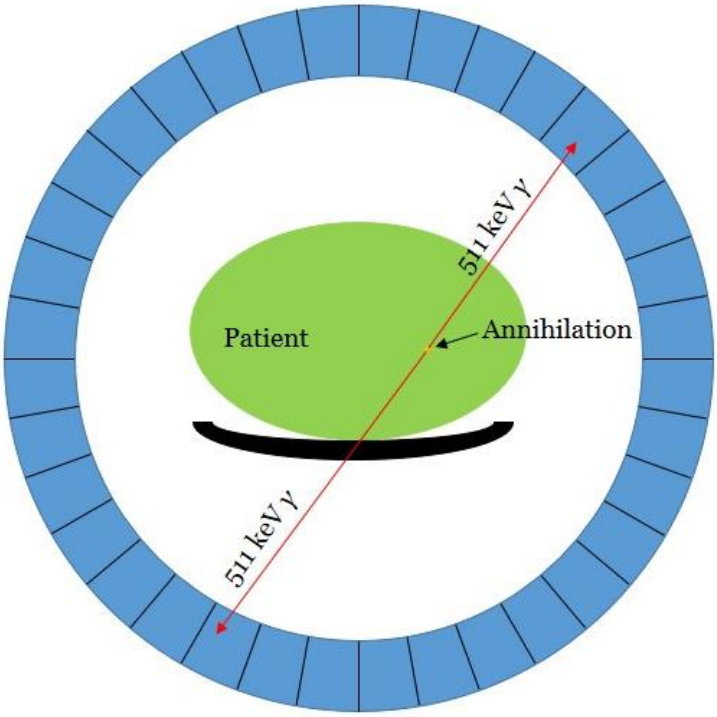

Figure 1-2. A sample recorded coincidence in PET. A pair of annihilation photons are shown in red, and a ring of PET detectors are shown in blue around the patient (green). The red lines represent the LOR associated with this coincidence.

One of the most important applications of PET is quantitative PET imaging, in which the concentrations of the administrated radio-pharmaceutical in different tissues are calculated. Quantitative PET imaging is now widely used in disease diagnoses, such as Alzheimer's Disease (AD) and evaluation of the tumor response to a treatment method in oncology (5). The key for accurate quantitative PET imaging is performing compensations for image degrading factors occurring during PET image acquisition (6). These factors are explained in Section 1.2.5 in detail. One of

the most important phenomenon that needs compensation happens when one (or both) of emitted annihilation photons interacts with a free (or lightly-bound) electron inside the body and changes its path with a lower energy. This phenomenon is called “Compton scattering” and will be discussed in the Section 1.3.2. Compton scattered photons will result in detection of incorrect LORs that lead to inaccuracy in the final reconstructed images. The situation where only one of the emitted photons undergoes a single Compton scattering is called a single-scatter coincidence and if more than one scattering event occurs for one or both annihilation photons, it is called a multiple-scatter coincidence. Figure 1-3 shows how a single-scatter coincidence introduces a false LOR.

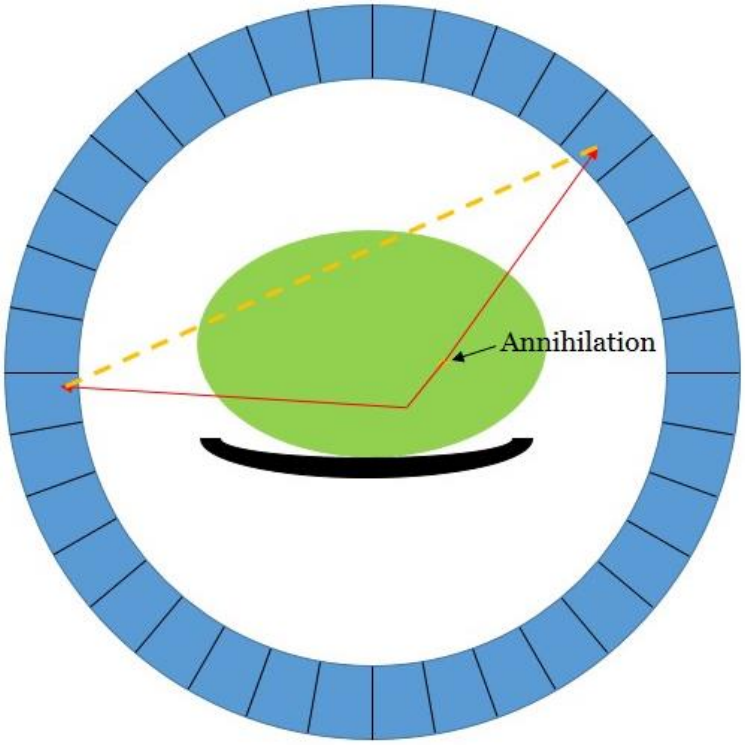

Figure 1-3. A sample single-scattering coincidence. Scattering of annihilation photons after emission can result in a false LOR (shown as the dashed line) which could be very far from the true annihilation position.

The main attempt to reject both the single and multiple scattered coincidences is done by restricting the accepted energy window of the recorded photons, however, due to the limited energy resolution of current PET detectors, a significant fraction of recorded coincidences comprises scattered photons. The fraction of recorded scattered coincidences can be as high as 20% in 2D

and 60% in 3D PET (7). Scattering is a serious problem, especially for 3D abdomen and pelvis PET imaging where the annihilation photons need to travel a relatively large path inside the body to exit the patient and reach the detector ring (7, 8). Importantly, in regular 3D PET imaging, single-scatter coincidences are shown to be 50% to 80% of the recorded scattered coincidences (9).

The current approach to compensate for scattered coincidences is to apply a scatter correction method. In several scatter correction techniques, scatter components (or only single-scatter coincidences) are estimated and then subtracted from the total recorded coincidences (9-13). These methods try to reduce the scattered component of total recorded photons and thus provide a less noisy set of data as an input to the image reconstruction step. Other scatter correction methods incorporate estimation of the scattering pattern at each angle in the forward-projection part of an iterative reconstruction algorithm (discussed in Section 1.4.2) (8, 14, 15). Scatter correction methods are not discussed in this dissertation in detail, and a comprehensive review of available scatter correction techniques in PET can be found in (8, 16).

This research concentrates on handling the single-scattered photons in a more efficient way than current scatter correction methods. In this work, the information carried with single-scattered photons (energy and detection position) is extracted and used in the image reconstruction step. Therefore, the proposed algorithm is not a new scatter correction technique, but is rather a new 3D PET image reconstruction technique which takes advantage of single-scattered photons rather than treating them as nuisance signals. This will be referred to as "scatter reconstruction."

The concept of scatter reconstruction for 2D PET has been previously investigated (1), however, extension of the algorithm into 3D makes the algorithm more realistic since scattering is a major problem in 3D PET (7). The difficulty in the extension to 3D is in complexity of the physical and mathematical side of the problem. Furthermore, extension to 3D needs time-efficient algorithms that would be capable of keeping the reconstruction time to a reasonable level. In this research, the proposed 3D scatter reconstruction will be incorporated with a fast iterative reconstruction algorithm which will be explained in Section 1.4.2. In addition to the extension of the previously developed scatter reconstruction technique from 2D to 3D, a new algorithm will be proposed which is based on the work done by (2). In (2), a different method for 3D scatter reconstruction in PET is proposed which uses time-of-flight (TOF) information along with the scattered pho-

tons' energy and detection positions (these concepts will be reviewed in Section 1.2). In this study, this method will be generalized to a situation where TOF information is not available, and the results will be compared with the results from the extension of previously developed algorithm in our group. Furthermore, attempts to reduce the reconstruction time will be explained including introduction of a novel 3D ray-tracing method for curved lines or surfaces.

1.2 Positron Emission Tomography (PET)

In this section, a brief review on the history of various NM techniques and specifically PET is explained, followed by a review on hardware structure, clinical applications, and limitations of PET.

1.2.1 Basics of PET

An NM study usually involves the injection of a gamma ray emitting or positron emitting radioisotope in the form of a radiopharmaceutical or radiotracer. There are two general categories of nuclear medicine imaging techniques. Single photon emission computed tomography (SPECT) was introduced in the 1970s (17, 18) and detects photons emitted from gamma emitting radionuclides. In SPECT imaging a relatively large photon detector (or two or three), known as a gamma camera, is rotated around the patient to record photons from various angles around the patient. The obtained image at each angle (view) is called a projection. By combining data for each projection, a set of raw data for each slice is gathered in a data set called a "sinogram." The sinogram is then converted to a tomographic image by applying a mathematical algorithm called "filtered back projection (FBP)" or by using an iterative reconstruction method (19). The reconstruction algorithms will be explained in detail in Section 1.4. Having one or two flat detectors make SPECT systems capable of image acquisition in planar mode, which provides 2D images of the patient from various angles. For many years, SPECT was the main modality in NM departments and is still in use, mainly in the form of a hybrid imaging system, SPECT/CT.

Although imaging using positron emitting radioisotopes was discovered before the invention of SPECT (3), PET systems were introduced into clinics later than SPECT systems. The advantages of PET over SPECT quickly became apparent to physicians and PET is now widely used for functional imaging. One of the advantages of PET is that radioisotopes associated with PET usually have a short half-life (for instance ^{18}F has the half-life of about 110 minutes), whereas

SPECT radioisotopes have a longer half-life (Technecium-99m or ^{99m}Tc and Iodine-131 or ^{131}I have half-lives of approximately 6 hours and 8.02 days, respectively). The short half-life of PET radioisotopes can reduce the risk of radiation for people who are in contact with patients after they leave the imaging clinic. PET systems also have higher sensitivity than SPECT systems, the resolution of the image is higher, and PET enables the opportunity of functional imaging at molecular level (20). Introduction of the first whole-body multi-modality PET/CT in 2000 (21) was a major milestone in the history of NM. Nowadays, PET and PET/CT systems play a vital role in cardiology, neurology, and oncology (5) and the power of PET lies in its ability to provide exquisitely sensitive images of biological processes at the molecular level. Figure 1-4 shows a sample clinical PET/CT image obtained from an FDG PET scan.

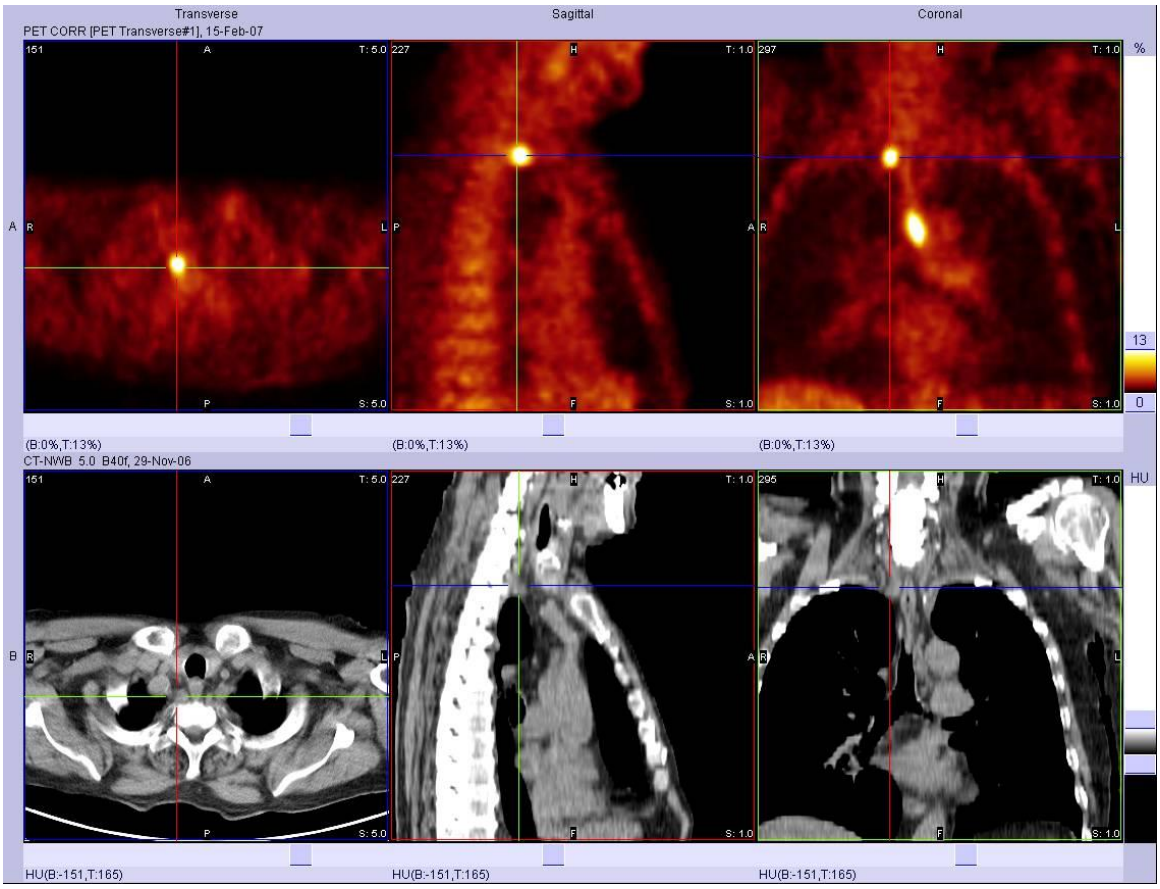

Figure 1-4. An example of a whole-body FDG PET/CT scan. A PET/CT scan of a 10 year old male revealed metastatic disease at upper paraesophageal lymph nodes. The top row shows co-registered PET and CT images and the bottom row shows the corresponding CT images. From left to right, trans-axial, sagittal, and coronal slices are shown. Image courtesy of the Great West Life PET/CT Center.

As explained in the previous section, the basis of PET imaging is detection of back-to-back annihilation photon pairs with a detector ring around the patient. It is worth mentioning that although annihilation photons are detectable by conventional SPECT systems, SPECT architecture is not well optimized for 511 keV photons (22). The detection rate is insufficient for clinical applications and SPECT systems would require a relatively inefficient high-energy collimator. Most importantly, SPECT systems would not take advantage of the unique property of 180° back-to-back photons. The architecture of PET systems, however, is optimal for the pair of 511 keV back-to-back photons (4).

PET sites usually include a small cyclotron (cyclotron is a charged particle accelerator) in order to produce the required radioisotopes for PET imaging, such as ^{18}F. Once ^{18}F is produced, it will be synthesized into ^{18}F-FDG and injected to the body. A regular whole-body PET scan with FDG is usually done with administration of 370-740 MBq[2] activity and takes 30-60 minutes to complete (23).

1.2.2 Hardware Structure

The main component of a PET system is the detector ring around the patient. Detectors in PET are scintillator crystals such as NaI(Tl) (a crystal structure of sodium iodide doped with thallium), LSO (lutetium oxyorthosilicate), LYSO (lutetium-yttrium oxyorthosilicate) and BGO (bismuth germanium oxide). These crystals are arranged into a pixelated block to form a block detector for PET scanners. The size of each crystal cell is usually on the order of a few square millimeters along the gantry axis (Z-axis) by a few centimeters maximum along the perpendicular direction and a set of detector blocks is used to form a cylindrical detector array around the patient. Table 1-1 shows some common scintillation detectors and their important properties[3] (24).

Table 1-1. Properties of some commonly used scintillators in PET detectors.

Scintillators	Effective atomic number (Z)	Density (g/cm^3)	Scintillation decay time (ns)	Photon yield (per keV)
NaI(Tl)	51	3.67	250	38
BGO	74	7.13	300	6
LSO	66	7.40	40	29
$LaBr_3$	47	5.3	16	61

[2] MBq or Mega Becquerel is the standard unit for measurement of radioactivity. Each Becquerel is equal to one disintegration per second.

[3] LSO: Lutetium oxyorthosilicate (Lu_2SiO_5:Ce). $LaBr_3$: $LaBr_3$:Ce, Lanthanum bromide.

When annihilation photons enter the scintillator crystal, they interact with the electrons in the crystal by photoelectric interaction or Compton scattering (explained in 1.3) and excite electrons. This causes the excited electrons to move to the conduction band, and when returning to the valence band (ground state energy) they release the energy difference in the form of an optical photon. The values in the last column of the Table 1-1 shows the number of optical photons generated per 1 keV energy absorbed in the crystal. The crystals usually need to be handled with extra care as they are fragile and very sensitive to room temperature. Crystals with higher density, higher effective atomic number, higher photon yield, and lower scintillation decay time are preferred, however, normally the choice of the proper detector for an arbitrary PET system depends on the use and required features of the system.

The scintillator crystals are joined with a photomultiplier tube (PMT) to detect the output optical photons. A PMT consists of a light-sensitive photocathode, followed by a series (usually around 10) of metallic electrodes known as dynodes, and an anode at the other end. The photocathode is facing the crystal and is usually an alloy of cesium and antimony or other bialkali metal that releases electrons after absorption of light photons. A high voltage (around 1000 V) is applied between the photocathode and the anode in steps of 50-150 V between dynodes. Dynodes are coated with materials such as cesium that makes them capable of liberating secondary electrons after interactions with the initial set of electrons. In this manner, the total number of electrons exponentially grows after striking each dynode, and the total number of 10^7-10^8 electrons is produced when the electrons reach the anode at the other end of PMT (24). The pulse is then delivered to the preamplifier and the height of this pulse is related to the number of optical photons detected by the PMT and in turn to the energy deposited in the crystal by the incident photon. Figure 1-5 shows how a basic NaI(Tl) scintillation counter and PMT work.

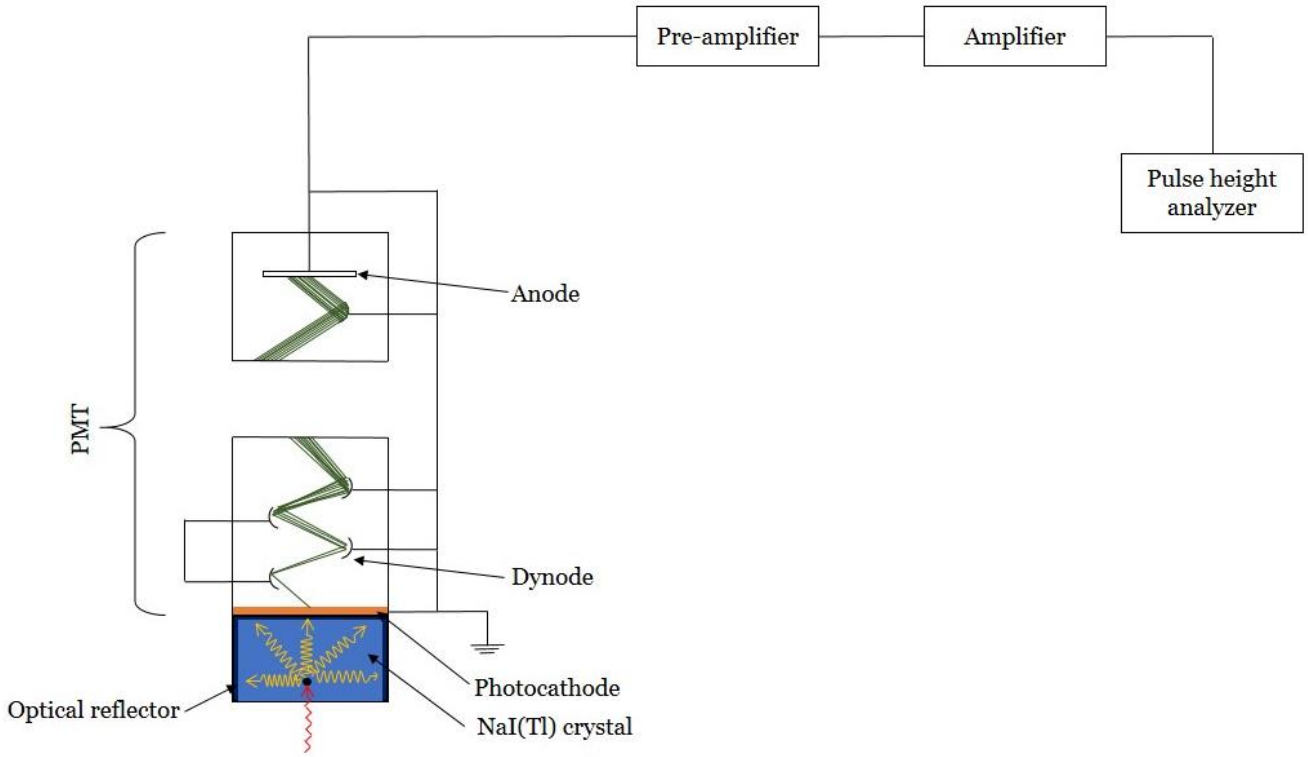

Figure 1-5. Schematics of a basic NaI(Tl) scintillation detector coupled with a PMT. A gamma ray (red arrow) is absorbed by NaI(Tl) crystal (shown in blue) and optical photons (shown in yellow) are generated in the crystal. Photocathode (orange) releases electrons by absorption of the optical photons and the released electrons (shown in green) are multiplied after striking each dynode. The output electron is then amplified through the preamplifier and amplifier and the height of the final pulse represents the energy of the gamma ray.

The most common detector arrangement in PET consists of cut block scintillation crystals coupled with PMTs (usually 4 PMTs). The channels in the crystal are filled with opaque material so that the light from scintillation events cannot spread between sections but travels toward the PMTs. Current full multi-ring PET scanners have about 200 to 400 blocks that contain 10,000 to 20,000 crystals joined with 500 to 1000 PMTs (23). Even though the number of PMTs is far less than the number of individual crystal elements, it is still possible to attribute each light pulse to a particular crystal element for localization by comparing the pulse heights in each of the PMTs based on modified Anger logic (25). Figure 1-6 shows a diagram of a PET scintillation block detector with connected PMTs.

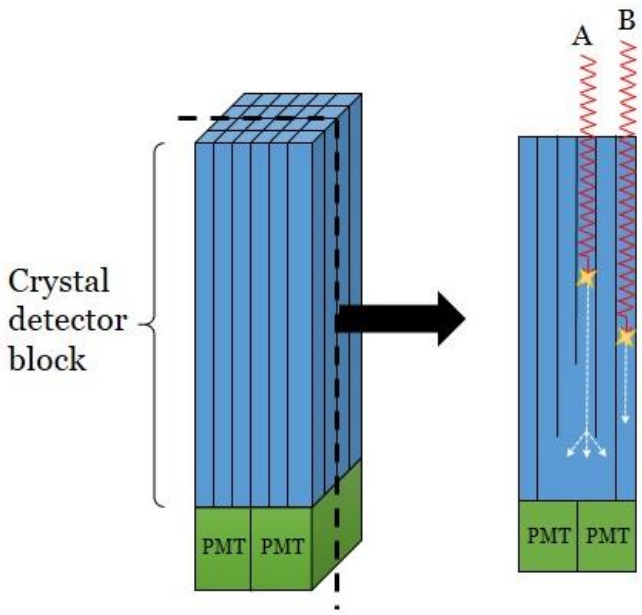

Figure 1-6. PET scintillation block detector. Crystal detectors are cut to different depths and filled with opaque material. The different depths of cut allows localization with only four PMTs. For instance, photon A is detected in a central shallow cut detector and the output light photons (white dashed lines) will be detected by several PMTs, whereas, photon B is interacting with a detector element near the edge of the block and the output light is seen by only one PMT.

In contrast with conventional gamma-cameras and SPECT systems, PET does not require a physical collimator. This is because both annihilation photons are detected almost simultaneously. This unique property of PET is called "annihilation coincidence detection", and requires the electronics to attach a time stamp to each recorded photon. Typically, the precision for the time stamp is around 1-2 nanoseconds (ns). The coincidence processor compares the time stamps for two detected photons travelling in opposite directions and usually accepts the pairs that have the time difference of less than 6-12 ns (23).

In theory, it is possible to determine the exact location of photon annihilation along each LOR using the time stamps and equation (1.2).

$$\Delta d = \frac{\Delta t \times c}{2} \tag{1.2}$$

where c is the velocity of light (3×10^{10} cm/s), Δd is the difference in the location the annihilation event with the midpoint between the two detectors, and Δt is the difference in arrival times of the photons. According to the equation (1.2), to achieve a depth resolution of 1 cm would require

timing resolution of about 66 picoseconds (ps). Achieving this level of timing resolution requires extremely fast scintillation crystals and careful design of electronic components and connections. With current technology and advances in scintillation crystals and electronic components, the timing accuracy at the level of a few hundred picoseconds is feasible. Using the information from the time stamps constrains full length LOR to within a few centimeters and this increases the signal-to-noise ratio (SNR) in images reconstructed with timing information compared with images reconstructed without timing information (4). PET machines, which use time stamps in their image reconstruction algorithm are called time-of-flight (TOF) PET.

Two important common performance parameters in PET (and generally in gamma cameras) are spatial and energy resolution. The spatial resolution of a PET system refers to the measured size (full-width at half-maximum or FWHM) of the image's profile for an impulse function (point source). Spatial resolution in PET is a function of crystal size and properties and architecture of the PET scanner. In a typical scintillator gamma camera, energy resolution is defined as the ability of the system to distinguish between the photopeaks of different radionuclides. In a PET system, energy resolution can be explained as the ability to separate different light photons from various incident gamma rays with different energies. Mathematically, energy resolution is defined as the ratio of the FWHM of the full energy peak to the energy value at the full energy peak maximum. The energy resolution in a PET system depends largely on statistical fluctuations in the number of light photons collected from a scintillation event. Therefore, good light collection is a prerequisite for good energy resolution. Spatial resolution and energy resolution in a typical clinical PET scanner is roughly in the range of 4 mm to 10 mm and 10% to 35%, respectively (24, 26, 27).

In PET, the energy window is set so that photons with energy below a certain energy (lower level discriminator or LLD) or higher than a certain energy (upper level discriminator or ULD) are rejected. Thus, only coincidences with both photons within that energy window (LLD to ULD) are recorded. This energy window could be set manually and varies for different type of scanners and different imaging protocols, however, a typical range of 350 – 650 keV is commonly used for a whole-body FDG PET scan (sometimes the LLD varies to up to 440 keV). The LLD rejects many scattered photons but cannot avoid all the scattered photons since many low-angle scattered photons have their energy close to 511 keV. Unscattered photons may deposit only a part

of their energy in the crystal (if they scatter within the crystal rather than undergoing photoelectric absorption), hence the need for a trade-off between sensitivity to unscattered photons and scatter rejection (28). On the other hand, the ULD causes rejection of events in which more than one photon is incident on the block detector at the same time.

1.2.3 Clinical Applications

As pointed out before, PET has various clinical applications and plays an important role in oncology, neurology, and cardiovascular disease. FDG is the most common choice for many types of clinical scans. The most widespread application of PET is detection and staging of cancer tumors, as many pathologic conditions may cause regional alterations in glucose metabolism that are detectable in an FDG PET scan. FDG in conjunction with blood flow tracers such as ^{13}N-ammonia is also used to evaluate myocardial viability for patients with coronary artery disease. PET is also used for various brain studies of neurodegenerative diseases such as Alzheimer's Disease (AD), Parkinson's Disease and the evaluation of psychiatric disorders (5).

1.2.4 Limitations

There are basic limitations associated with a clinical PET scanner. The information acquired with a PET scanner suffered from a lack of anatomical information, and this led to the invention of PET/CT. PET/CT is now widely accepted in imaging departments, however, it increases patient radiation dose since both PET and CT use ionizing radiation. To overcome PET/CT limitations, replacement of CT with MRI has been investigated (29, 30). Although PET/MRI resolves many of the drawbacks of PET/CT, it still requires further improvement to completely to replace PET/CT systems in clinics. A PET site, regardless of whether it uses a stand-alone PET scanner or a hybrid PET/CT or PET/MR scanner, needs a small cyclotron to produce the essential radioisotope for the PET scan and this makes PET an expensive modality. Furthermore, PET has poor sensitivity and/or specificity for some disease processes such as detection of metastatic prostate cancer (31). PET also has limitations with respect to small lesions due to its inherent limited spatial resolution. Although it is not possible to determine a definite cut-off for clinical PET systems, in some cases PET may be limited in detection sensitivity for lesions smaller than 1 cm (31).

1.2.5 Image Degrading Factors

There are several physical degrading factors that can affect the quality of images produced by a PET system, some of which can be compensated for to achieve more accurate quantitative PET images. These factors are summarized as follows.

1.2.5.1 Scatter

In a PET scan, not all of the detected coincidences are true coincidences. As briefly explained in Section 1.1, scattered photons may produce LORs that are far from the true location of photon annihilation (see Figure 1-3) and degrade image quality by introducing false LORs. The physical explanation and kinematics of photon scattering will be explained in Section 1.3.2.

Defining a coordinate system as shown in Figure 1-7 (with the center of the coordinate system at the PET system isocenter), a coincidence may be recorded in detectors with the same value of Z or identical XY plane (which is called in-plane coincidence) or different value of Z (out-of-plane coincidence).

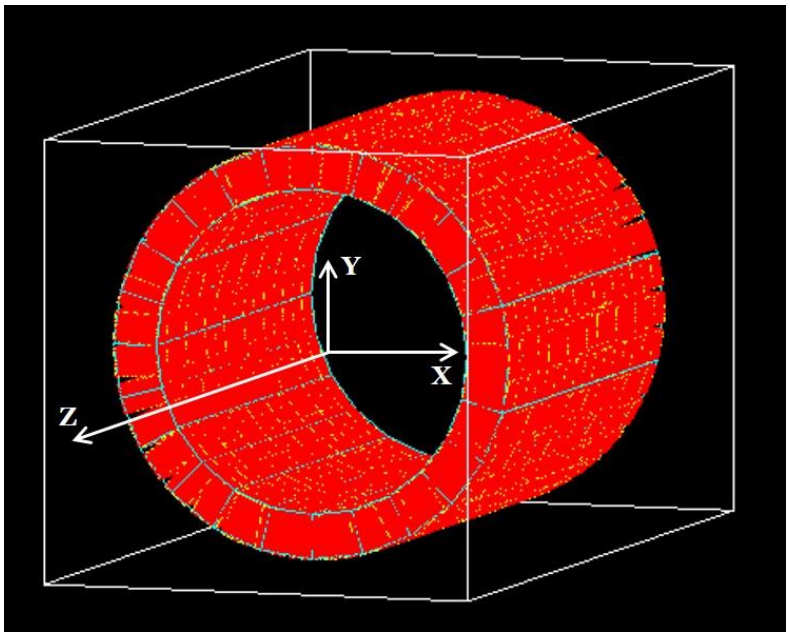

Figure 1-7. XYZ Coordinate definition in a PET system.

Scattering may change the type of each potential coincidence, and a photon in an in-plane coincidence may undergo scattering and change its direction to a different detector with a different Z value. Therefore, one way to avoid detection of scattered photons is physically to limit the system to detect in-plane coincidences only. Flat, ring-shaped lead or tungsten septa are used to re-

duce the number of out-of-plane coincidences. Using septa allows the PET system to detect coincidences that happen between the two detectors in the same XY plane and only scatter photons that scattered in the same XY plane might be detected. Figure 1-8 represents a schematic illustration of a PET system with septa.

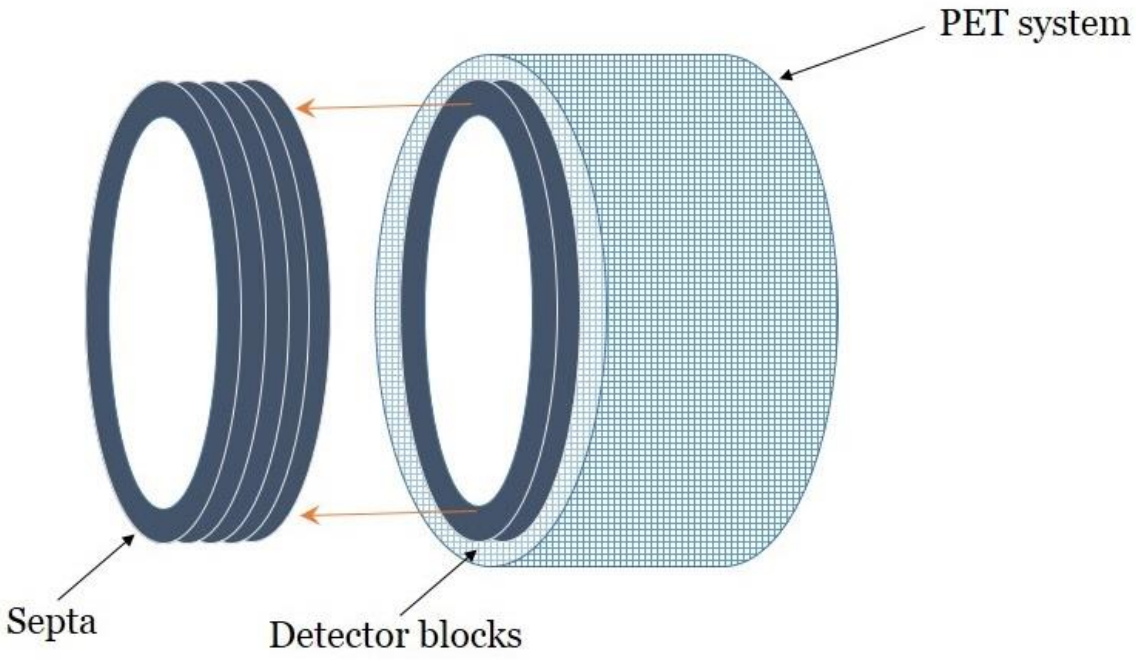

Figure 1-8. A PET system with septa. Flat, ring-shaped lead or tungsten septa are shown in dark blue.

The septa limit the PET system to gathering information in 2D only. PET acquisition with septa has the advantages of minimizing the effects of radiation originating outside the field-of-view (FOV) and random events (to be discussed later) beside reducing scatter from 30%-60% to 10%-20% (32). Figure 1-9 shows the basic difference between PET systems with and without septa.

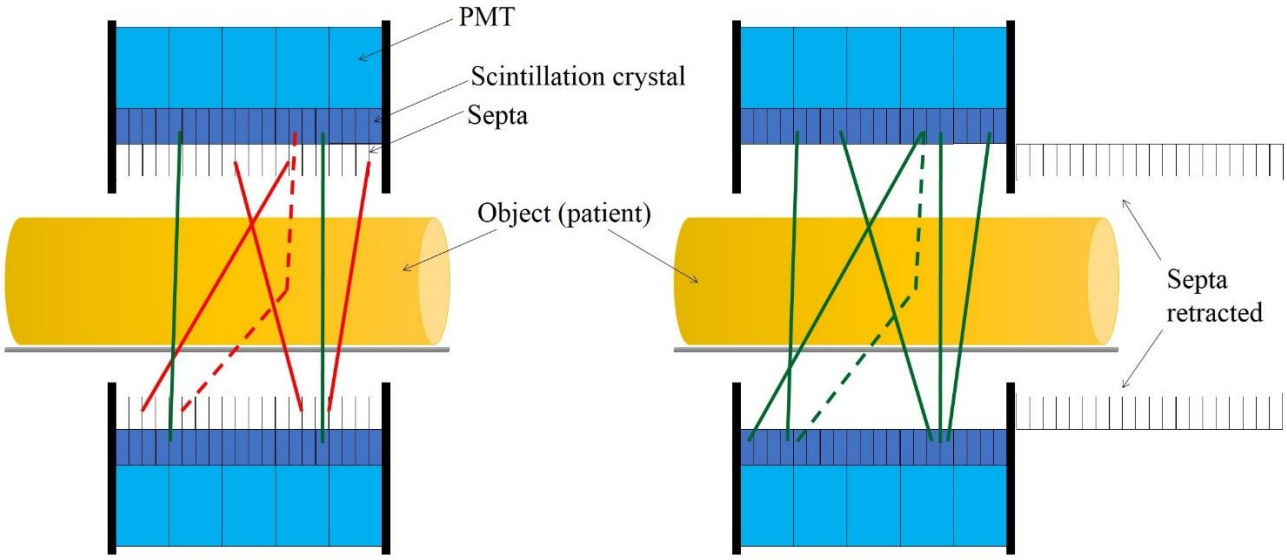

Figure 1-9. PET system with and without septa. Left image shows a PET system with septa. The coincidences that have their both annihilation photons in the same XY plane are detected (green lines), whereas out-of-plane coincidences (red lines) and scatter coincidences (dashed red line) are not detected due to the presence of the septa. Right image shows the PET system with septa retracted (fully 3D acquisition mode). The LORs that were not detected in the right image (red lines), including the scattered coincidence (dashed red line), now reaches detector and are recorded.

Using septa reduces PET sensitivity significantly due to rejection of many out-of-plane coincidences. Nowadays, with advances in image reconstruction and scatter correction techniques, fully 3D PET systems (septa-retracted for PET systems with septa) are the most widely used technique in clinical and pre-clinical PET.

There are various scatter correction algorithms for PET. The well-known convolution-subtraction method (10) was among the first algorithms proposed for scatter correction in PET and was implemented in commercial PET systems. The algorithm is based on estimation of the scatter component and subtraction from the recorded data to generate a scatter-free raw data for the image reconstruction step. This type of scatter correction technique was mainly used in analytical image reconstruction techniques. Model-based scatter correction algorithms for PET was introduced in 2000 (33) and remains the most widely used scatter-correction algorithm in clinical PET systems as of 2007 (8). These techniques directly estimate scatter components of the acquired raw data, using preliminary PET emission and transmission images and the Klein-Nishina formulation (explained in Section 1.3.2) or using Monte Carlo (MC) simulation. Implementation of such techniques for single-scatter correction is well established in the literature (9, 14, 33-35).

Statistical image reconstruction techniques[4] provide the opportunity for modelling physical aspects of image acquisition in the image reconstruction such as Poisson statistics of radioactive decay, attenuation, scatter, and the geometry of the PET system. Iterative reconstruction-based scatter correction approaches have been developed by incorporating the estimated scatter component in the forward projector of an iterative image reconstruction technique as an additive term (see Section 1.4.2). Scatter estimation in these algorithms might be done analytically or by using the transmission scan image and MC simulation (36).

1.2.5.2 Attenuation

In PET, both annihilation photons should be detected within the acceptable pre-set energy window to record a coincidence. In reality, photons might interact with atoms inside the body and either scatter or be completely absorbed by electrons inside the body by the photoelectric effect (explained in 1.3.1). The probability of photon interaction with matter increases exponentially as the thickness of the object increases. Therefore annihilation pairs generated close to the midpoint of the patient have a lower chance of detection in comparison with photons generated close to the surface of the patient. This effect results in a larger number of photons being detected as the annihilation position moves from the center of patient towards the patient's skin. Figure 1-10 shows the effect of attenuation on reconstructed images of a uniform phantom with the diameter of 14 cm filled with 370 MBq of FDG.

[4] In this dissertation the term "iterative image reconstruction", "statistical image reconstruction", and "statistical iterative image reconstruction" are considered equal and used interchangeably.

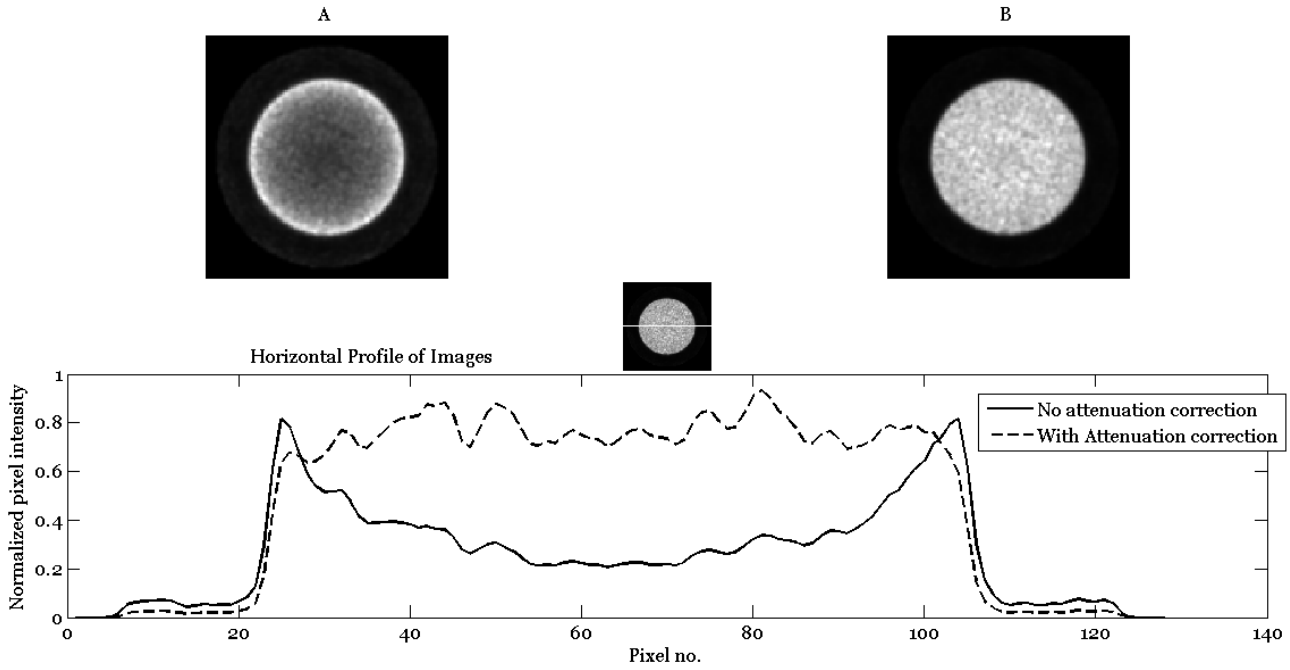

Figure 1-10. The effect of attenuation on PET images. Sample reconstructed images of a uniform cylindrical phantom with diameter of 14 cm filled with 370 MBq FDG when compensation for attenuation is not applied (A) and is applied (B). Mid-image horizontal profile of the reconstructed images (shown in the image above the graph) are drawn in the plot.

In order to perform attenuation correction (AC), an attenuation map of the object is required. This map represents estimated attenuation coefficients of the object for each voxel (3D pixel) for the photon energy of 511 keV and must be well aligned with the PET image. A convenient and reliable way of generating a patient-specific attenuation map is to derive the attenuation map from the CT images of patients. Since X-ray photons in CT have a polyenergetic spectrum, a simple piece-wise linear transformation is used to derive the attenuation map for 511 keV photons from the CT images (37). Stand-alone PET systems, however, might use electronically windowed rotating positron emitter radioactive rod sources, usually Germanium-68/Gallium-68 (^{68}Ge/^{68}Ga) or a rotating point source, usually Cesium-137 (^{137}Cs), to generate the attenuation map for each patient (38).

Attenuation correction was historically done by Chang's method for NM images (39). In Chang's method, a uniform attenuation map is used to calculate an attenuation correction coefficient for each pixel. The correction coefficient is calculated by averaging the attenuation over all different views and multiplying by each pixel within the object after reconstruction. Therefore,

this method is a post-processing algorithm (to be done after image reconstruction) and is compatible with analytical reconstruction algorithms. With the introduction of iterative reconstruction techniques, however, more sophisticated AC algorithms were introduced. The AC algorithms in this category take advantage of a patient-specific attenuation map in order to model the attenuation for each angle or view. The attenuation models are then incorporated with statistical image reconstruction algorithms (40).

1.2.5.3 Noise

The number of radioactive decays over a period of time obeys Poisson statistics. Therefore, the decay of the injected radiotracer or radiopharmaceutical in an NM study is a Poisson process. The stochastic nature of radioactive decay is indeed among the first factors for noise in all NM modalities, including planar gamma-camera images, SPECT, and PET. Although PET has higher sensitivity in comparison with gamma-cameras and SPECT, and records a higher number of coincidences ("counts") in a clinical scan, noise in 3D PET is much more complex than other NM modalities. This is because the noise in PET comes from a variety of other sources (in addition to the statistical nature of radioactivity decay), such as the reconstruction algorithm, random, and scatter coincidences. Since iterative reconstruction algorithms have the ability to deal with noise, they are favored for PET.

1.2.5.4 Random Coincidences

In a PET scan, single photons from different annihilation events might reach the detector within the acceptable coincidence time window and generate an LOR that does not correspond to the true location of either annihilation. Figure 1-11 shows the basis of different types of coincidences in PET.

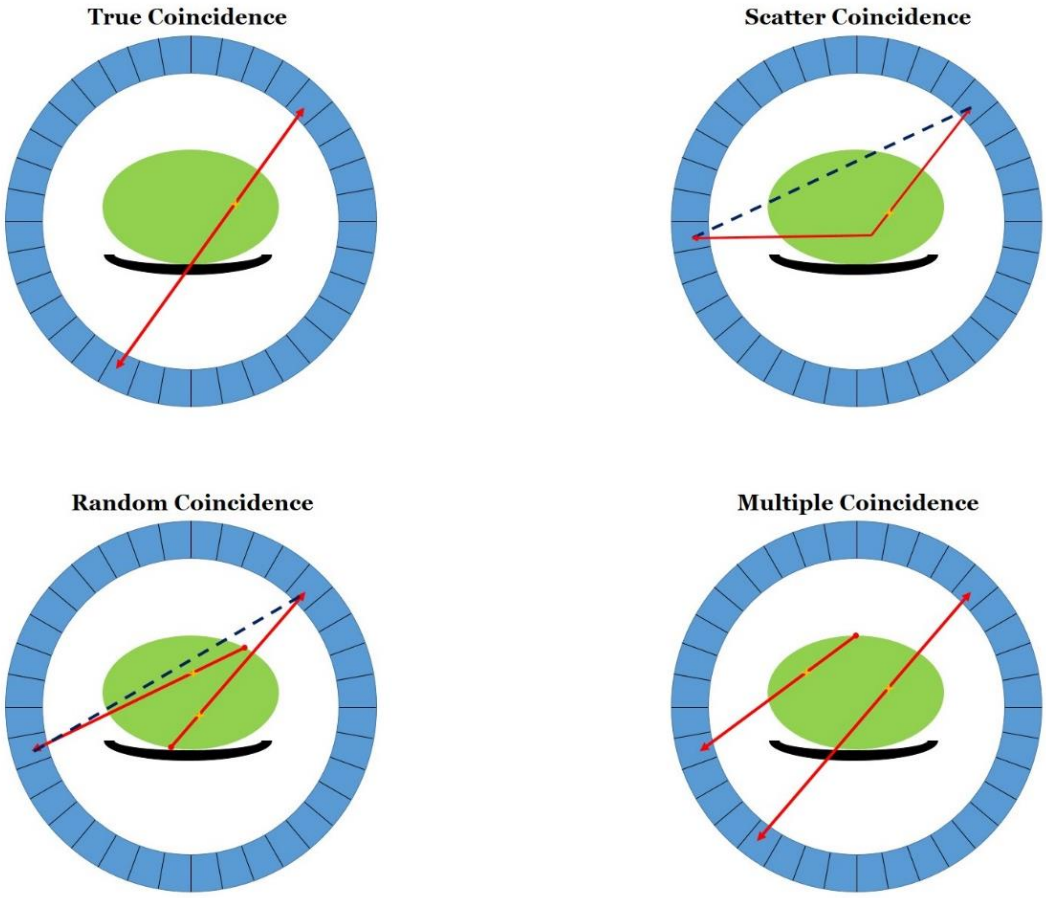

Figure 1-11. Different types of coincidences in PET. The right upper image shows a true coincidence. The left upper image shows a single-scatter coincidence and the incorrect LOR is shown as the blue dashed line. The left lower image shows a random coincidence and the incorrect LOR is shown as the blue dashed line. The right lower image shows multiple coincidences. PET systems usually do not record any events for multiple coincidences.

Random coincidences are particularly problematic in PET since they might arise from annihilations outside the FOV and can contribute up to 50% of the total recorded coincidences (41). Random coincidences are usually distributed uniformly across the FOV and can cause overestimation of activity concentration, if they are not subtracted. The rate of random coincidences can be estimated by measuring the rate of single events detection (detection of single photons) in each detector pair separately, R_1 and R_2, and using the following equation:

$$R_C = 2\tau R_1 R_2 \tag{1.3}$$

Where τ is the coincidence time window and R_c is the random count rate that is to be subtracted from the prompt count rate to obtain the true coincidence count rate. There are also other methods to estimate random coincidences which can be found in the references (42-44).

1.2.5.5 Dead Time

Scintillation detectors have a limit to photon detection rate. The dead time is the time during which the detector cannot detect any new events because it is still dealing with a previous photon detection process. Single events are the largest contributor to the dead time, because the detector block must process each event until the lack of coincidence is verified. It is important to consider that the single-event rate in PET is very high, often 100 times that of the trues rates. Other contributors in dead time are multiple coincidences (see Figure 1-11) and the detector block architecture (41).

In order to compensate for the dead time, most PET scanners use empirical dead time models in which the observed count rate as a function of radioactivity concentration is measured for different object sizes and energy thresholds. The resulting data are then fit to the appropriate dead time models (4).

1.2.5.6 Motion Artifacts

Scan time in PET is longer than that in X-ray-based imaging techniques (such as CT). A regular whole-body FDG PET scan takes 30-60 minutes and motions such as breathing are inevitable. Patient motion can lead to image blurring and underestimation or overestimation of the calculated activity in the organs. Moreover, in multimodality systems such as PET/CT, functional and anatomical images are acquired sequentially (and not simultaneously), and even a small patient motion in between the scans leads to an image misregistration and consequently quantitative errors in reconstructed PET images.

1.2.5.7 Partial Volume Effect (PVE)

The accuracy of PET quantification is limited due to the relatively poor spatial resolution of a PET system. Spatial-resolution-related effects are referred to as partial volume effects (PVEs).

Various partial volume correction techniques have been proposed for NM modalities to improve the resolution of the images. “Image enhancement techniques” perform the resolution recovery directly from the emission data (45), whereas “image-domain correction techniques” use anatom-

ical images (MRI or CT) to improve the resolution (46, 47). "Projection based correction algorithms" use known properties of the image noise distribution (48). Details of the partial volume correction algorithms in PET are beyond the scope of this work. A comprehensive review of different partial volume correction techniques in PET can be found in (49, 50).

1.3 Interactions of Photons with Matter

In order to discuss the details of the proposed scatter reconstruction techniques, the physics of photon attenuation and scattering should be explained first. Five different types of photon interaction with matter will be introduced in this section, however, the emphasis will be on photoelectric and Compton scattering. The kinematics of these two types will be discussed in detail, due to the nature of this work.

1.3.1 Photoelectric Effect

The photoelectric effect is the most important interaction for low energy photons, especially for high atomic number (Z) materials. In a photoelectric interaction, an incident photon hits a tightly bound electron, such as those in the inner shells of an atom, and loses its energy in the coincidence completely. The photoelectric effect for an incident photon (with the energy of $h\nu$) with an electron with binding energy E_b is schematically shown in Figure 1-12.

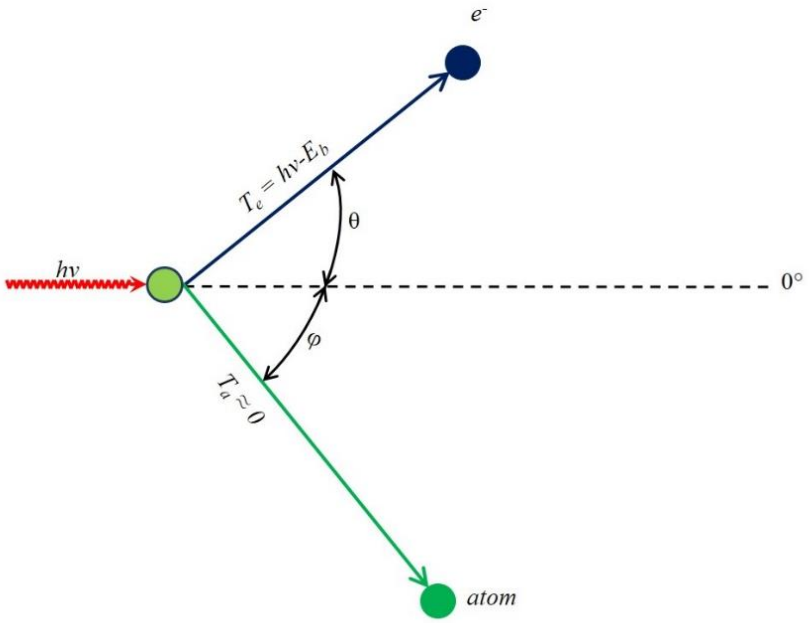

Figure 1-12. Schematic showing the photoelectric effect. An incident photon with initial energy of $h\nu$ (shown in red) strikes an electron with binding energy of E_b (shown in blue) and loses all its energy in this interaction. The electron will then depart at angle θ, relative to the incident photon's direction, with the kinetic energy of $h\nu$-E_b. To preserve momentum conservation, the remainder of the atom departs at an angle φ with practically zero kinetic energy ($T_a \approx 0$).

The smaller $h\nu$ is, the more likely is the occurrence of the photoelectric effect, as long as $h\nu > E_b$. The interaction cross section per atom for photoelectric effect, integrated over all angles of θ (photoelectron emission) is described as

$$\tau_a \cong k\frac{Z^n}{(h\nu)^m} \qquad \left(cm^2 / atom\right) \tag{1.4}$$

where k is a constant, n ≅ 4 at $h\nu$ = 0.1 MeV, gradually increasing to about 4.6 at 3 MeV, and m ≅ 3 at $h\nu$ = 0.1 MeV, gradually decreasing to about 1 at 5 MeV (51).

Attenuation coefficients (μ) are often stated in the form of mass attenuation coefficient (μ/ρ) with the unit of cm^2/g to be independent of density. For instance, photoelectric mass attenuation coefficient (τ/ρ) of 511 keV photons for water is 1.778×10^{-5} cm^2/g, while τ/ρ for photons with the energies of 100 keV and 1 MeV in water is 2.76×10^{-3} cm^2/g and 3.68×10^{-6} cm^2/g, respectively (52).

The photoelectric effect in emission tomography is one of the major sources of attenuation. In NM, this effect is more dominant in SPECT where lower energy photons (often 140 keV photons emitted from ^{99m}Tc) are used and in PET is also considered a noticeable image degrading factor which requires compensation for accurate quantitative PET imaging (see Section 1.2.5.2).

1.3.2 Compton Effect (Incoherent Scattering)

In Compton effect or incoherent scattering, an incident photon strikes an initially stationary un-bounded or free electron. Figure 1-13 shows a schematic illustration of the Compton effect. In a Compton scattering, a photon with the initial energy of $h\nu$ and momentum of $h\nu/c$ collides with an unbounded electron and transfers a part of its energy to the electron. The photon then scatters at angle φ with a new, lower energy, $h\nu'$, and momentum, $h\nu'/c$.

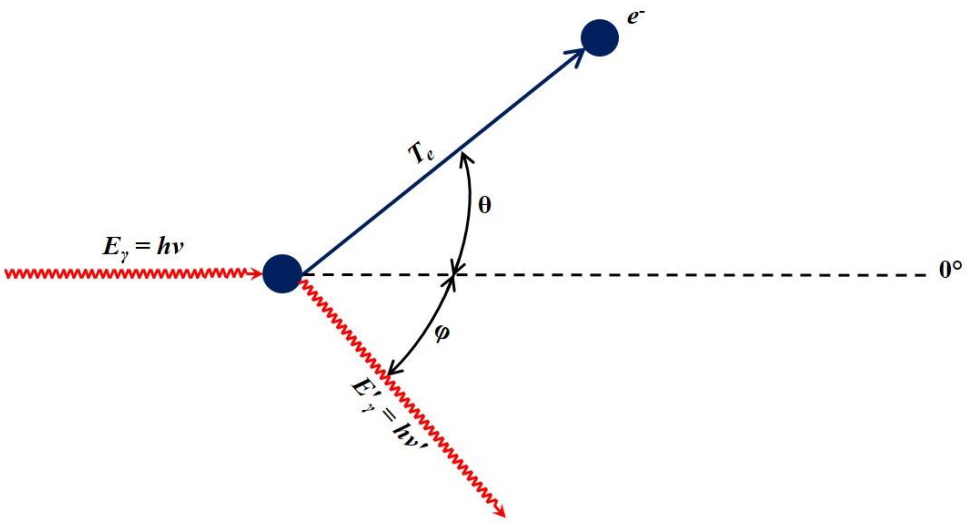

Figure 1-13. Schematic illustration of Compton scattering. A photon, with the initial energy of E_γ, strikes a free stationary electron and scatters at the angle φ with a new lower energy E'_γ. Thus, the energy of E_γ - E'_γ is transferred to the electron and causes the electron to depart at an angle θ.

Therefore the energy of the electron after collision, based on energy conservation would be

$$T_e = h\nu - h\nu' \quad . \tag{1.5}$$

Based on the law of invariance, the relationship between the momentum (p) and energy of the electron (T_e) can be written as

$$pc = \sqrt{T\left(T + 2m_0c^2\right)} \tag{1.6}$$

in which m_0 is the electron's rest mass.

Conservation of momentum along two directions (along the original photon direction at 0° and the perpendicular direction) yields

$$\frac{h\nu}{c} = \frac{h\nu'}{c}\cos\varphi + p.\cos\theta \tag{1.7}$$

$$h\nu'.\sin\varphi = p.c.\sin\theta \ . \tag{1.8}$$

Solving the equations (1.7) and (1.8) for $h\nu$ and $h\nu'$ and using equation (1.6) results in equation (1.9) which defines the relationship between the energy of the incident photon, the scattered photon, and scattering angle (φ).

$$h\nu' = \frac{h\nu}{1+\frac{h\nu}{m_0c^2}\left(1-\cos\varphi\right)} \ . \tag{1.9}$$

Equation (1.9) can also be written in the form of

$$\varphi = \cos^{-1}\left[m_0c^2\left(\frac{2}{h\nu}-\frac{1}{h\nu'}\right)\right] \tag{1.10}$$

which defines the relation between the scattering angle and energy of the incident and scattered photon. Based on this equation, for a given value of $h\nu$, the energy $h\nu'$ and the angle φ of the scattered photon are uniquely correlated to each other and with the assumption that the initial energy of the incident photon is 511 keV the equation (1.10) can be simplified to

$$\varphi = \cos^{-1}\left(2-\frac{m_0c^2}{h\nu'}\right) \ . \tag{1.11}$$

This equation describes the Compton effect in PET imaging, where the initial photons have the energy of 511 keV.

The hypothesis on probability of low energy Compton effect, known as Thomson scattering, was proposed in 1955 (53). This theory stated that the differential cross section per electron for a photon scattered at angle φ per unit solid angle ($\frac{d_e\sigma_0}{d\Omega_\varphi}$), could be expressed as

$$\frac{d_e\sigma_0}{d\Omega_\varphi} = \frac{r_0^2}{2}\left(1+\cos^2\varphi\right) \tag{1.12}$$

in the unit of $cm^2.sr^{-1}$ per electron (*sr* or steradian is the SI unit for solid angle). In this equation, $r_0 = e^2/m_0c^2 = 2.818\times10^{-13}$ *cm*, also known as "classical electron radius." The equation (1.12) is called Thomson scattering cross section equation. The total Thomson scattering cross section per electron, ${}_e\sigma_0$, can be calculated by integrating equation (1.12) over all directions of scattering. With the assumption of cylindrical symmetry, this cross section would be equal to 6.65×10^{-25} $cm^2/electron$. This shows the probability of Thomson scattering for a photon crossing through a 1 cm^2 layer containing one electron. This probability is independent of photon's energy and is known is to be too large for photons with energies higher than 10 keV. The Klein-Nishina equation (equation (1.13)), however, improved and extended the Thomson scattering cross section estimation to higher energy photons by applying Dirac's relativistic theory of the electron to Thomson effect.

$$\frac{d_e\sigma}{d\Omega_\varphi} = \frac{r_0^2}{2}\left(\frac{h\nu'}{h\nu}\right)^2\left(\frac{h\nu}{h\nu'}+\frac{h\nu'}{h\nu}-\sin^2\varphi\right) \tag{1.13}$$

which approaches equation (1.12) for low energies ($h\nu \cong h\nu'$).

The total Klein-Nishina cross section per electron (${}_e\sigma$) is calculated by integrating equation (1.13) over all photon scattering angles, φ, which yields

$$\begin{aligned} {}_e\sigma &= 2\pi\int_{\varphi=0}^{\varphi=\pi}\frac{d_e\sigma}{d\Omega_\varphi}\sin\varphi d\varphi \\ &= 2\pi r_0^2\left\{\frac{1+\alpha}{\alpha^2}\left[\frac{2(1+\alpha)}{1+2\alpha}-\frac{\ln(1+2\alpha)}{\alpha}\right]+\frac{\ln(1+2\alpha)}{2\alpha}-\frac{1+3\alpha}{(1+2\alpha)^2}\right\} \end{aligned} \tag{1.14}$$

in which $\alpha = h\nu \big/ m_0c^2$ (51).

It can be seen that, unlike photoelectric, this cross section is independent of the atomic number (*Z*), therefore

$${}_e\sigma \propto Z^0 \ . \tag{1.15}$$

The Klein-Nishina cross section per atom of any Z and the Klein-Nishina cross section per unit mass or the Compton mass attenuation coefficient can be derived by equations (1.16) and (1.17), respectively.

$$ {}_e\sigma = Z.{}_e\sigma \tag{1.16} $$

$$ \frac{\sigma}{\rho} = \frac{N_A Z}{A}\,{}_e\sigma \qquad \left(cm^2/g\right) \tag{1.17} $$

where $N_A = 6.022\times10^{23}\,\text{mole}^{-1}$ is Avogadro's constant, Z is atomic number, A is mas number, and, therefore, $N_A Z/A$ is the number of electrons per gram of the material.

The Compton mass attenuation coefficient of 511 keV photons in water is 9.575×10^{-2} cm^2/g (52), which is roughly 5000 times greater than the photoelectric mass attenuation coefficient for 511 keV photons in water. In the energy of PET imaging (511 keV), Compton effect is the most probable interaction and thus it is a major problem. Nevertheless, a scattered photon departs with a lower energy and, therefore, with a different cross sections for each type of interaction.

Based on equation (1.11), the energy window of 350 – 650 keV, which is often used in FDG PET studies can detect single-scattered photons with the maximum scattering angle of 57.3° (corresponding to the scattered photons with $h\nu' = 350$ keV).

1.3.3 Other Types of Photon Interactions

Coherent scattering or Rayleigh scattering is a kind of scattering in which the incident photon does not lose its energy at all. This event is considered as an elastic collision of the incident photon with an atom. The atom moves just enough to conserve momentum, and the incident photon is usually redirected through a small angle. As the energy of the incident photon increases, the importance of Rayleigh scattering decreases, partly because the scattering angle is greater in low energies. Coherent scattering mass attenuation coefficient for 511 keV photons in water is 2.151×10^{-4} cm^2/g (52).

Pair production is another type of photon interaction, which is more likely to happen for relatively high energy photons. This interaction has the threshold energy of 1.022 MeV for incident photon and the probability increases as the energy of incident photon increases. In pair production,

the incident photon disappears and gives rise to an electron and a positron. This process takes place in a Coulomb force field and usually near an atomic nucleus. It can also occur in the field of an atomic electron which causes the host electron to acquire significant kinetic energy and therefore the process is called "triplet production" Triplet production has lower probability then pair production and requires the minimum photon energy of 2.044 MeV to preserve conservation of momentum (51).

Photonuclear is also another kind of photon interaction which happens for energetic photons with the energy exceeding a few MeVs. In a photonuclear interaction, the incident photon enters and excites a nucleus, which then emits a proton (γ, p) or neutron (γ, n). This interaction is not of importance in the premise of medical imaging.

Based on various mentioned interactions the total mass attenuation coefficient for photons, μ/ρ (neglecting photonuclear interaction) in units of cm^2/g can be calculated as

$$\frac{\mu}{\rho} = \frac{\tau}{\rho} + \frac{\sigma}{\rho} + \frac{k}{\rho} + \frac{\sigma_R}{\rho} \tag{1.18}$$

in which τ/ρ corresponds to the photoelectric coefficient, σ/ρ to the Compton effect coefficient, k/ρ to the pair production coefficient, and $_R\sigma/\rho$ to the Rayleigh scattering coefficient. The total mass attenuation coefficient for 511 keV photons in water is 9.598×10^{-2} cm^2/g (52).

Mean free path (MFP) is an important quantity that estimates the average path travelled by a photon to do its first intersection and is defined as

$$\lambda = \frac{1}{\mu} \ . \tag{1.19}$$

Assuming the density of 1 g/cm^3 for water, the MFP for 511 keV photons in water is equal to $1/9.598\times10^{-2}$ cm or 10.42 cm.

1.4 Tomographic Image Reconstruction Techniques

Accurate quantitative NM imaging is highly demanded in various clinical and research studies. The prerequisite for accurate quantitative NM imaging is to carefully model and compensate for

the physical image degrading factors occurring during image acquisition. Analytical reconstruction algorithms assume that the data have been pre-corrected (or will be post-corrected) for various effects such as random coincidences, scattered coincidences, and attenuation. Many iterative reconstruction algorithms, however, allow for accurate modeling of these effects as well as noise properties of the image (42). Although many different algorithms for image reconstruction in PET exist, a brief overview of more widely used analytical and iterative image reconstruction techniques are included in this section, and the iterative reconstruction algorithm used in this work will be explained in detail. A more comprehensive review of image reconstruction algorithms in PET can be found in the references (4, 54, 55).

1.4.1 Analytical Image Reconstruction

The image obtained at one angle or view in 3D PET is a "projection" of the 3D distribution onto the 2D detector plane, or in the case of 2D PET, the projection is a 1D signal obtained from one view or angle. The operator that estimates the projection of any arbitrary 3D activity distribution at different angles is called a "projector." In PET, one projection does not contain any information regarding the depth at which annihilation has happened, similar to the situation of finding two values knowing only their sum. Therefore, a large number of views around the object is required to determine relative positions. The idea of image reconstruction in PET is to obtain, as accurately as possible, an image of the radioactivity distribution using projections of this image acquired from several angles.

We define $g(s,\theta)$ as the number of detected LORs that have the distance of s from the isocenter with the slope of the line defined by θ (between 0° and 180°) (see Figure 1-14). This function is the sinogram and as mentioned earlier, it comprises actual recorded projections of the activity distribution, $f(x,y)$, at all views.

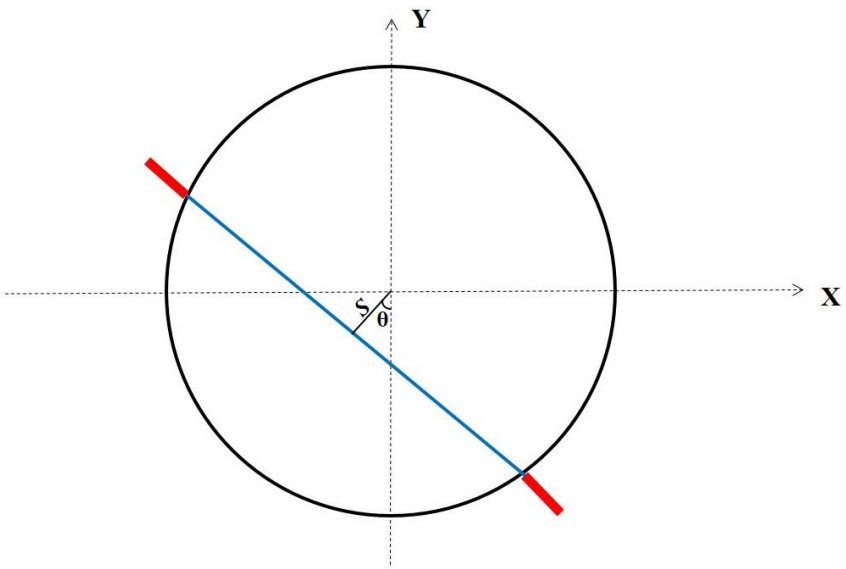

Figure 1-14. Definition of *s* and θ for a sample LOR in PET. The LOR, shown in blue, has the distance *s* from the isocenter with the angle θ.

Mathematically, the projection operator can be defined by the Radon transform (56). The Radon transform $g(s,\theta)$ of a function $f(x,y)$ is the line integral of the values of $f(x,y)$ along the line inclined at angle θ from the X-axis at the distance *s* from the origin and is mathematically given by

$$g(s,\theta) = \int_{-\infty}^{+\infty} f(s.\cos\theta - u.\sin\theta, s.\sin\theta + \mathrm{u}.\cos\theta)\,\mathrm{du}\,. \tag{1.20}$$

Associated with the projection operator, the backprojection operator can be defined as

$$b(x,y) = \int_{0}^{\pi} g(s,\theta)d\theta\ . \tag{1.21}$$

Backprojection represents the accumulation of the ray-sums (equal to projection) of all the rays that pass through any point $M(x,y)$, where *M* denotes an approximation to the true distribution, *f(x,y)*. The most basic analytical approach for reconstructing an image from the profiles is by simple backprojection (BP), in which the projections shown in the sinogram are backprojected to form an image. This technique does not apply any filters and leads to blurring in the reconstructed image. The most common analytical technique involves filtering the projections in the frequency domain and then applying backprojection, which is known as filtered backprojection

(FBP). A sample 2D reconstruction done with simple BP and FBP algorithm is shown in Figure 1-15.

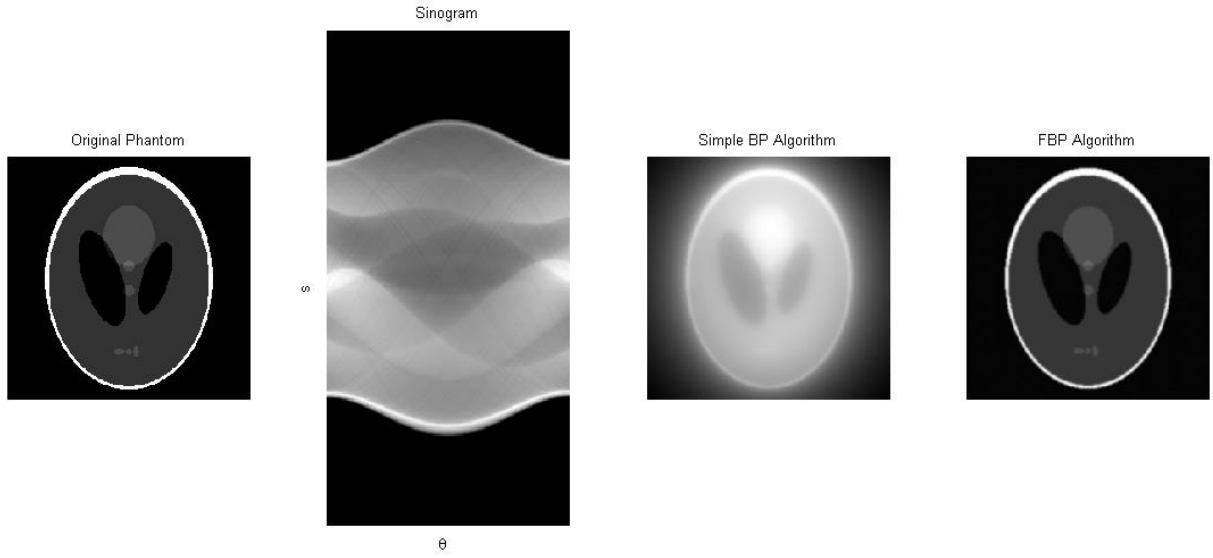

Figure 1-15. Example reconstructed images by backprojection and filtered backprojection techniques. From the left side, the first image is the original image of the Shepp-Logan phantom, the second image is the sinogram generated within the angular range of 0°-180° with increments of 1°, the third image is the reconstructed image using simple backprojection algorithm, and the last image is the reconstructed image by filtered backprojection algorithm using the Hamming filter.

As shown in Figure 1-15, simple backprojection leads to a blurring. FBP, on the other hand, reduces the blurring and had been the main reconstruction technique for many years in clinical tomographic systems, because of its relatively low computational load, in comparison with iterative reconstruction algorithms.

In 3D PET, sensitivity of photon detection increases significantly, due to the detection of out-of-plane LORs. Indeed, out-of-plane LORs have the greatest contribution to all recorded events. These LORs and their corresponding sinograms are known as oblique LORs and oblique sinograms, respectively. Some oblique sinograms beyond a certain azimuthal angle will not be entirely filled in due to the limited axial size of FOV. In other words, truncating the FOV along the axial direction results in part of data required to complete some oblique sinograms being missed. The reason for incomplete sinograms beyond a certain angle is that for some oblique LORs only one of the annihilation photos has the chance of reaching PET detectors, while the other photon escapes from the FOV. The error associated with the incomplete sinogram in 3D PET is known as “truncation error.” One way to overcome truncated data is to estimate an initial image from

present sinograms and then calculate missed projections by forward projecting the image onto the missing LOR coordinates (42). Due to the large computational load in 3D PET, it is preferred to reduce the 3D data set into a 2D data set and then reconstruct the image based on a 2D reconstruction algorithm. Data reduction techniques in 3D PET includes transition techniques for oblique 3D sinograms to 2D data sets, known as "rebinning algorithms." Rebinning algorithms are usually associated with some approximation and undergo a trade-off between the speed and accuracy. Although exact rebinning methods have also been proposed (57), most common rebinning algorithms in practice are those in which approximations are used. The single-slice rebinning algorithm (SSRB) (58) and Fourier rebinning algorithm (FORE) (59) are the most widely used rebinning algorithms in clinical 3D PET systems.

Since in this work a fully 3D iterative reconstruction algorithm was employed, details of the rebinning algorithms will not be discussed, however, a comprehensive review of these algorithms can be found in (42, 55).

1.4.2 Iterative Image Reconstruction

The basic principle of iterative methods is in finding a vector f that is a solution of $g = Af$, where g is the stack of acquired projections (sinogram), and A is a matrix that represents the imaging system, known as "system matrix." This equation is an ill-posed inverse problem that is not easy to solve. Therefore, numerical iterative solutions are employed to find f by successive estimates. Each iteration of the algorithm is divided into two steps: in the expectation step (E step), the formula expressing the likelihood of any reconstructed image given the measured data is formed, and in the maximization step (M step), that image that has the greatest likelihood to give the measured data is found (60). This led to the ML-EM algorithm (61), defines as follow

$$\bar{f}_j^{(k+1)} = \frac{\bar{f}_j^{(k)}}{\sum_{i=1}^{n} a_{ij}} \sum_{i=1}^{n} \frac{g_i}{\sum_{j'=1}^{m} a_{ij} \bar{f}_{j'}^{(k)}} a_{ij} \tag{1.22}$$

in which $\bar{f}_j^{(k)}$ denotes pixel number j of the image $(\bar{f})$ at k^{th} iteration, m is the total number of pixels in the image, n is the total number of projections in the sinogram (bins), g_i is the i^{th} vector taken from the sinogram (i^{th} projection), and a_{ij} is the array at i^{th} row and j^{th} column of the

system matrix *A* so that the equation $g=Af$ is satisfied. Physical effects such as attenuation, scatter modeling, and blurring could be included in *A*, the system matrix.

The EM algorithm can be seen as a set of successive projections/backprojections (62) so that EM algorithms can be written, conceptually, as

$$\text{Image}^{(k+1)} = \text{Image}^{(k)} \times \text{Normalized Backprojection of} \left(\frac{\text{Measured projections}}{\text{Projections of image}^{(k)}} \right) . \quad (1.23)$$

The ML-EM algorithm is computationally heavy and converges slowly and may require 50-200 iterations to converge. The ordered-subset expectation maximization (OS-EM) has been proposed (63) to accelerate the process. In the OS-EM, the set of projections is divided into subsets, and the ML-EM algorithm is then applied to each subset to help achieve convergence faster.

The reconstructed images obtained using the ML-EM algorithm tend to become noisy as the number of iteration increases, because the noisy reconstructed images may yield projections that are very close to the measured noisy projections (64). Maximum a posteriori (MAP) algorithms were introduced to reconstruct an image that is as close as possible to the measured projections and also is not too noisy. The introduction of prior knowledge as a constraint that may favor convergence of the EM process is called regularization (62).

In order to prepare the recorded coincidences for being used in the ML-EM algorithm, they need to be saved in a set of sinograms. This way of recording coincidences is termed "histogram-mode." Another mode for recording coincidences in PET is "list-mode", in which recorded coincidences are saved in a time list of coincidences, unlike the histogram mode that counts the number of similar LORs in each possible bin to form a sinogram. List-mode reconstruction techniques have some advantages over projection-based algorithms (algorithms that use histogram-mode data), such as avoiding data loss which occurs frequently as a result of the approximations used in sinogram generation. An EM technique for reconstruction based on the list-mode data was first proposed by (65) and developed for 2D and 3D PET by (66) and (67), respectively.

Using the same notation as in equation (1.22), list-mode ML-EM can be shown as

$$\overline{f}_j^{(k+1)} = \frac{\overline{f}_j^{(k)}}{\sum_{i=1}^{n} a_{ij}} \sum_{i=1}^{M} \frac{1}{\sum_{j=1}^{m} a_{ij} \overline{f}_j^{(k)}} a_{ij} \quad (1.24)$$

in which M is the total number of recorded LORs.

Depending on the number of events, iterative reconstruction directly from list-mode data can be computationally expensive. Therefore, a new LM reconstruction based on a single pass through the data is presented by (68). In this paper, analytical reconstruction, conventional ML-EM, and the new list-mode method were compared, and acceptable results for the new method were reported. This algorithm is known as one-pass list-mode expectation-maximization (OPL-EM) and is mathematically given by

$$\bar{f}_j^{(k+1)} = \frac{\bar{f}_j^{(k)}}{\sum_{i=1}^{n} a_{ij}} \sum_{i \in T^k} \frac{1}{\sum_{j=1}^{m} a_{ij} \bar{f}_j^{(k)}} a_{ij}, \quad \text{for } k = 1, ..., K \ . \tag{1.25}$$

In comparison with conventional list-mode ML-EM, given by equation (1.24), the only difference here is that the summation is now only over those list-mode events, i, which are present in the k^{th} subset, T^k, which is a time subset of the list-mode data. As in any other EM algorithms, the system matrix A may include exact modeling of physical effects such as blurring, scatter, and attenuation.

1.5 Previous Work on Scatter Reconstruction in PET

The idea of using scattered coincidences in image reconstruction in PET was first proposed by (1) and (2) almost concurrently. In (1), a new projection/backprojection technique was proposed and implemented in list-mode EM reconstruction algorithm for scattered events in 2D non-TOF PET. In the proposed method, all possible pixels for each single-scatter event are detected and backprojection over the pixels is done assuming that the detected pixels have the same annihilation probability. The authors developed the proposed algorithm by introducing a new scatter-reconstruction-dedicated attenuation correction algorithm in (69) and implementing patient outline to their suggested image reconstruction algorithm in (70). Technical aspects of this algorithm will be explained in Section 2.2 in detail. Moreover, a part of the results reported in the mentioned papers will be discussed in Chapter 4 to compare with the results of this work.

In another work, a different algorithm was proposed in which the temporal and spatial information, as well as deposited energies of the annihilation photons were used to reconstruct the image based on scattered coincidences in a 3D TOF PET system (2). Also, the effects of energy

and timing resolution of PET detectors were presented in this work. Unlike the non-TOF scatter reconstruction technique shown in (1), the scatter reconstruction technique in (2) is based on splitting each scattered event into several possible trajectories and dealing with each trajectory independent of the others. The hurdle in this work is to find the possible trajectories, and once the trajectories are found, they will be treated as in regular list-mode EM reconstruction technique. A detailed review of the physics and technical aspects of this method will also be discussed in Chapter 2.

1.6 Objectives of the Study

The work presented in this thesis is extension of two previously developed scatter reconstruction techniques in 2D non-TOF PET (1) and 3D TOF PET (2) to 3D non-TOF PET. The ultimate goal of the research is to develop a fully 3D iterative reconstruction technique for non-TOF PET, which unlike many conventional scatter correction techniques, takes advantages of scattered events as well as true (unscattered) events. The study does not use TOF information of the recorded events, which differs from previous work (2) and represents the possibility of 3D scatter reconstruction without using TOF information.

Although many other effects, such as random coincidences and sensitivity correction along FOV, are not considered in this work, attenuation correction for true events is implemented in the proposed reconstruction technique. Two different methods of attenuation correction for scatter coincidences are explained and compared. To avoid geometry-dependent-artifacts, ideal PET systems are simulated and used in this research (discussed in Section 2.3.1).

Moreover, a novel mathematical method for fast ray-tracing of curved lines and surfaces is introduced which has the potential of speeding up this type of algorithm.

2 Chapter Two: Methodology

The most important part of this work is the new projector/backprojector algorithms that have been implemented into the one-pass list-mode expectation-maximization (OPL-EM) reconstruction method in order to perform the scatter reconstruction. Details of the reconstruction techniques (including new projector/backprojector operators), Monte Carlo (MC) simulations, and assessment of the proposed techniques are discussed in this chapter.

2.1 Reconstruction Technique

All required data for image reconstruction in this work were saved in list-mode format. One-pass list-mode expectation-maximization, given by equation (1.25), was the reconstruction technique in this work and all images were reconstructed using this technique to minimize the reconstruction time by processing each coincidence once only. No rebinning (data reduction) was used for either true or scatter coincidences, and a fully 3D reconstruction method was employed. The number of subsets in OPL-EM was chosen empirically for each image reconstruction and only the reconstructed images with the same level of convergence were quantitatively compared to each other. Since the time required for reconstruction is highly dependent on the matrix size of the reconstructed images, reconstructions that did not require quantitative analysis were done in a relatively low resolution matrix size.

Siddon's ray tracing algorithm (71) was used to calculate the system matrix, A, for true coincidences on-the-fly, as explained in (68, 72). Although pre-calculation of the system matrix speeds up the reconstruction, it was not feasible to do this for scatter coincidences, due to the variation in scattering angles and detection positions.

The data in this study were obtained from MC simulations and, therefore, the complete history of each coincidence before detection was known. Using this information, random and multiply-scattered coincidences were subtracted from the list of events, prior to starting the reconstruction algorithm. Ideal PET systems were simulated to cover the whole object in the axial direction to reduce the problems of data truncation and activity outside the field of view (FOV) (73). The specifications of the simulated PET systems will be further discussed in Section 2.3.1. The system matrix used in the reconstruction step does not contain information regarding sensitivity var-

iations across the FOV and does not model blurring. No regularization was applied in the reconstruction technique.

Computed tomography images for defining the patient outline and attenuation correction were defined in MATLAB. In order to perform image registration, CT images were downsized to the matrix size of PET images and a blurring process was applied to downscale the resolution of CT images. Blurring of CT images was done with cubic interpolation method for each 2D CT slice, using a 4×4 averaging kernel.

CT images were then segmented based on various materials (i.e. air, plastic, and water) and proper attenuation coefficient for each material for required energy were extracted from (52). As explained in the next section (Section 2.2), some types of suggested projection algorithms require exact attenuation coefficients for energies other than 511 keV. In this case, a 4D attenuation map, where 4^{th} dimension is energy, was defined for each reconstruction. A total of 17 attenuation maps for energies between 350 – 511 keV was generated (with 10 keV incrementing) to be used in the attenuation correction algorithm.

The information regarding patient/phantom outline was also obtained from CT images and used in reconstructions as explained later. No post-filtering was applied on reconstructed images.

2.2 Projection/Backprojection Techniques

Two different types of projector/backprojector were used in this work. The ideas of both techniques were previously developed and reported in (1) and (2). In this section, first the underlying physics of both techniques will be discussed in detail, and then extension of each technique to 3D non-time-of-flight (non-TOF) PET will be explained.

2.2.1 Physics of Single-Scatter Reconstruction

A schematic of a single-scatter coincidence is shown in Figure 2-1. Assuming that photon annihilation happens at the point *O*, an unscattered photon is detected at *A* and the other annihilation photon undergoes Compton scattering with the scattering angle of θ in *S* and is detected at *B*. For simplicity this figure shows a single-scatter event in 2D.

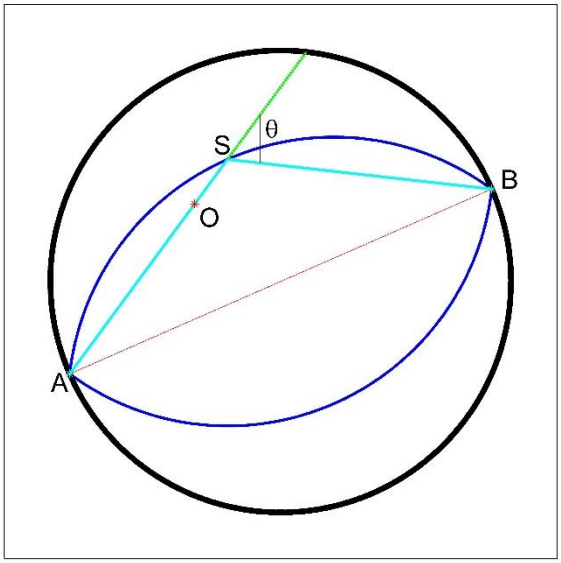

Figure 2-1. Schematic illustration of a single-scatter coincidence in PET. The PET ring is shown as a black circle. One of the annihilation photons is detected at *A* the other one is detected at *B* following a Compton scattering at *S*.

In a PET machine, information regarding the position of detected photons (*A* and *B*) and their associated energies (E_A and E_B) are recorded. Assuming that the deposited energy of both photons in *A* and *B* are known exactly, one can determine the scattering angle (θ), using equation (1.11). In 2D PET, for any single-scatter event with fixed detection points, *A* and *B*, and known scattering angle, θ, the locus of possible scattering points is restricted to two circular arcs (TCA). For scattering events occurring on the TCA, annihilation must have occurred in the region bounded by the TCA. For instance, in Figure 2-1, the TCA (shown in blue), represent all possible positions that for any arbitrary annihilation in between them, a scattered event with scattering angle θ might have happened on these arcs and photons will be detected at *A* and *B*. The concept of TCA was first proposed in (1) for 2D PET. For each single-scatter coincidence in PET, we are able to determine its corresponding TCA and, therefore, the possible area that covers the annihilation position associated with that event. In this thesis positions on the TCA are referred to as "scattering centers", since the scattering event has happened somewhere on these lines. In 3D PET, however, scattering centers are defined as a surface (rather than two arcs). This surface is analogous to TCA in 2D PET in terms of properties and can be obtained by rotating one of the circular arcs around a line connecting two detection points (the red line in Figure 2-1). Figure 2-2 shows sample scattering centers for a single-scatter event in a 3D PET system.

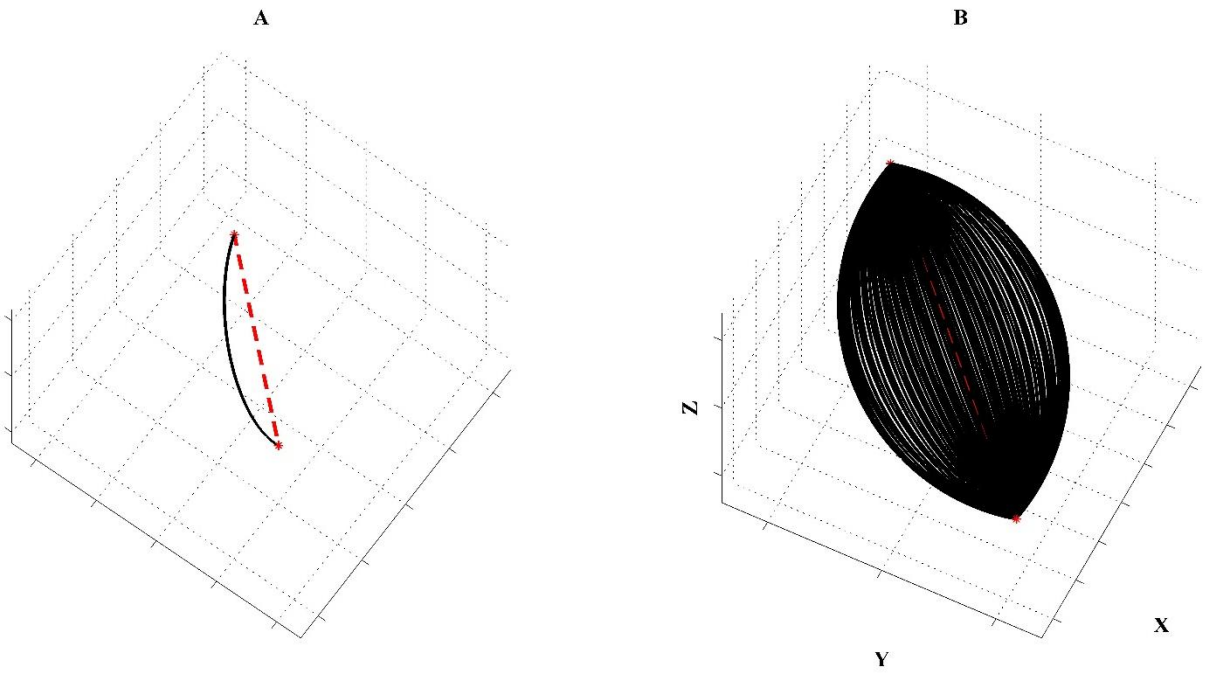

Figure 2-2. Sample scattering centers for a single-scatter event in 3D PET. Note that neither PET system, nor the scattered event is shown here. Red dashed line connects two detection points. (A) shows one single arc of the scattering surface, and (B) illustrates the complete scattering surface covering all possible scattering centers for this particular single-scatter event. This surface is obtained by rotating the arc in (A) around the dashed red line.

This surface can be mathematically defined as

$$\vec{S}(\varphi,\vec{\mathrm{q}}) = \vec{O} + R.\cos\varphi.\vec{p} + R.\sin\varphi.\vec{q} \tag{2.1}$$

where $\vec{S}$ is a vector containing the coordinates of the scattering surface, $\vec{p}$ is the unit vector along the vector connecting two detection points, *A* and *B*, $\vec{q}$ is a set of unit vectors that are perpendicular to $\vec{p}$, $\vec{O}$ is the coordinate of the circle for each arc, *R* is the radius of the circles (same for all circles), and φ is a range of angles that truncates the whole circle to an arc. Appendix A contains more details on these concepts and the mathematical derivation of equation (2.1).

Based on the inherent properties of the defined scattering surface, for each point on the scattering surface, S_i, a broken line (two-piece line with angle 180-θ in between them) $A - S_i - B$ can be defined, such that this broken line defines a possible trajectory for the recorded event. It is important to note that for each point on the scattering surface, only one possible trajectory for the

scattering event can be defined. Each $A - S_i - B$ broken line is called a broken line-of-response or b-LOR (notation taken from (2)).

Finding voxels inside and on the scattering surface could be very time consuming, since for each single-scatter event all voxels should be evaluated. This could increase the computational load in 3D PET considerably. For instance, in 3D scatter reconstruction with the matrix size of $N \times N \times N$, N^3 individual calculations need to be done for each single-scatter coincidence to find all voxels on the scattering surface which could be very time-consuming and inefficient. A new mathematical ray-tracing approach is proposed in this work that reduces the number of calculations to $3 \times M \times N$ (instead of N^3) for each single-scatter coincidence, where M is the number of rotations required for each 1D line on the scattering surface to imitate the geometry of a 3D scattering surface. The rationale behind this technique is similar to the well-known Siddon's ray tracing technique (71) and is explained in detail in Appendix B.

As mentioned before, the reconstruction technique in this work is OPL-EM. One challenge to incorporate scatter reconstruction in list-mode reconstruction is computational inefficiency, meaning that for large scatter angle events, since the area between the scattering centers may occupy a considerable fraction of the whole reconstruction volume, which means that the scattered event practically does not provide much beneficial information. The patient outline could be used to further confine the number of voxels in which annihilation might have happened. In clinical trials, patient outline can be defined based on available anatomical images (in hybrid imaging modalities such as PET/CT) or by estimation of the patient outline based on an initial reconstructed image obtained purely by PET. The idea of using patient outline to further confine the reconstruction technique was first developed by (2, 70).

Figure 2-3 shows how defining patient outline further confines the reconstruction algorithm. Note that this figure shows only one sample 2D situation of the overlap between patient outline and scattering surface to clarify how patient outline information might be useful in reconstruction.

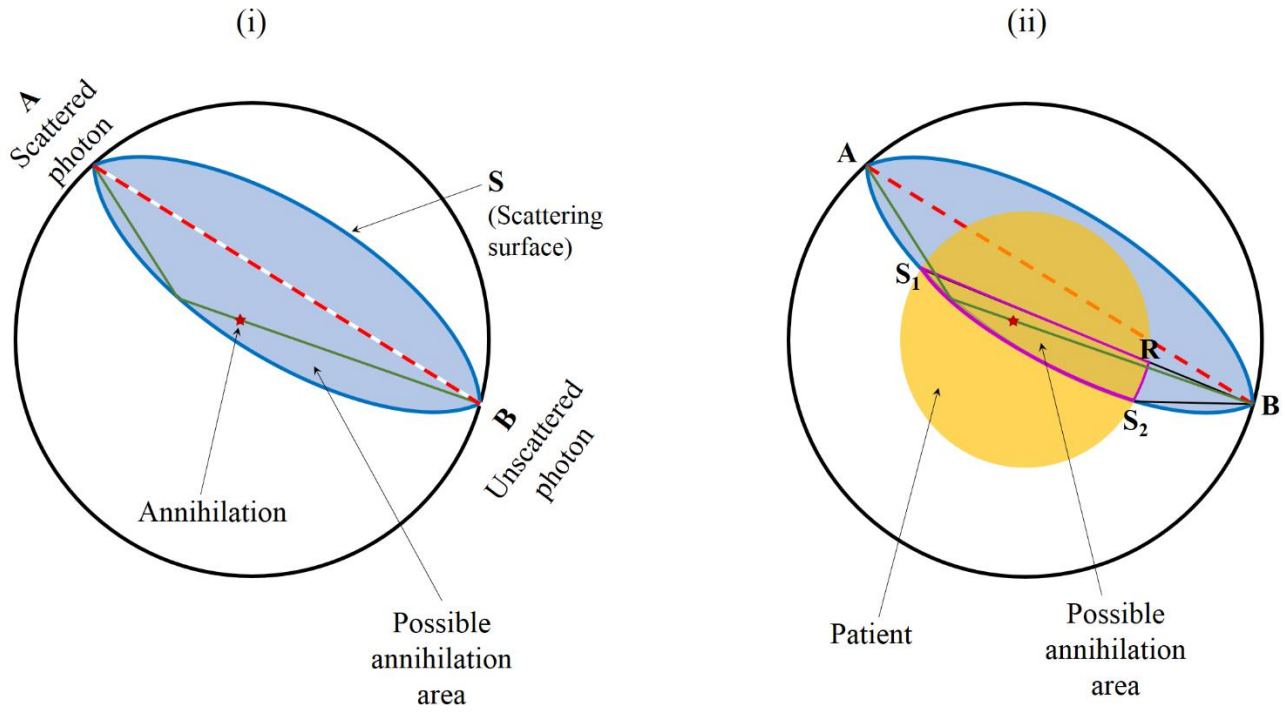

Figure 2-3. Drawing shows how patient outline constrains the possible annihilation area. Without patient outline information, as shown in (i), all of the area enclosed within the scattering surface, except the red dashed line, has the same probability for annihilation to happen (shown in light blue), whereas with the knowledge of patient outline, the possible area for the annihilation is constrained to the area confined by $S_1S_2 - S_2R - S_1R$. The boundaries of this area are shown in pink.

Conceptually, introducing a patient outline limits the scattering centers to only that part of the scattering surface that overlaps with patient. Annihilation must have happened somewhere inside scattering surface but within the patient boundary. Therefore, annihilation might have happened in any location that a b-LOR $A - S_i - B$ can be defined, such that S_i is a point inside the patient boundary. In this work, the effect of activity outside the FOV and scattering in other available physical objects (patient couch, crystal, etc.) was ignored. Also, the patient outline was incorporated in all reconstructions in this work.

2.2.2 Uniform Projection/Backprojection

In uniform projection/backprojection technique, an important assumption is that the probability that annihilation occurred in a given voxel is the same for all voxels enclosed within the scattering surface. This assumption is based on the fact that, for a uniform activity distribution in a uniform medium (same electron density), all points within the scattering surface have the same an-

nihilation probability, except points on the *A*-*B* line. The assumption is valid due to the isotropic nature of photon annihilation. In other word, for each single-scatter event, all points within the scattering surface have the same probability to generate a b-LOR associated with that scattering surface. With activity distribution of $f(x)$ over the object, the probability of single-scatter event detection with a scattering angle of θ, at points *A* and *B*, where an unscattered photon is detected in *A* and scattered photon in *B*, with a non-uniform object with electron density ρ_e is proportional to (1)

$$P_{ab}(\theta) \propto \oint_{AB} \int_{A}^{S} f(x)dx.\rho_e(S).\frac{d\sigma}{d\theta}.e^{-\left(\int_{A}^{S}\mu dl+\int_{S}^{B}\mu dl\right)}ds \tag{2.2}$$

where *S* represents points on the scattering surface, $d\sigma/d\theta$ is the Compton cross section for 511 keV photons at point *S*, and the exponential terms takes the attenuation for both photons into account. In this approach, the backprojector operator simplifies the reconstruction by assuming a uniform electron density distribution all over the body and zero electron density outside the body.

The uniform projector calculates the summation of voxel intensity in voxels confined by both the patient outline and the scattering surface for each single-scatter event (equivalent to the area confined by $S_1S_2 - S_1R - S_1R$ in Figure 2-3). The probability of annihilation in each voxel, with the assumption of identical probability for all voxels, is then calculated and the uniform backprojector operator backprojects (assigns) this probability to the corresponding voxels. Implementation of the uniform projector/backprojector in OPL-EM does not change the reconstruction algorithm mathematically and equation (1.25) is still valid for scatter projection/backprojection. However, the system matrix for each single-scatter coincidence needs to be modified accordingly.

The following graphical example clarifies this issue. Figure 2-4 illustrates a sample single-scatter coincidence in 2D with the scattering angle of 55° and Figure 2-5 compares a row of the system matrix (shown as 2D probability image) for this event to further explain the details of uniform projector/backprojector operators. Images shown in Figure 2-5 are reconstructed within the reconstruction zone shown as a brown square in Figure 2-4. The imaging object is assumed to be a

uniform cylindrical water phantom with the diameter of 3.5 cm. The CT image of this object is also shown in Figure 2-5-B.

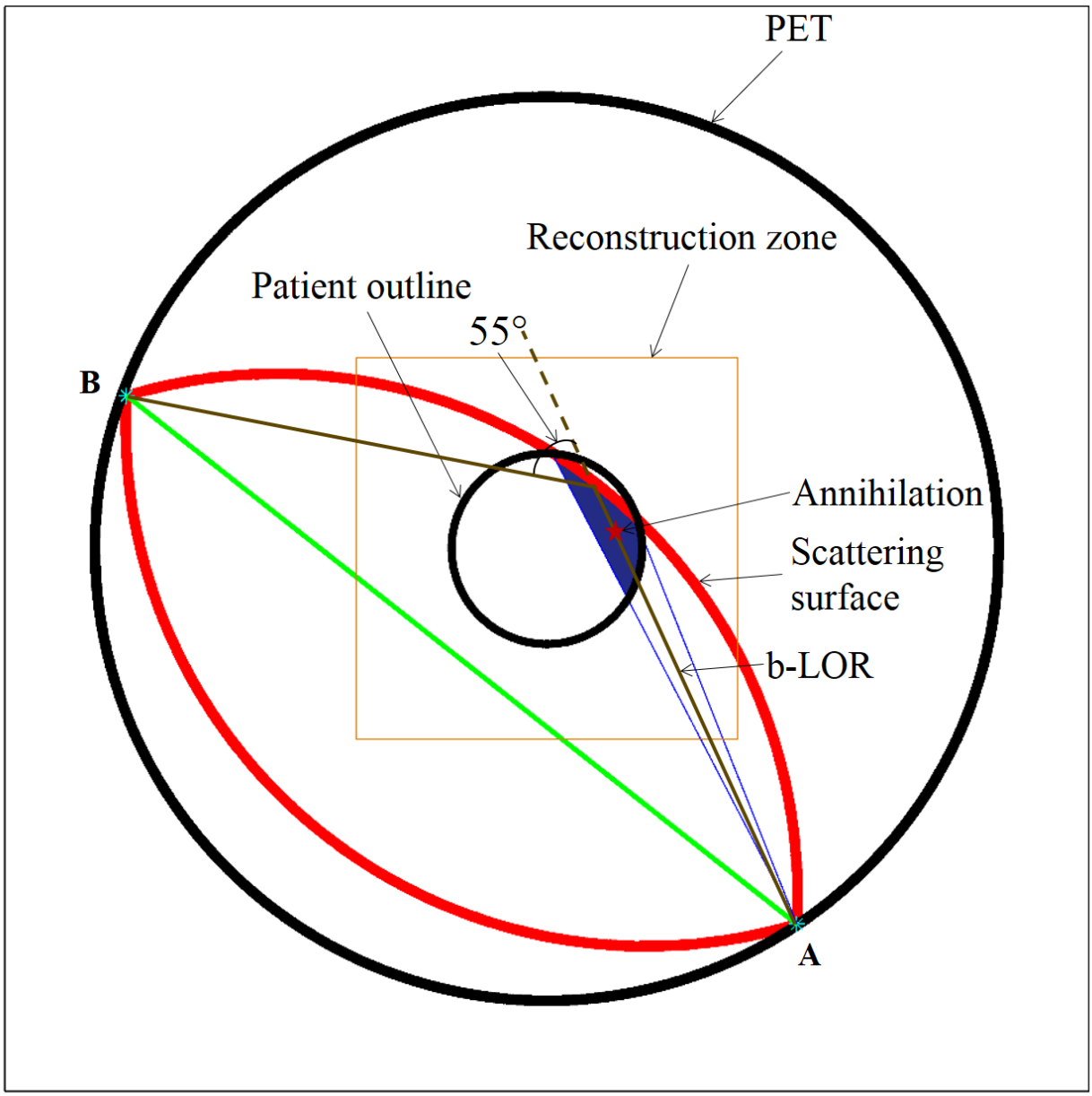

Figure 2-4. Schematic of how uniform projector/backprojector deals with single-scatter coincidences. A sample single-scatter event with the scattering angle of 55° is shown. The scattered photon is detected at B and the unscattered photon is detected at A. The external and inner black circles represent the PET system and patient outline, respectively. The area within the scattering surface almost covers the whole patient boundary, however, using patient outline information projection/backprojection area can be constrained to only the area shown in blue (covering annihilation).

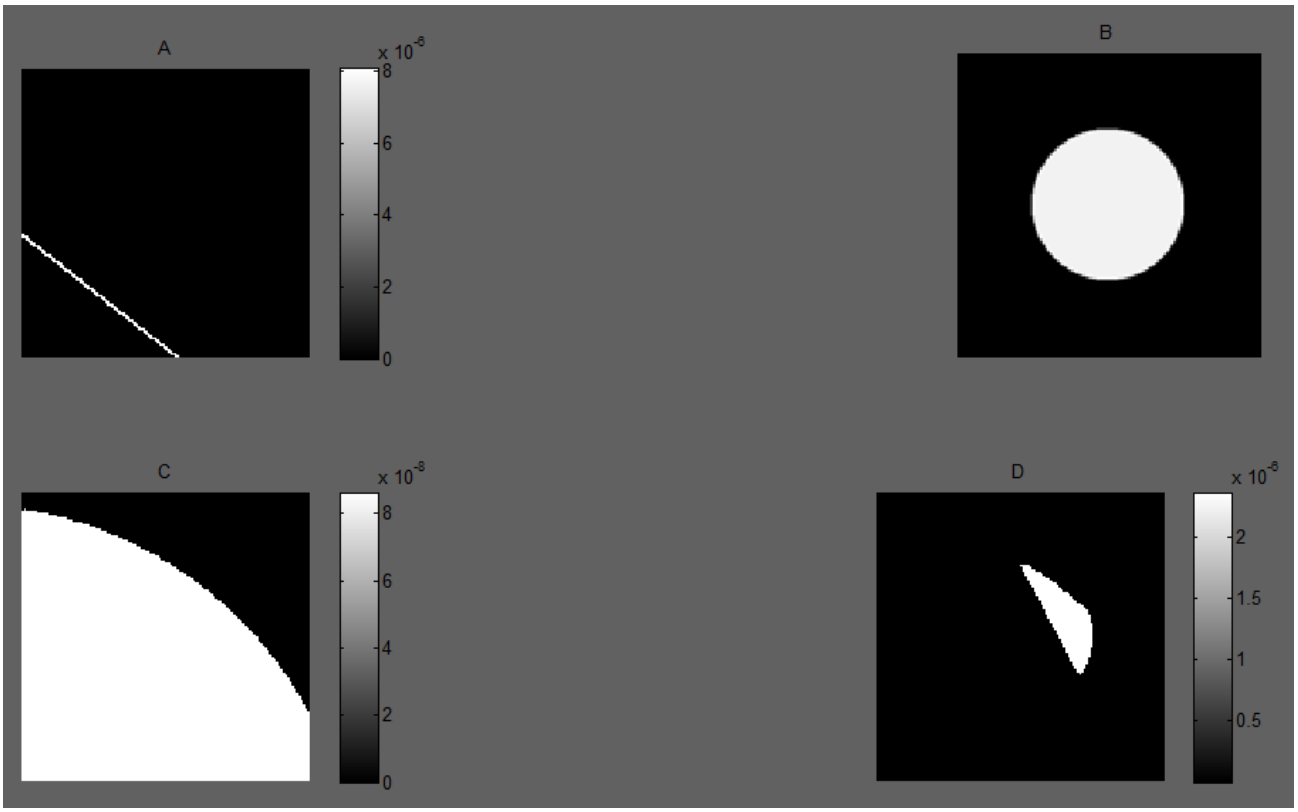

Figure 2-5. Example of probability images in different reconstruction techniques. (A) is a sample probability image (one row of the system matrix) for a scattered event when conventional list-mode method for system matrix generation was used, (B) shows the CT image of the cylindrical phantom, (C) shows the probability image when uniform projector/backprojector is applied but information regarding patient outline is not used, and (D) shows the same probability image as in (C), however, this time patient outline information is used.

Probability for each coincidence is backprojected in a way that the total probability for each coincidence should be equal to one. As it can be seen in Figure 2-5, the uniform backprojector operator assigns the calculated probability only to the section corresponding to the blue area shown in Figure 2-4. A coregistered image of the CT and probability images is shown in Figure 2-6.

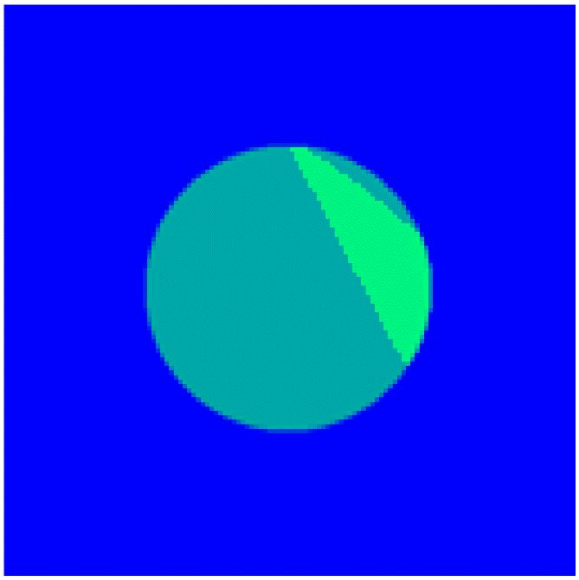

Figure 2-6. Coregistered CT and probability image. CT image is shown in the background, and the back-projected area is shown in green over the CT image.

2.2.3 B-LOR Projector/Backprojector

In (2), reconstruction of scatter coincidences was done based on the assumption that for each voxel intersecting with scattering surface only one b-LOR can be defined. Under this assumption, *N* b-LORs are defined for each scatter coincidence, where *N* is the number of voxels that intersect with the scattering surface and the patient's body. Figure 2-7-(i) shows all possible b-LORs for a sample single-scatter event in 2D PET to clarify the concept of b-LOR (matrix size 64×64). Note that an annihilation event must have occurred somewhere on the segment of the b-LOR between the scattering point and the detection point of the unscattered photon. For instance, if an unscattered photon is detected at *B*, only a part of B-S_i lines that are within patient boundary represents the possible annihilation locus. Image (ii) in Figure 2-7 illustrates these lines for the single-scatter event shown in Figure 2-7-(i).

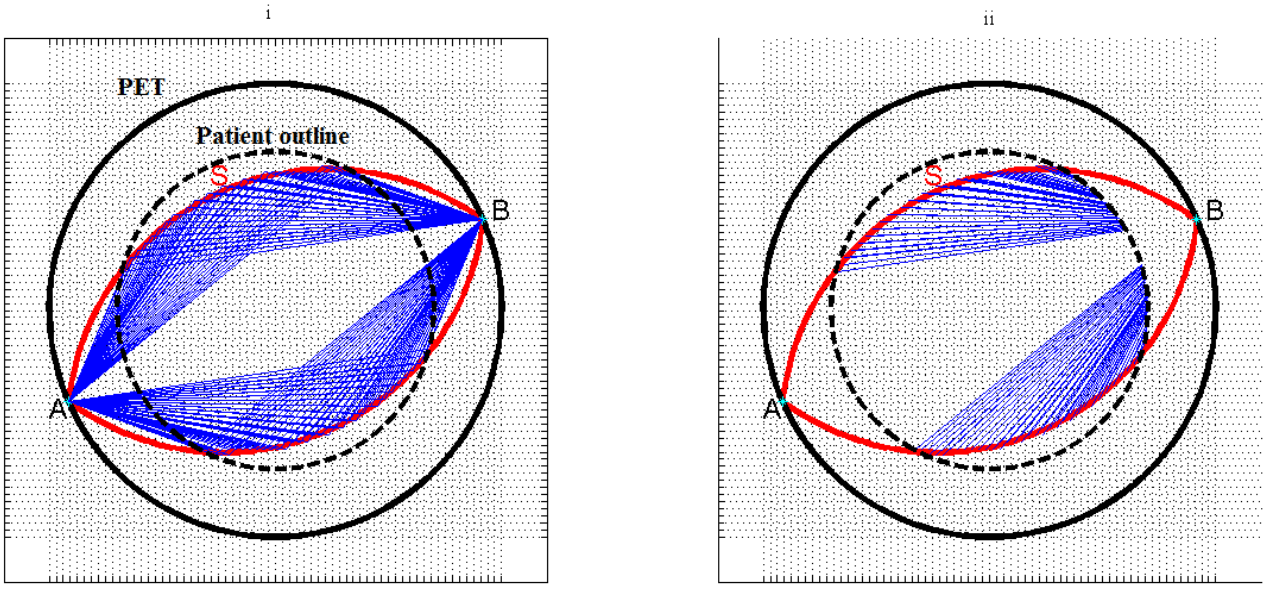

Figure 2-7. All possible b-LORs for a sample single-scatter event with assumption of one b-LOR per scattering center's voxel. The two red arcs represent the scattering surface and b-LORs are shown in blue lines. (i) shows all possible b-LORs in their complete form and (ii) shows only the part of b-LORs that covers the annihilation area.

In this manner, for each single-scatter event, the number of b-LORs that are going to be considered in image reconstruction is a function of the reconstruction matrix size. This is because changing matrix size varies the number of scattering centers and hence creates a different number of b-LORs.

Assuming that the unscattered photon is detected at *B*, the projector operator in b-LOR scatter reconstruction technique is the summation over the part of each $S_i - B$ line that is contained within the patient boundary. The backprojector operator also backprojects calculated values over the same region for each line. It is important to note that in the b-LOR technique the $A - S_i$ segment of broken lines is not included in either the projection or backprojection step. The $A - S_i$ lines only play a role in the attenuation correction step which is explained in Section 2.2.4. Therefore, in the b-LOR projection/backprojection technique each single-scatter coincidence is essentially divided into several b-LORs and the OPL-EM algorithm needs to be run over each b-LOR separately. However, b-LORs do not have the same probability. Considering the fact that the annihilation has occurred on one of the possible $S_i - B$ lines and all points on different $S_i - B$ lines have the same annihilation probability (as explained before), the probability of each

line is proportional to the length of the line. Thus, the longer $S_i - B$ is, the more annihilation probability should be considered. The summation of probabilities of all b-LORs should be equal to one for each single-scatter coincidence as the normalization of the probability. We can write these two conditions as

$$\begin{aligned} w_p &\propto L_{S_p - B} \\ \sum_{p=1}^{P} w_p &= 1 \end{aligned} \tag{2.3}$$

where w_p represents the probability for the p^{th} b-LOR, $L_{S_p - B}$ is the length of $S_p - B$ line inside the patient (and not the total length), and P is the total number of scattering centers inside the patient. These two equations can be re-written as

$$w_i = \frac{L_{S_i - B}}{\sum_{p=1}^{P} L_{S_p - B}} \quad . \tag{2.4}$$

Therefore, with the same notation as above and in equation (1.25), modified OPL-EM equation for b-LOR scatter reconstruction can mathematically be written as

$$\overline{f}_j^{(k+1)} = \frac{\overline{f}_j^{(k)}}{\sum_{i=1}^{n} a_{ij}} \sum_{i \in T^k} \sum_{p=1}^{P} \frac{w_p}{\sum_{j=1}^{m} a_{pj} \overline{f}_j^{(k)}} a_{pj} \quad . \tag{2.5}$$

Inevitably, this method produces a non-uniform probability matrix for each scatter coincidence, since the probability assigned to each voxel corresponds to the number of b-LORs crossing that voxel. This means that voxels in the zone of higher b-LOR density will have a higher probability in comparison with voxels in low b-LOR density areas. This effect is obvious in Figure 2-7-(i) and (ii). Figure 2-8 also shows the corresponding probability image (a row of the system matrix) of the single-scatter coincidence discussed in Figure 2-5.

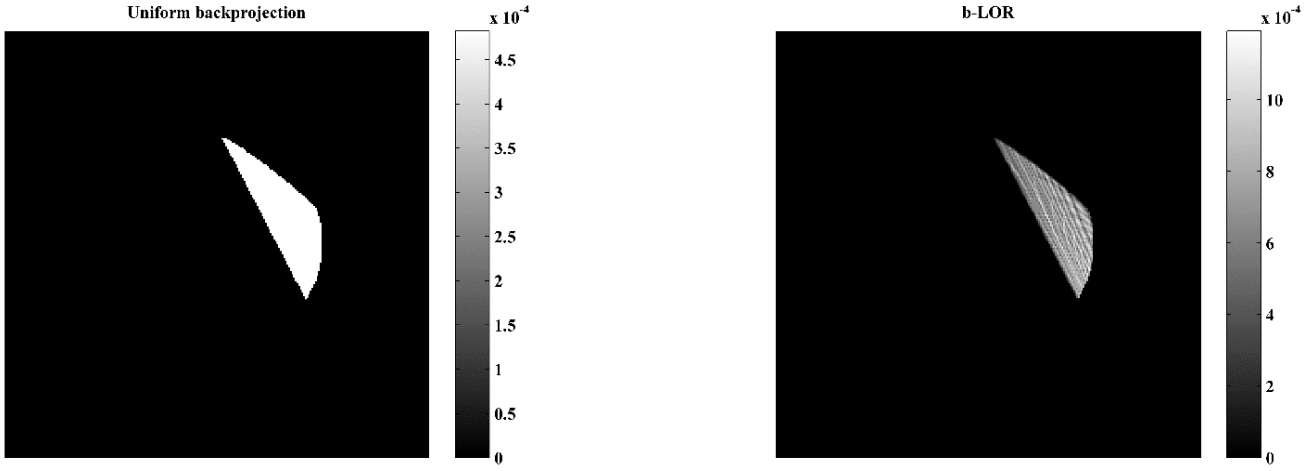

Figure 2-8. Probability images for different type of backprojections. The image on the left is generated for the previously explained sample single-scatter event using uniform projection/backprojection and the right image shows the same probability image when the b-LOR technique is applied. Note that the b-LOR technique essentially generates a non-uniform probability image for each single-scatter coincidence.

2.2.4 Attenuation Correction

Compensation for attenuation effect was done for each reconstruction method consistently. For the algorithm with uniform projection/backprojection an attenuation correction technique was previously developed by our group and published in (69) for 2D PET. Based on this technique, an attenuation coefficient for each single-scatter event is defined by averaging over possible b-LORs. The attenuation coefficient, *Att*, can be written as

$$Att = \frac{\sum_{i=1}^{P} e^{-\left(\sum_{A}^{S_i}\mu dl + \sum_{S_i}^{B}\mu dl\right)}}{P} \quad . \tag{2.6}$$

This attenuation coefficient will be multiplied by the summation in denominator (projection) of equation (1.25). Therefore, the OPL-EM reconstruction algorithm with uniform projection/backprojection and implementation of attenuation correction can be written as

$$\overline{f}_j^{(k+1)} = \frac{\overline{f}_j^{(k)}}{\sum_{i=1}^{n} a_{ij}} \sum_{i \in T^k} \frac{1}{Att. \sum_{j=1}^{m} a_{ij}\, \overline{f}_j^{(k)}} a_{ij}, \quad \text{for } k = 1, ..., K \quad . \tag{2.7}$$

Attenuation correction for the second approach (the b-LOR approach) is more straight-forward as each b-LOR can be assumed as an independent LOR that needs to be compensated for attenuation effect. This is done similarly to conventional LOR-based AC correction in 3D PET. The only difference here is that a part of the ray has a different energy than 511 keV ($A-S_i$ lines) and requires a different attenuation correction coefficient. This issue was also considered for the attenuation coefficient calculation in equation (2.6). As briefly mentioned in Section 2.1, in order to account for all possible energies of scattered photons a 4D attenuation map for each reconstruction was generated, in which the 4th dimension is energy, starting from 350 keV to 511 keV with 10 keV increments. Careful selection of attenuation coefficients is a subtlety in scatter reconstruction algorithms. In the TOF scatter reconstruction method, explained by (2), the authors used photoelectric attenuation coefficients to generate attenuation maps, rather than total attenuation coefficient. They believe since photons have already undergone a Compton scattering, Compton attenuation coefficient should not be included in attenuation correction anymore. However, in non-TOF 2D scatter reconstruction (69), total attenuation coefficients were used in the AC step. In this work also total attenuation coefficients are used since each single-scattered photons could have undergone photoelectric interaction or even more Compton scattering at other locations.

2.3 Evaluation of the Proposed Techniques

Both types of projector/backprojector techniques implemented into OPL-EM are evaluated qualitatively and quantitatively using various simulated digital phantoms. This section provides information on the GATE simulations performed and subsequent evaluation procedures.

2.3.1 MC Simulations with GATE

This study is a proof of concept, so ideal data (ideal energy resolution and detector architecture, no random or multiple-scattered events) was used to investigate the feasibility of using scattered photons in 3D PET for image reconstruction. The data was generated by the MC code GATE V6.2 (74, 75). Details of the PET systems simulated for each reconstruction are explained in the following sections. All PET systems were simulated with detector banks of sufficient length (along the Z-axis) to cover the whole length of the phantoms used, in order to eliminate the effects of activity located outside the FOV and minimize data truncation issues. The simulated sys-

tems were all cylindrical PET systems with no gaps between the block detectors. Length and size of crystals are equivalent to real PET systems, however, the energy resolution was set at 0.1% at 511 keV to achieve near-ideal energy resolution. The crystal material of the simulated detectors was lutetium oxyorthosilicate (LSO) for all simulated PET systems and the acceptable energy window was 350-650 keV, so single-scattered photons with the maximum scattering angle of 57.32° could be recorded.

Simulations were run for a specified acquisition time, which will be stated for each phantom in the following sections. All recorded coincidences were saved in a .root format file and a C code was used to extract essential information for reconstruction. Only true and single-scatter coincidences were used and all other coincidences, including random and multiple-scattered coincidences, were ignored. The simulated phantoms were all analytically simulated, except for the two standard NEMA phantoms that were voxelized phantoms. The source in all phantoms was back-to-back 511 keV photons and the real positron emission phenomenon was ignored in simulations to remove the effect of positron range (i.e. the radioactive material was assumed to emit back-to-back 511 keV photons directly).

2.3.2 Simple Analytical Phantoms

In order to analyze the behavior of each proposed algorithm, simple analytical phantoms were used. A few small phantoms were simulated in a small animal PET system to evaluate the reconstruction techniques in a situation where attenuation effects were negligible. Several large, simple phantoms[5] were also used for qualitative evaluation of the proposed techniques, followed by analysis of images of standard small and large size NEMA phantoms.

2.3.2.1 Small Simple Phantoms

Small uniform cylindrical and rectangular phantoms were simulated in a small animal PET system, similar to a Siemens Inveon pre-clinical system (76). This cylindrical PET system consisted of 64 detector blocks (16 transaxial and 4 axial) in a circular array. Each block detector consisted of a 20×20 array of LSO crystals of size of 1.59×1.59×10 mm. The PET bore has an inner radius of 8.05 cm and provides axial coverage of 12.8 cm. The uniform cylindrical phantom was de-

[5] The term “large” here is used to show the contrast against “small” phantoms, however, the diameter of large phantoms is 14 cm which is below the average size of patients in clinical imaging. Real patient-size-imaging was evaluated through the NEMA NU-2 2007 simulation.

fined with a diameter of 3.5 cm and height of 3 cm, and the rectangular phantom was designed with the size of 2×4 cm along XY plane and 3 cm length along the axial direction. Both phantoms were placed at different locations including centre and off-centre of the imaging system.

The same simulated PET system was used for small animal NEMA NU-4 2008 study as well (explained in Section 2.3.3)

2.3.2.2 Large Simple Phantoms

The PET system used in this section was a cylindrical PET system with an inner diameter of 11 cm. The PET system consisted of 9 rings of detector blocks and each detector block had the size of 2×2 cm along XY plane with 3 cm depth, comprised of a 10×10 array of LSO crystals of size of 2×2×30 mm. The axial coverage of the PET system was 18 cm. As mentioned earlier, the source in this simulation was also back-to-back 511 keV photons to eliminate positron range effects.

Images were reconstructed into the matrix size of 128×128×9 yielding a voxel size of 0.17×0.17×1.67 cm. Voxel size varies significantly along XY and Z directions to keep the reconstruction time low while the reconstruction is still 3D. For the sections where quantitative analysis was needed, however, reconstructions were done using a larger number of slices.

To see the effect of blurring, due to backprojection in a large area (rather than a line), analysis of the line spread function (LSF) was done by imaging a line source in a uniform water-filled cylindrical phantom as the scattering medium. The rod source was simulated as a cylindrical source with the diameter of 0.2 mm and length of 15 cm, filled with 37 MBq activity. This radioactive rod was located in the middle of a large water-filled cylinder with diameter of 14 cm and length of 15 cm.

Using the same water-filled cylinder, the next phantom was generated by locating two radioactive rods (each filled with 18 MBq activity) with a diameter of 2 cm at distance of 3.5 cm from the center of the cylinder on X-axis and opposite each other.

To evaluate the performance of attenuation correction, the water-filled cylinder was filled with 37 MBq activity uniformly. Finally, 37 MBq activity was distributed over the water-filled cylinder and 3 hot rod sources with diameters of 3, 10, and 20 mm and one cold rod source with a diameter of 20 mm were located at a distance of half the radius of the water-filled phantom on X-

and Y-axes. The hot-to-background activity ratio of 5 was chosen for all hot rod sources (similar to the other scatter reconstruction paper, (1)).

Figure 2-9 illustrates schematics of all mentioned phantoms in this section.

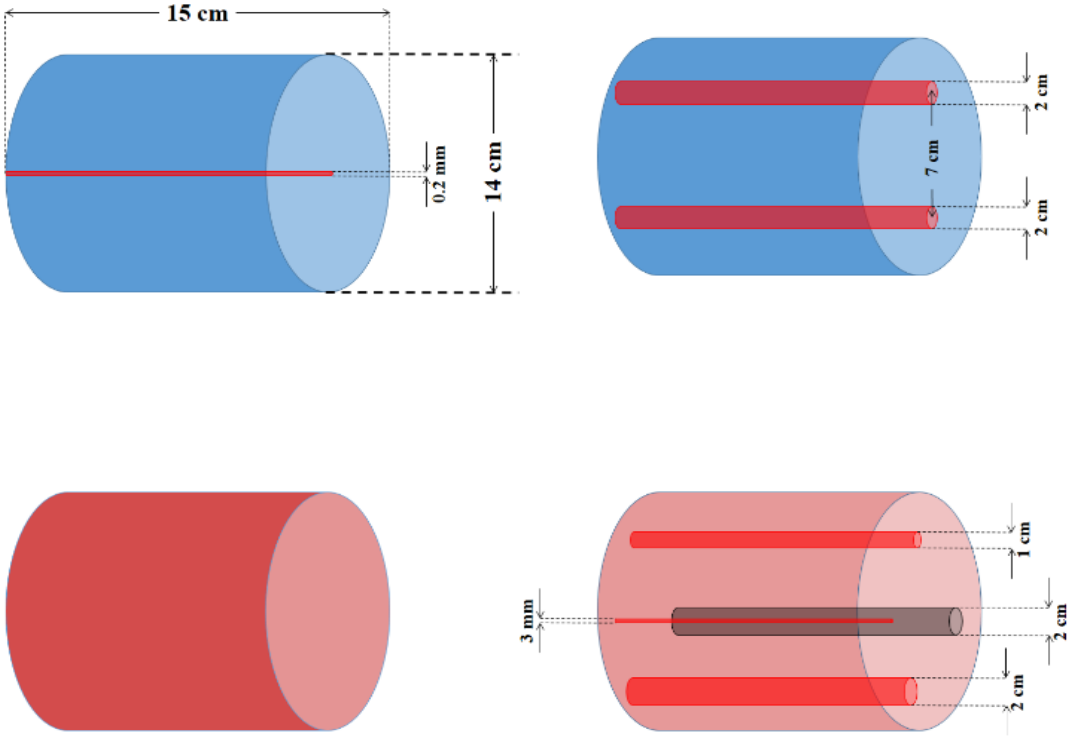

Figure 2-9. Simulated digital phantoms for qualitative analysis of different scatter reconstruction techniques. In these images blue shows non-radioactive water-filled cylinder, red shows hot area, and black shows cold area.

2.3.3 Standard NEMA NU-4 2008 Phantom

In order to perform a quantitative evaluation on the proposed image reconstruction techniques, the small size NEMA NU-4 2008 phantom was used. This is based on a standard guideline for performance evaluation of small animal PET systems published by National Electric Manufacturers Association (77). The phantom is cylindrical with a diameter of 33.5 mm and length of 63 mm and consists of three parts for various performance evaluations. The upper part of this phantom consists of five hot rods with diameters of 1, 2, 3, 4, and 5 mm in a non-radioactive water background and is used for resolution recovery coefficient (RC) evaluation. Based on the NEMA guideline, in order to find the RC, the image slices covering the central 10 mm length of the rods were averaged first to obtain a single image slice of lower noise. Then circular regions of interest

(ROIs) with diameters twice the physical diameter of the rods were drawn and the maximum values in each ROI and the corresponding pixel index were recorded. Using the recorded pixel coordinates, the line profiles of rods along the axial direction were created. Finally, the pixel values measured along each profile, divided by the mean activity concentration found in the middle part of the phantom (explained later) was used to determine the RC for each rod size. The standard deviation of the recovery coefficients was calculated as

$$\%STD_{RC} = 100 \times \sqrt{\left(\frac{STD_{LineProfile}}{Mean_{Line\,Profile}}\right)^2 + \left(\frac{STD_{Background}}{Mean_{Background}}\right)^2} \tag{2.8}$$

where "background" activity is calculated in the middle part of the phantom.

The middle part of the phantom is the uniform part and is to be used for uniformity test and noise measurement. A cylindrical volume of interest (VOI) with a diameter of 22.5 mm and length of 10 mm was drawn over the center of the uniform region of the phantom. The standard deviation of activity within the VOI was used to evaluate the uniformity.

The lower part of the phantom contains two cold cylinders, both with a diameter of 8 mm. One of these cylinders contains non-radioactive water and the other one air, and they are both surrounded by radioactive water as a background activity. This part of the phantom is to be used for accuracy of attenuation and scatter correction methods. In order to do that, two cylindrical VOIs with diameter of 4 mm and length of 7.5 mm encompassing the central parts of the cold cylinders were drawn. The ratio of the mean in each VOI to the mean of the uniform area was used to calculate spill-over-ratio (SOR) and the standard deviation was calculated in the same manner as that of the RC calculations, as shown in equation (2.8).

A high resolution voxelized digital phantom was defined as instructed in (77) and used in GATE simulation. The phantom was filled with 370 MBq activity. It is important to note that the activity concentration was the same all over the phantom. Figure 2-10 shows the CT and activity map of the simulated NEMA NU-4 2008 phantom.

Using the simulation package GATE, image acquisition was done for almost 12 minutes (during approximately 4 days of simulation). True and single-scatter events were then extracted to use in

the reconstruction algorithms. The PET system used here was the same animal PET system as explained Section 2.3.2.1.

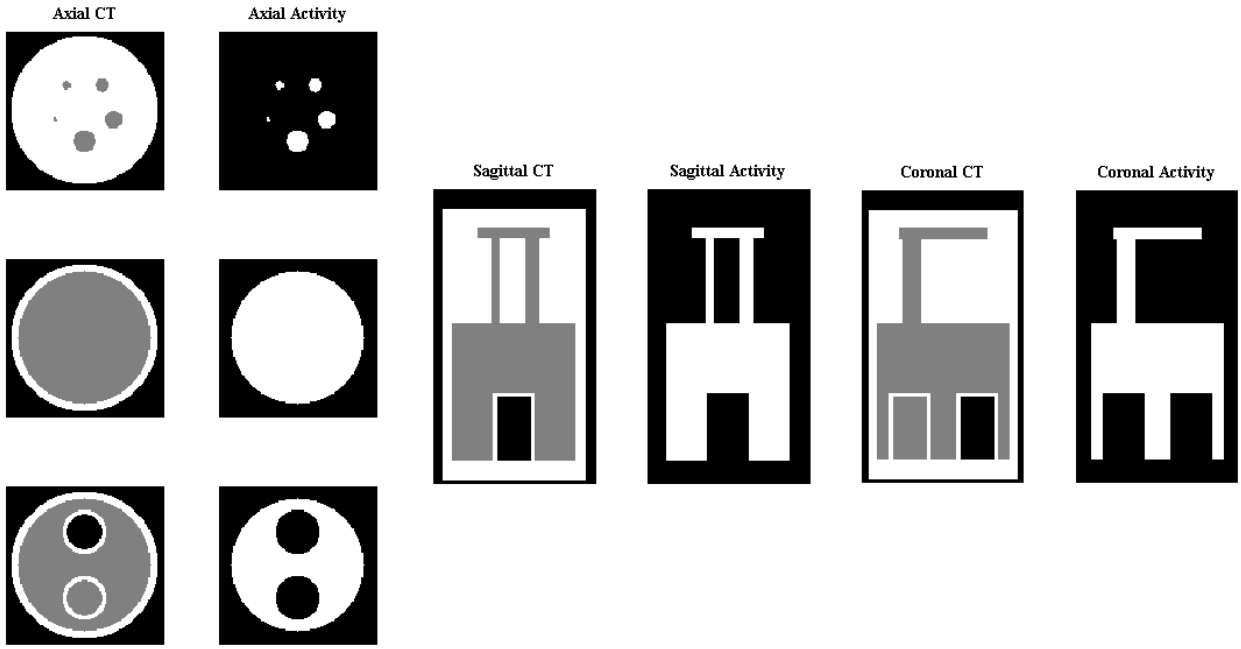

Figure 2-10. Anatomical and activity map of the small NEMA NU-4 2008 phantom. The first column shows CT images of the upper part, mid-part, and lower part of the phantom from top to bottom. The second column shows corresponding activity maps of the anatomical images in the first column. Images in other columns, show sagittal CT, sagittal activity map, coronal CT, and coronal activity map from left to right.

2.3.4 Standard NEMA NU-2 2007 Phantom

The large size NEMA NU-2 phantom was simulated to evaluate the performance of the proposed scatter reconstruction techniques in an idealized clinical situation, where attenuation is a major image degrading factor. The standard guideline for phantom generation and image quality assessment is published by National Electric Manufacturers Association (78). A high resolution voxelized phantom was generated based on the guideline and used in MC simulation with GATE. The rectangular cuboid encompassing the NEMA phantom has the size of 30×23 cm in the transverse plane and 22 cm along the axial direction. The phantom was filled with 370 MBq radioactive water (source directly emitted back-to-back 511 keV photons) and 4 hot spheres with diameters of 10, 13, 17, and 22 mm were filled with the hot-to-background activity ratio of 4. The two largest spheres (diameter: 28 and 37 mm) were assumed to contain non-radioactive wa-

ter and the cylindrical lung insert at the middle of the phantom was filled with air. Figure 2-11 shows the CT and activity map of the NEMA NU-2 2007 phantom used in this section.

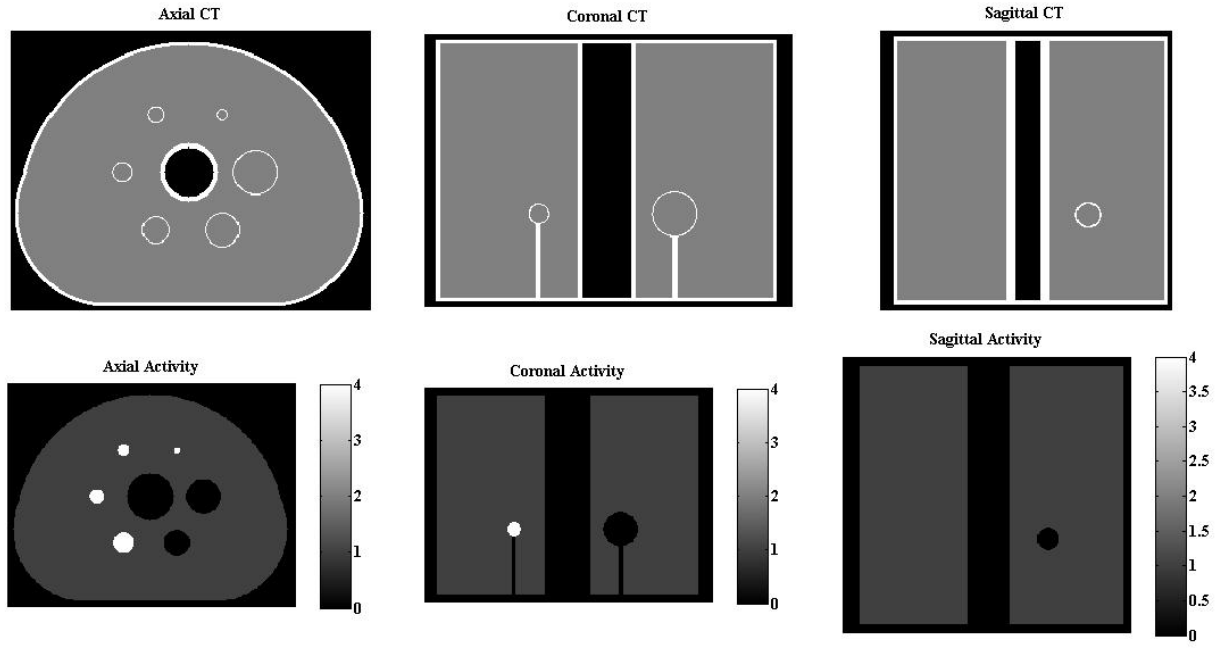

Figure 2-11. Anatomical and activity map of the NEMA NU-2 2007 phantom. The upper row shows axial, coronal and sagittal slices of anatomical images from left to right and the bottom row represents corresponding activity map of anatomical images shown in the upper row.

Based on the guideline (78), the transverse images centered on the spheres were used in quantitative analysis. ROIs with the same diameter as the inner diameter of spheres were drawn on spheres in reconstructed images. For each hot and cold sphere, 60 ROIs (12 ROIs in 5 slices as close as possible to either side of the central slice) on the background were drawn with the same diameter as the sphere, at a distance of 15 mm from the edge of the phantom, but no closer than 15 mm to any sphere. The average counts in each ROI was recorded and the percentage contrast $Q_{H,j}$ for each hot sphere j was calculated by

$$Q_{H,j} = \frac{C_{H,j}/C_{B,j} - 1}{a_H/a_B - 1} \times 100\% \tag{2.9}$$

where $C_{H,j}$ is the average counts in the ROI for sphere j, $C_{B,j}$ is the average of the background ROI counts for sphere j, a_H is the activity concentration in the hot spheres, and a_B is the activity concentration in the background.

The percentage contrast $Q_{C,j}$ for each cold sphere j was also calculated by

$$Q_{C,j} = \left(1 - \frac{C_{C,j}}{C_{B,j}}\right) \times 100\% \tag{2.10}$$

where $C_{C,j}$ is the average counts in the ROI for sphere j and $C_{B,j}$ is the average of the background ROI counts for sphere j.

The percentage background variability N_j for sphere j was calculated as

$$N_j = \frac{SD_j}{C_{B,j}} \times 100\% \tag{2.11}$$

where SD_j is the standard deviation of the background ROI counts for sphere j which is given by

$$SD_j = \sqrt{\sum_{k=1}^{K} \left(C_{B,j,k} - C_{B,j}\right)^2 \Big/ \left(K-1\right)} \quad ,K = 60 \tag{2.12}$$

Finally a circular ROI, 30 mm in diameter, was centred on the lung insert in each slice to be used in attenuation and scatter correction evaluation. The average pixel value within the ROI, $C_{lung,i}$, for each slice i was recorded and the residual error was calculated as follows

$$\Delta C_{lung,i} = \frac{C_{lung,i}}{C_{B,i}} \times 100\% \tag{2.13}$$

where $C_{lung,i}$ is the average counts in the lung insert ROI and $C_{B,i}$ is the average of the 60 37-mm background ROIs drawn for image quality analysis. The average of these errors over all slices then was calculated to report the residual error (equivalent to SOR) for each reconstructed image.

Simulation was executed for 10 minutes (during approximately 4 days of simulation) of acquisition time. True and single-scatter coincidences were used for image reconstruction. The simulated PET system was a cylindrical PET system with 25.5 cm inner diameter gantry bore and 28 cm length along the axial direction (Z-axis). The PET system consisted 14 rings of detector blocks and each detector block was made of 5×5 array of LSO crystals with the size of 4×4×25 mm. The axial coverage of the PET system was 28 cm and the phantom was located at the center of FOV.

2.4 Statistical Analysis and Computer Programming

A program was written in C to extract unscattered and scattered coincidences from the "root" files generated by GATE as a result of each simulation. All reconstruction algorithms were written in C and linked to MATLAB through a MEX file and reconstructions were run on a 16-node cluster system. Algorithms for quantitative analysis and demonstration of reconstructed images were written in MATLAB.

In order to explain quantitative differences in image quality factors with different means and standard deviations, a two-tailed t-test was done on each set of images. The confidence level was set to 90% and the t-value and degree of freedom (*d.o.f*) were calculated using equations (2.14) and (2.15), respectively (the guideline for statistical analysis was taken from (79)).

$$t = \frac{\bar{X}_1 - \bar{X}_2}{\sqrt{\frac{s_1^2}{n_1} + \frac{s_2^2}{n_2}}} \tag{2.14}$$

$$d.o.f = \frac{\left(\frac{s_1^2}{n_1} + \frac{s_2^2}{n_2}\right)^2}{\frac{\left(\frac{s_1^2}{n_1}\right)^2}{n_1 - 1} + \frac{\left(\frac{s_2^2}{n_2}\right)^2}{n_2 - 1}} \tag{2.15}$$

where *t* is the t-test value, $\bar{X}_1$ and $\bar{X}_2$ are mean values of the first and second groups, s_1 and s_2 are the standard deviations of the first and second groups, and n_1 and n_2 are the number of elements in the first and second groups. Degree of freedom was rounded to the closest integer and the corresponding *p*-value value then found using available look-up tables at (79). *P*-values greater than 0.1 were considered to be unable to reject the null hypothesis of "no significant statistical changes between two groups."

3 Chapter Three: Results and Discussion

In this chapter, simulation results for the small and large simple analytical phantoms will be shown and discussed, followed by quantitative analysis for simulation of imaging the NEMA NU-2 and NEMA NU-4 phantoms.

It is important to consider that the scatter reconstructed images (images purely based on scattered photons) shown in this chapter should only be considered as a rough representation of activity distribution and are not expected to have the same quality level as images reconstructed with unscattered coincidences. These images are shown to investigate the potential benefits of image reconstruction when the proposed techniques are implemented along with conventional techniques for unscattered (true) events. Therefore, scatter reconstructed images can merely be used for analysis of behavior of the proposed scatter reconstruction algorithm, and not for quantitative purposes of any kind. It is important to consider that in a clinical setting, it is difficult if not impossible to distinguish single-scatter events from other coincidences, so reconstruction purely based on scattered events likely has little value.

3.1 Analytical Simple Phantoms

These phantoms are first reconstructed with true coincidences as reference images (for demonstration purposes only, and not for quantitative purposes), and then with single-scatter coincidences to allow for analysis of the proposed algorithms.

All large size analytical phantoms were reconstructed on a 128×128×9 matrix using the one-pass list-mode expectation-maximization (OPL-EM) technique, with 40 subsets for the scatter-free images and 60 subsets for the scatter reconstructed images. Twenty million (2×10^7) true events and around 3.5×10^6 single-scatter events were used for reconstruction of scatter-free and scatter reconstructed images, respectively.

Table 3-1 shows the reconstruction time spent for each large size analytical phantom. In this table, the reconstruction time is reported for the case where attenuation correction (AC) was employed in reconstruction algorithms and rounded to the nearest integer in hours.

Table 3-1. Reconstruction time (in hours) spent for scatter reconstructed images of large size analytical phantoms.

	Line source in a water-filled cylinder	Uniform cylindrical phantom	Two hot rods in a water-filled cylinder	Three hot and one cold rods in a water-filled cylinder
Scatter reconstruction time (uniform/b-LOR approach) (hours)	56 / 79	49 / 62	54 / 66	63 / 78

The number of single-scatter events varies between different reconstructions, since the number of generated single-scatter coincidences in each GATE simulation was different. Scatter-only images are reconstructed with a higher number of subsets, although a smaller number of events are used. That is because the convergence rate is much slower in scatter-only reconstructions (because of backprojection over areas rather than lines). Nevertheless, the subset number is selected empirically and based on visualization only.

Figure 3-1 shows the central slices and horizontal profiles of the line source (radioactive rod source) in the uniform water-filled cylindrical phantom. The images shown in Figure 3-1 were compensated for attenuation effects (in this and many following figures central slices, along Z-axis, of the reconstructed images are shown only).

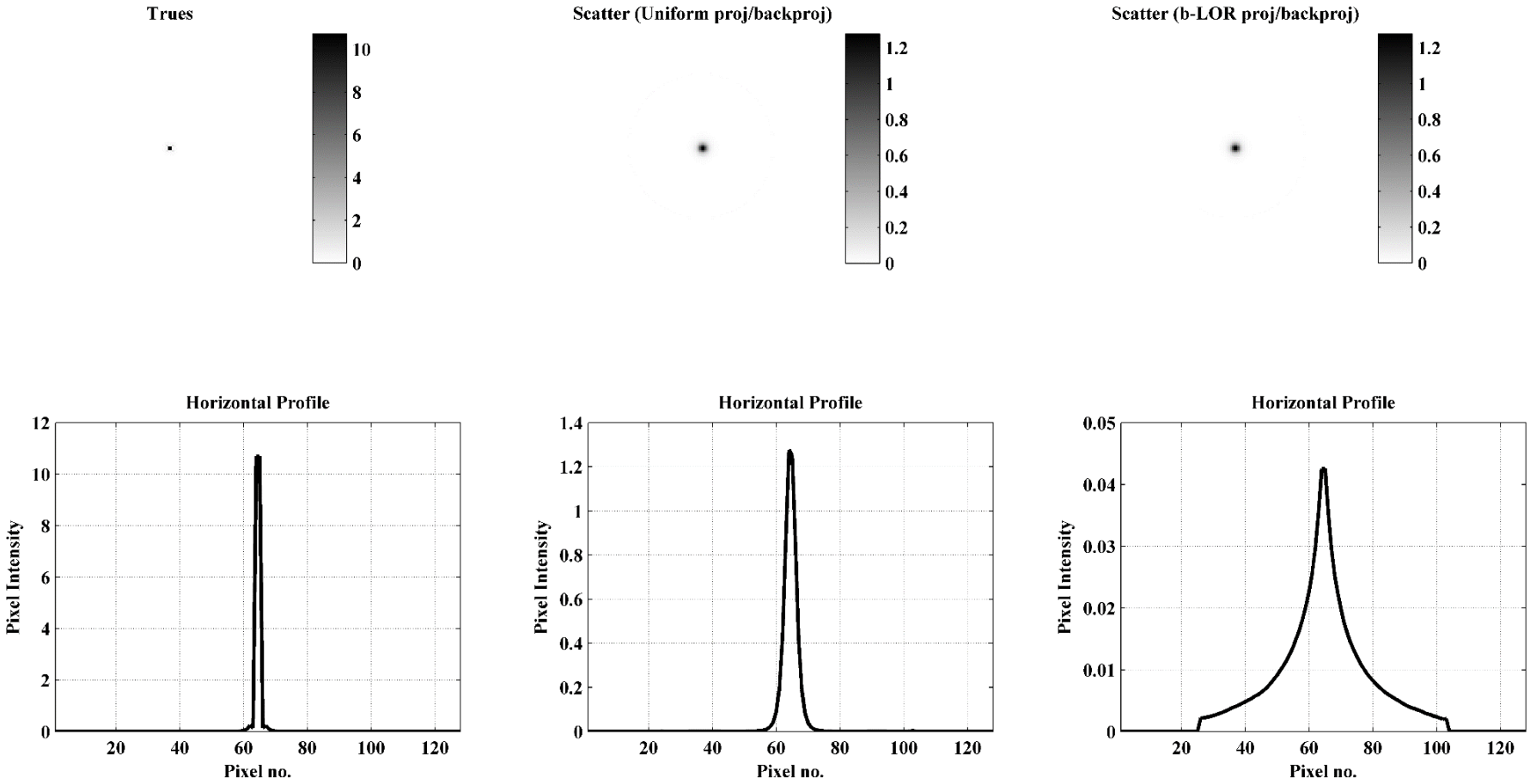

Figure 3-1. Central reconstructed images and their horizontal mid-profiles of the line source phantom. From left to right, the first column shows image and profile of the scatter-free case, the second column corresponds to the scatter reconstructed image when the uniform approach was used, and the last column shows the image and profile of the scatter reconstructed image when the b-LOR technique was used.

Backprojection over areas in proposed scatter reconstruction techniques causes blurring in scatter reconstructed images. However, as shown in the broken-line-of-response (b-LOR) scatter reconstructed image, the b-LOR approach introduces a higher degree of blurring in comparison with the uniform projection/backprojection method. Although the backprojection area for each single-scatter event is identical in both scatter reconstruction techniques, non-uniform backprojection in the b-LOR technique is the main reason for the broad line spread function, as shown in the corresponding image profile. Areas outside the phantom boundary have pixel values of zero, since all reconstructions accounted for the phantom outline. Further quantitative analysis, such as full-width half-maximum (FWHM) or modulation transfer function (MTF), was not performed on these images due to the low resolution reconstruction matrix size and relatively low count statistics used in the reconstructions.

Figure 3-2 shows images reconstructed based on unscattered and scattered events of the uniform non-radioactive water-filled cylindrical phantom with two hot rods inside.

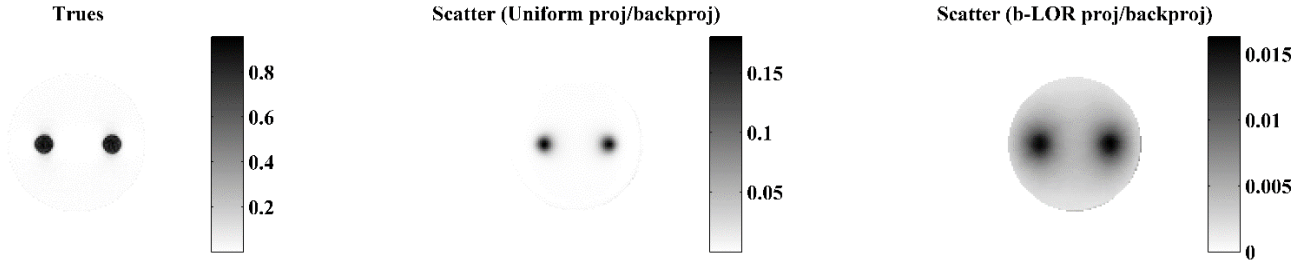

Figure 3-2. Reconstructed images of the uniform water-filled cylindrical phantom with two hot rods. From left to right, images are reconstructed by using true events only, scattered events with the uniform approach, and scattered events with the b-LOR approach.

Consistent with images and profiles shown in Figure 3-1, the b-LOR method resulted in a highly blurred image, while reconstruction with the uniform approach yielded a less blurred image with lower background activity.

Figure 3-3 shows the images and corresponding horizontal profiles of the uniform cylindrical phantom (diameter: 14 cm, length: 15 cm). This series of reconstructions was done with and without AC to further evaluate the effectiveness of the proposed AC techniques.

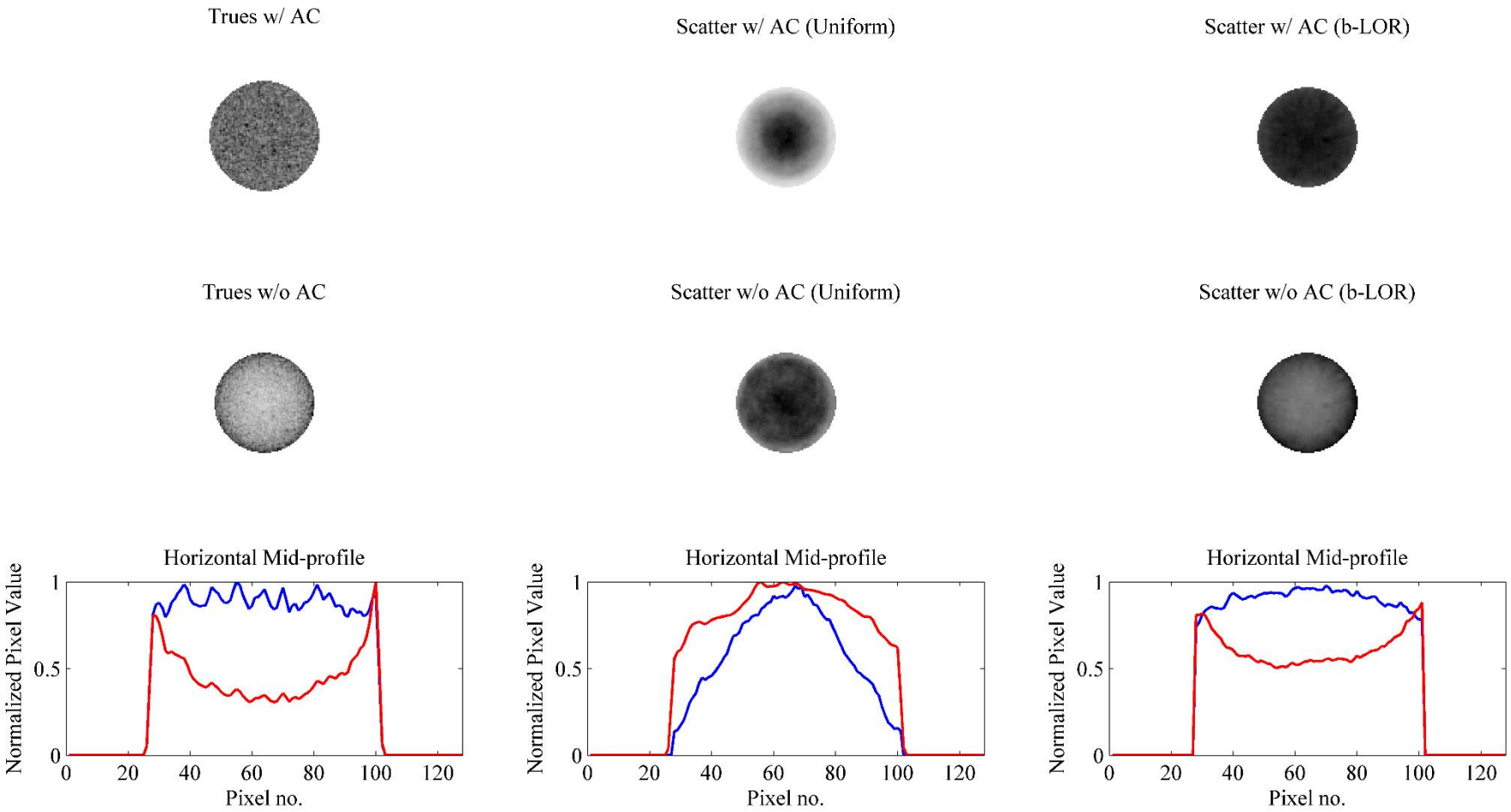

Figure 3-3. Reconstructed images and horizontal profiles for the central slice of the uniform cylindrical phantom. In columns from left to right, images and profiles are for the scatter-free case (true coincidences only), uniform scatter reconstruction and b-LOR scatter reconstruction. The first and second rows show images reconstructed with and without attenuation correction, respectively, while the third row shows profiles through the center of the images. In the profiles, the blue line is the profile of the attenuation corrected image while the red line is the profile of the image without compensation for attenuation effects.

The profiles of the images reconstructed with true events in this figure show the importance of attenuation correction for this phantom. While the profile of the attenuation corrected image shows a relatively flat line, the profile of the image without AC clearly shows activity underestimation in the central part of the phantom. Reconstruction of scattered events with implementation of the uniform projection/backprojection method has led to an inhomogeneity in the image. This also happened for the image without AC, although AC made the non-uniformity more severe. The inhomogeneity can be interpreted as an activity overestimation in the central area of the phantom or underestimation around the surface of the phantom. Implementation of b-LOR projection/backprojection, on the other hand, has resulted in a fairly uniform image when AC is included. Similar to the scatter-free images, not including AC in the b-LOR approach has resulted in activity underestimation in the central area of the phantom.

Figure 3-4 shows the results of the last simple large analytical phantom, a 3D water-filled cylinder with three hot rods, one cold rod, and background activity as explained in Section 2.3.2.2. As mentioned previously, the ratio of hot-to-background activity for all three hot sources was set to 5. In one simulation, the cold rod was filled with air while in another it contained non-radioactive water, to analyze both scatter reconstruction and AC techniques when dealing with different types of cold areas in terms of attenuation coefficients.

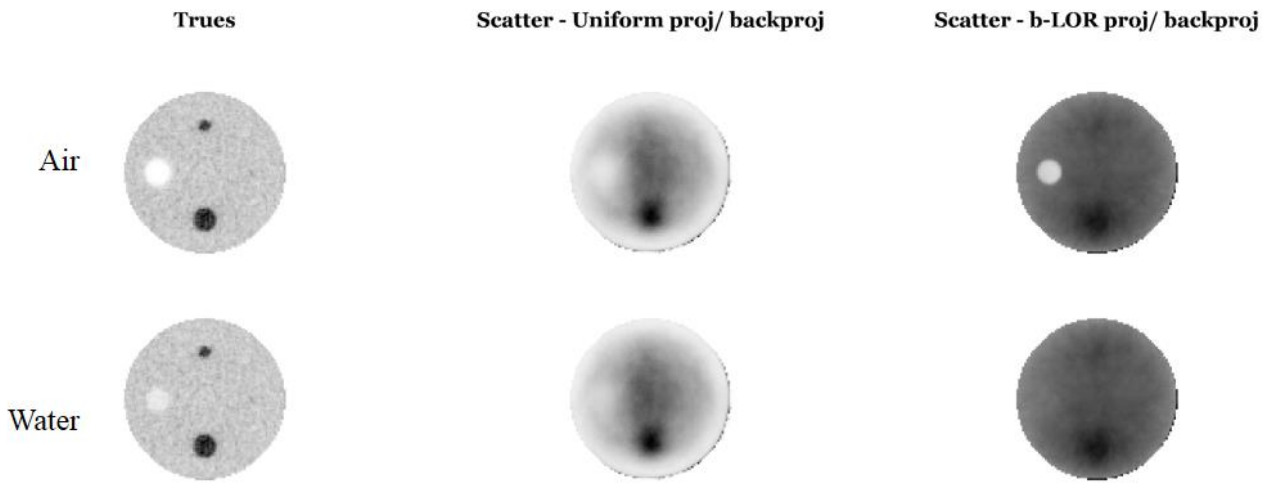

Figure 3-4. Reconstructed images of the water-filled cylinder with background activity, three hot sources, and one cold source. The top row shows images of the phantom when cold area is filled with air, and the bottom row shows images of the phantom when cold area is filled with non-radioactive water. True events were used for the images of the left hand side column, scattered events with the uniform approach for the central column, and scattered events with the b-LOR approach for the right hand side column.

In PET LOR-based image reconstruction, LORs passing through hollow cold lesions have different attenuation correction coefficient than the ones crossing dense cold lesions. So AC indeed modifies the contrast recovery coefficient (CRC) for various type of cold areas. Generally, CRC for cold lesions filled with air would be higher than that for more dense lesions (e.g. filled with water) when AC is included. This effect can be seen in the cold area of the images in the first column of Figure 3-4 (scatter-free or "trues-only" images). The same issue happens for the cold rod in scatter reconstructed images as well, however, the contrast degradation is more severe in the b-LOR approach. The contrast of hot rods is more degraded in the b-LOR approach as a result of the previously shown blurring effect of this method.

3.2 Small Analytical Simple Phantoms

Table 3-2 summarizes reconstruction parameters, number of unscattered and scattered events, and the time required for reconstruction of each of the small analytical phantoms explained in Section 2.3.2.1.

Table 3-2. Reconstruction details and parameters used for small analytical phantoms.

	Phantom size (cm)	No. of true coincidences	No. of single-scatter coincidences	Subset no. (trues/ scatter)	Reconstruction matrix size	Scatter reconstruction time (uniform / b-LOR) (hours)	Description
Small uniform cylindrical Phantom	3.5 (diameter) × 3 (length)	20,000,000	3,000,000	40 / 60	128×128×9	19 / 23	Phantom at the centre of FOV
Small uniform cylindrical Phantom	3.5 (diameter) × 3 (length)	19,000,000	3,000,000	40 / 60	128×128×9	19 / 22	Phantom shifted by 1.75 cm along X-axis
Small uniform cylindrical Phantom	3.5 (diameter) × 3 (length)	19,000,000	1,412,000	40 / 50	128×128×9	9 / 10	Phantom shifted by -1.75 cm along both X- and Y-axes
Small rectangular cuboid Phantom	4×2 (XY plane) × 3 (Z-axis)	20,000,000	1,599,000	40 / 50	128×128×9	7 / 7	Phantom at the centre of FOV
Small rectangular cuboid Phantom	4×2 (XY plane) × 3 (Z-axis)	19,500,000	1,668,000	40 / 50	128×128×9	6 / 7	Phantom shifted by 2 cm along X-axis

Figure 3-5 shows central reconstructed slice of the small uniform cylindrical phantom in the center of the field of view (FOV).

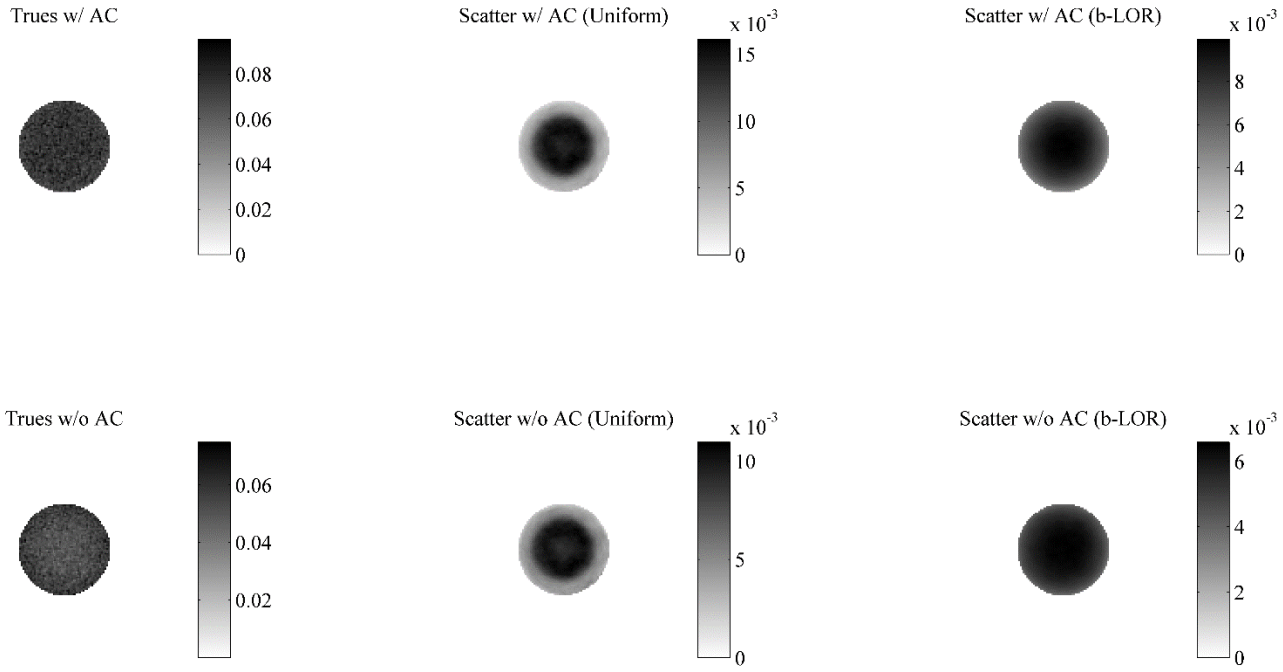

Figure 3-5. Reconstructed images of the small size uniform cylindrical phantom (central slice). The top row shows attenuation corrected images and the bottom row shows images reconstructed without compensation for attenuation. From left to right, the first column represents scatter-free images, second column shows scatter reconstructed images with the uniform approach, and third column is the scatter reconstructed images with the b-LOR technique.

Visually, this figure suggests there is no significant difference in reconstructed images with and without AC. In order to evaluate the effect of AC quantitatively, the middle horizontal profile of scatter-free images were compared in Figure 3-6. The scatter reconstructed images using the uniform projection/backprojection algorithm show higher activity concentration in the central part of the phantom and a low-pixel-count ring in the outer area. This issue can be seen in both attenuation corrected and uncorrected images. The b-LOR approach, however, provides a relatively more uniform activity distribution over the phantom. Figure 3-7 illustrates horizontal profiles of the scatter reconstructed images using both proposed techniques.

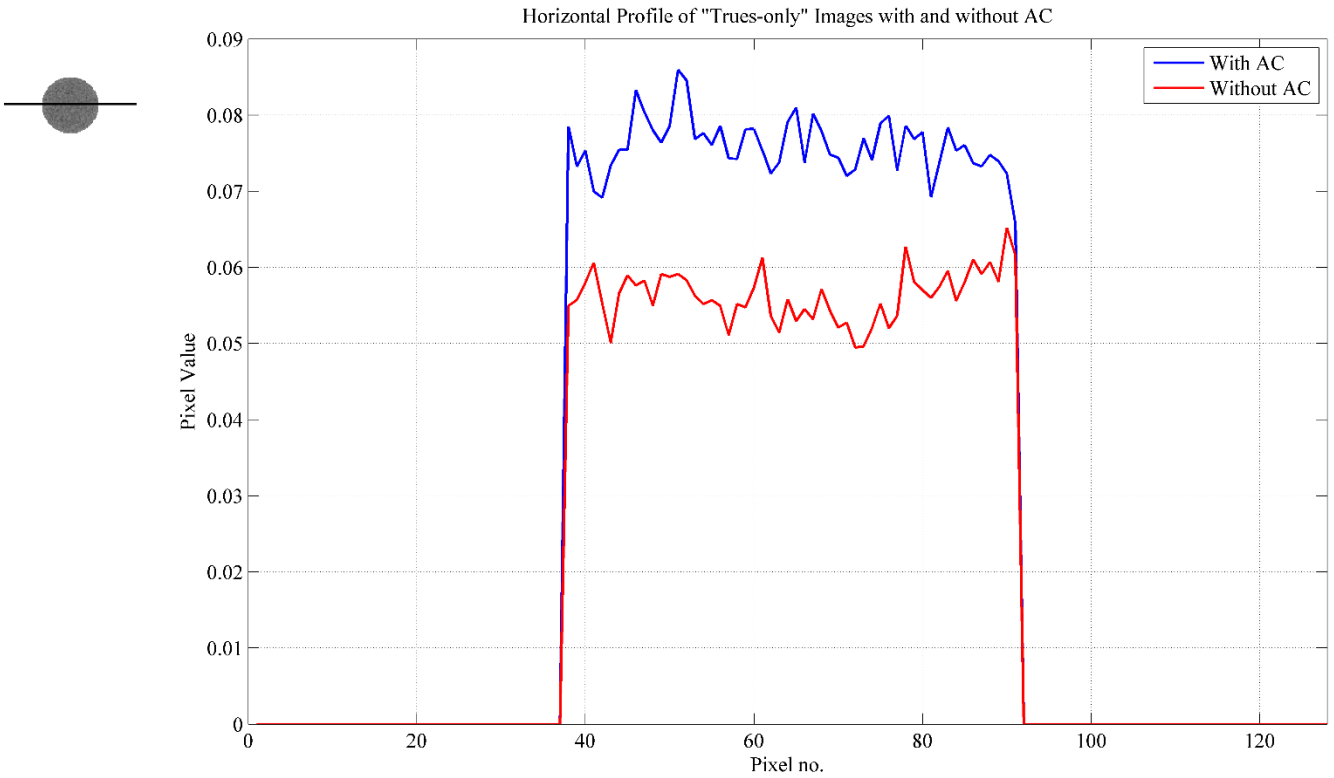

Figure 3-6. Horizontal profile of the scatter-free images with and without AC.

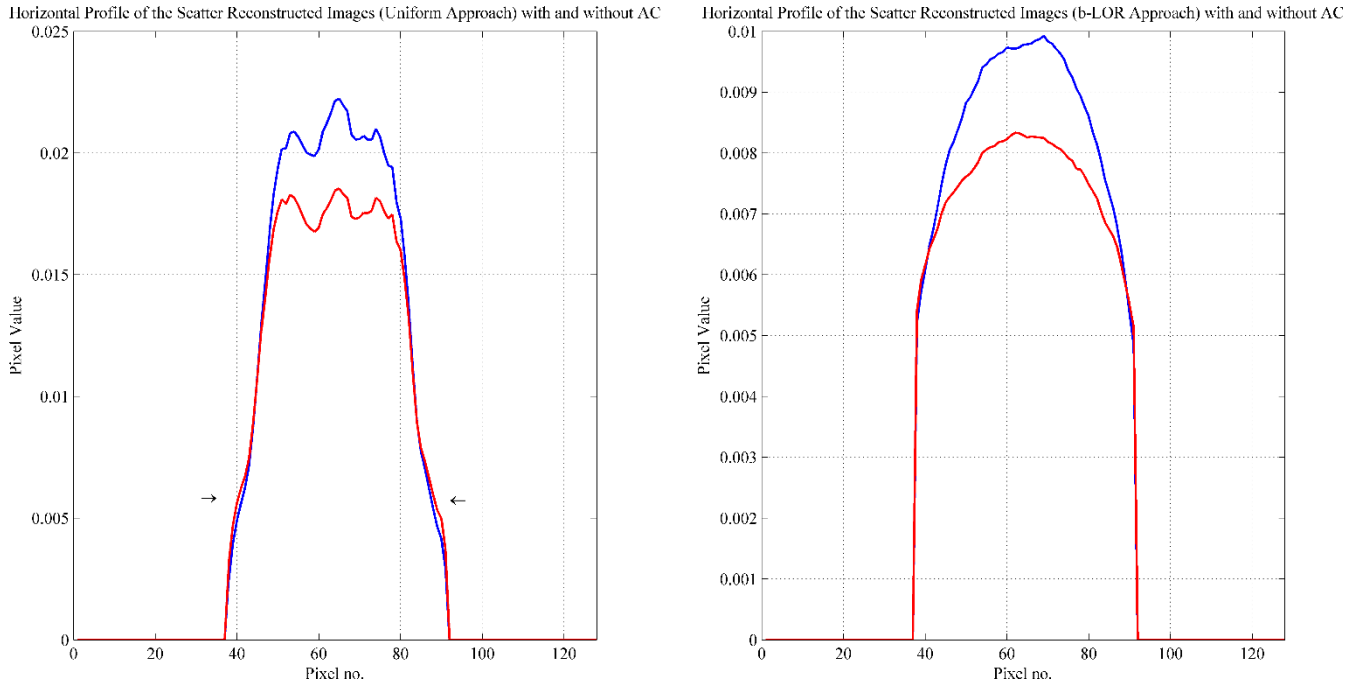

Figure 3-7. Horizontal profile of the scatter reconstructed images with and without AC for both proposed scatter reconstruction techniques.

As the profiles in Figure 3-6 show, compensation for attenuation effects has led to an increase in pixel values of the scatter-free images globally, however, the image without AC still shows a relatively uniform (although noisy) image profile. This can be used to confirm the claim that the small size of the phantom has led to negligible attenuation effects. The profiles of the scatter reconstructed images with the uniform approach (Figure 3-7) show a similar non-uniformity trend, regardless of AC being done or not, although including AC in the reconstruction algorithm has increased pixel values globally. This non-uniformity is obvious inside the profiles (shown by two arrows). Therefore, it could be concluded that the uniform projector/backprojector in scatter reconstruction introduces non-uniformity in images regardless of AC technique. The profiles regarding the b-LOR scatter reconstructed images also show that AC has led to a mild activity overestimation in the central region.

Since the sampling LOR is not uniform across the FOV of a cylindrical PET system, images of other asymmetric and off-center located small phantoms were reconstructed in order to further evaluate both proposed scatter reconstruction algorithms, particularly the uniform approach. Figure 3-8 shows the reconstructed central slice of the small uniform cylindrical phantom when set off-center. These images were compensated for attenuation effects.

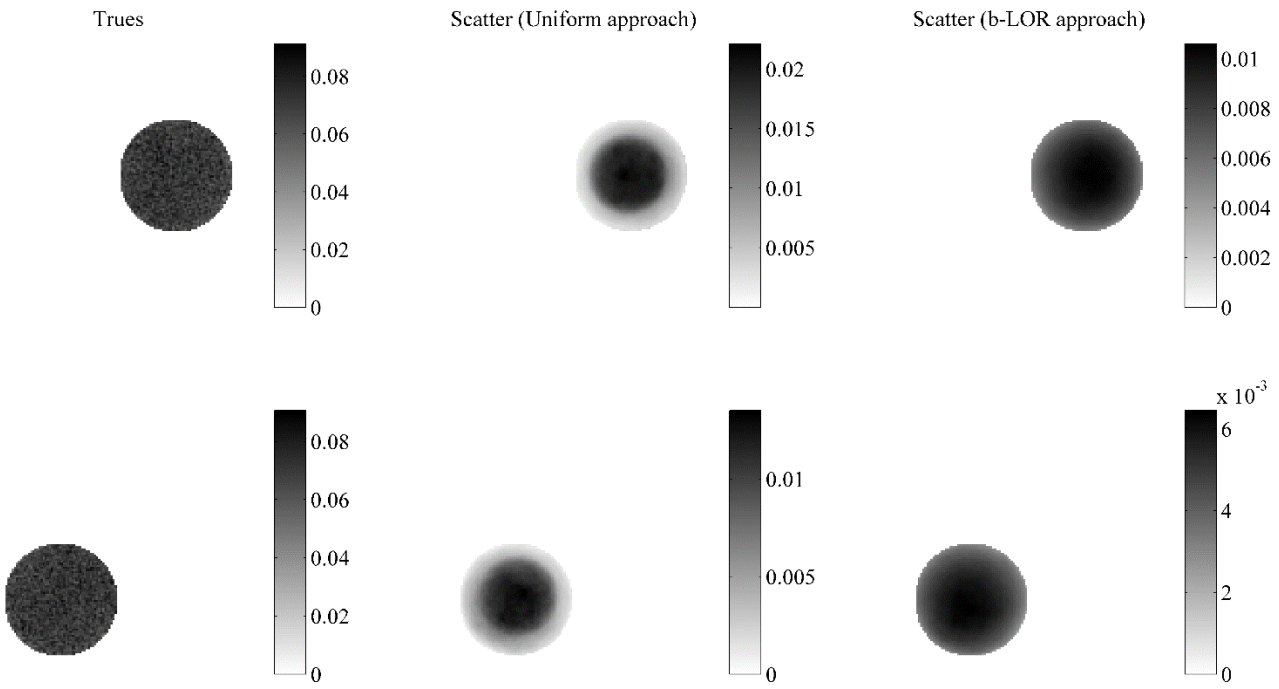

Figure 3-8. Reconstructed images of the small uniform cylindrical phantom when it was shifted by 1.75 cm along X-axis (top row) and -1.75 cm along both X- and Y-axes (bottom row). From left to right, the first column shows images of true events only, next column is scatter reconstructed images using the uniform projection/backprojection method, and the last column is the scatter reconstructed images when the b-LOR approach was used. All images are corrected for the effects of attenuation.

Images of the off-center small cylindrical phantom shows similar behavior as images of the phantom located at the center of FOV. In fact, the uniform approach has led to non-uniform images, whereas the b-LOR approach generated relatively more uniform images.

The next figure illustrates central slices of the small rectangular phantom at the center and off-center of FOV. Images shown in Figure 3-9 were reconstructed with compensation of attenuation effect.

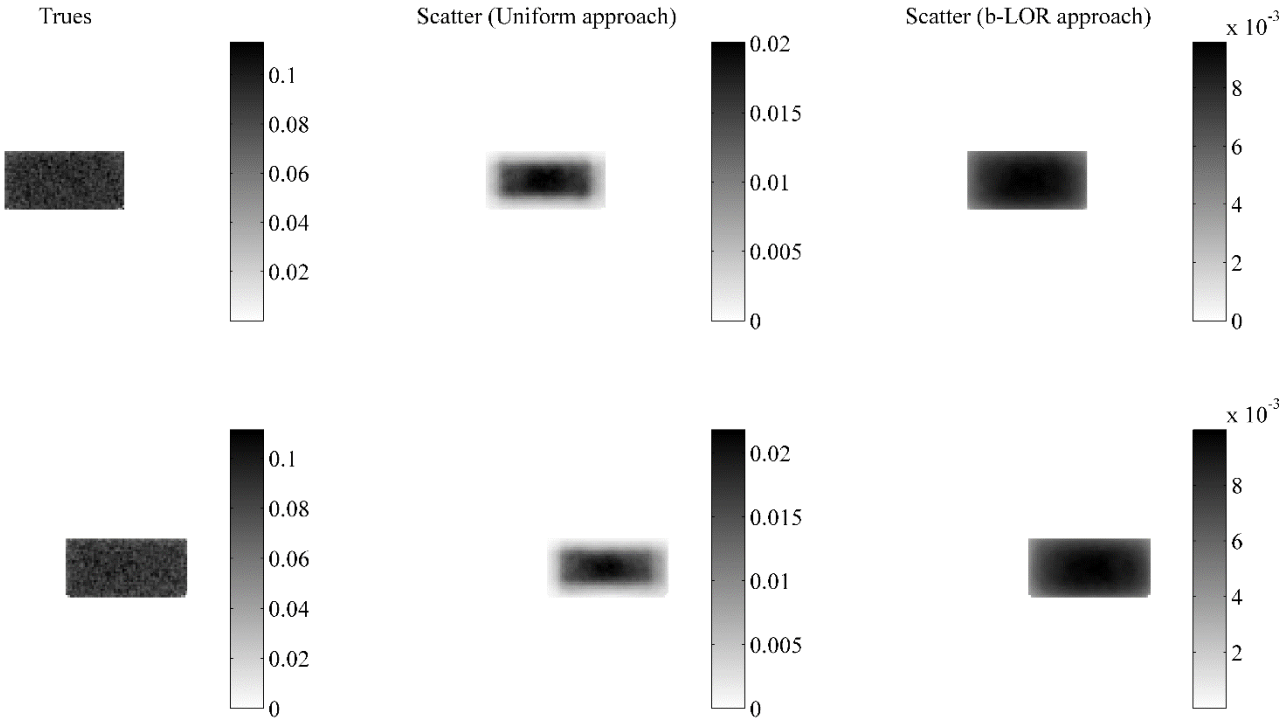

Figure 3-9. Reconstructed images of the small rectangular phantom. The top row shows images of the phantom located at the center of FOV and the bottom row shows images of the phantom when it was shifted by 2 cm along X-axis. From the left side, the first column is the images of true events only, the next column is the scatter reconstructed images when the uniform approach was used, and the last column is scatter reconstructed images when the b-LOR approach was used. All images are corrected for the effects of attenuation.

Images in this figure also show that the uniform approach has led to higher apparent activity concentration in the center of the phantom, whereas the b-LOR approach yielded more uniform images.

3.3 NEMA NU-4 2008 Image Quality Phantom

This section includes reconstructed images of the small animal NEMA NU-4 image quality phantom followed by quantitative analysis of the images. As previously explained, five different cases with 7.85×10^6 unscattered events and various scatter fractions (0%, 10%, 25%, 50%, and 75% of the unscattered events) were considered. A set of scatter reconstructed images was reconstructed for demonstration purposes only (and not for quantitative purposes of any kind). Each case was reconstructed with both proposed projector/backprojector operators into a 100×100×32 matrix, yielding a voxel size of 0.8×0.8×2.2 mm. The reconstruction technique was

OPL-EM and 40 subsets were used to reconstruct the images, except scatter reconstructed images (images based on scattered events only) that were reconstructed with 60 subsets.

In the following figures, "LM" refers to conventional list-mode reconstruction in which all recorded events (scattered and unscattered events) are assumed to be unscattered events. "Uniform GS" and "b-LOR GS" refer to the developed 3D reconstruction techniques in which the uniform and b-LOR projectors/backprojectors are used for scatter coincidences, respectively. In some of the following figures image quality factors for the ideal case of scatter-free images (trues only) are also shown. However, these images had different noise and convergence levels from the other images reconstructed with both scattered and unscattered events and therefore should not be included in a quantitative comparison. These values are only reported to show the change in the level of image quality factors if scattered photons are to be subtracted from the list of events, rather than being used in image reconstruction (while keeping the reconstruction parameters the same as before). Only images with the same number of events and same reconstruction parameters were compared quantitatively.

Figure 3-10 shows the central slice of each phantom's part of reconstructed images with true coincidences and true plus 75% scattered events when different reconstruction algorithms were used. Reconstruction time for the NEMA NU-4 2008 phantom was up to 77 hours, depending on the number of scattered events and the projection/backprojection technique used in the reconstruction algorithm.

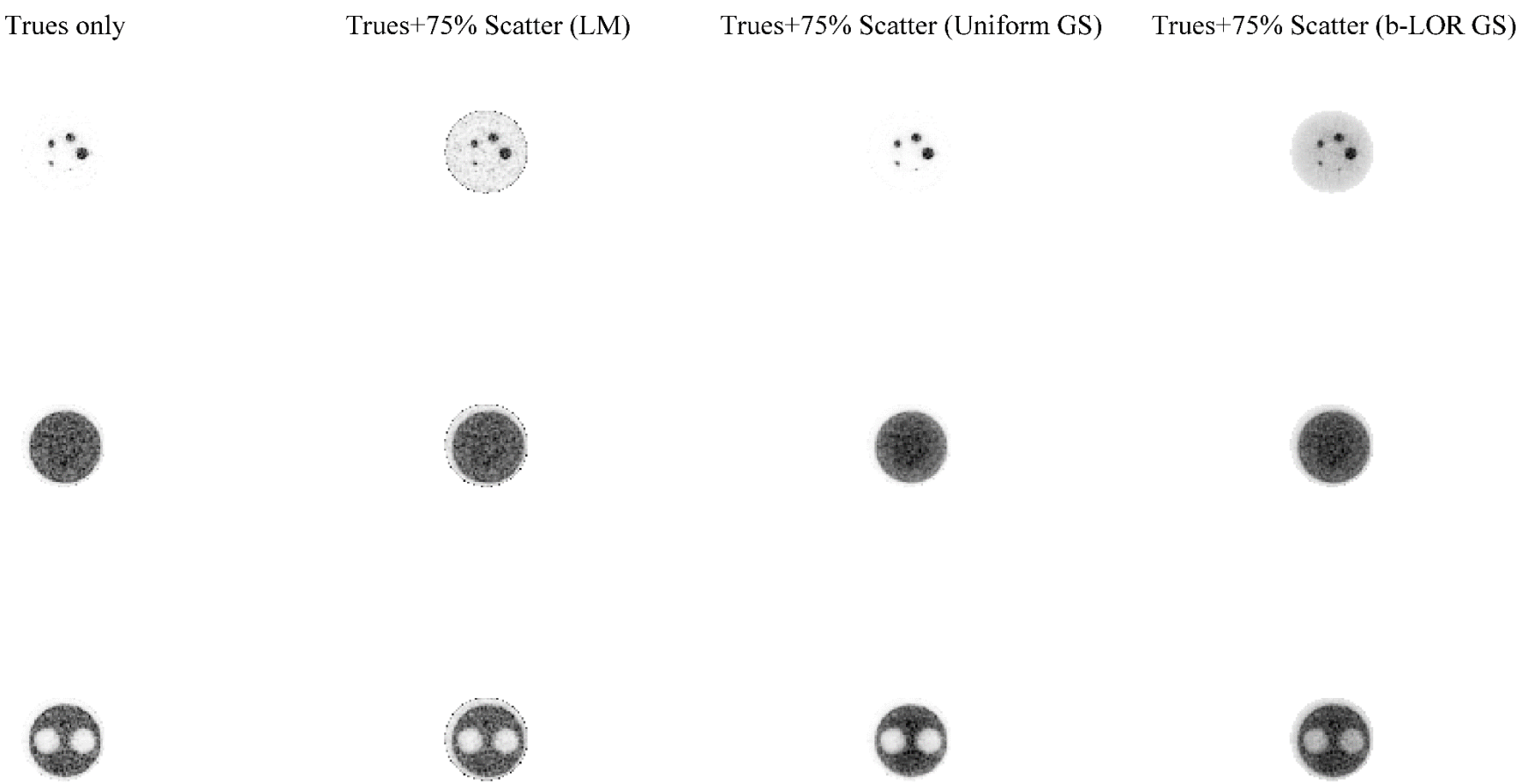

Figure 3-10. Reconstructed images of the NEMA NU-4 2008 image quality phantom when true events were used only (first column), true and 75% scattered events with conventional list-mode reconstruction technique (second column), true and 75% scattered events when the uniform projection/backprojection method was used for scattered events (third column), and true and 75% scattered events when the b-LOR projection/backprojection method was used for scattered events (last column). From the top to bottom each row represents images of the top part of the phantom containing five hot rods, uniform part of the phantom, and the bottom part containing two cold cylinders, respectively.

In this figure, images with the largest fraction of scattered events were presented to clearly show the effect of scatter projection/backprojection technique when combined with a conventional technique for true events. When comparing images of the two last columns in this figure (the uniform and b-LOR approaches) with images in the second column (LM), visually, the effect of blurring is noticeable in b-LOR reconstructed images. The blurring has severely affected residual activity in the two cold cylinders and introduced additional background activity all over the phantom. Following graphs compares image quality factors quantitatively for each set of reconstruction.

Figure 3-11 illustrates calculated resolution recovery coefficient (RC) for each rod in different reconstructed images.

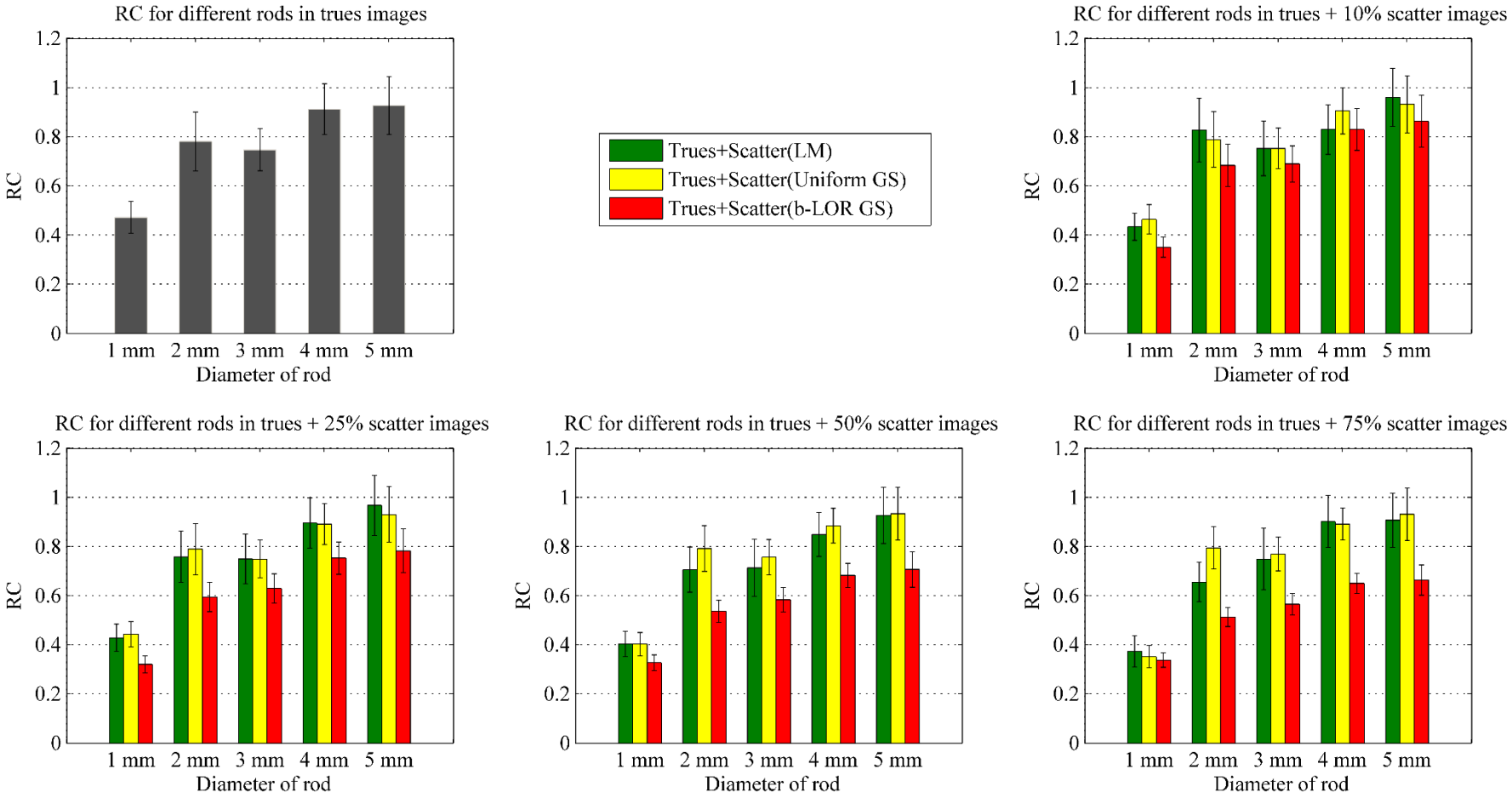

Figure 3-11. Resolution recovery coefficient (RC) for various rods in reconstructed images of the NEMA NU-4 2008 phantom with different scatter fractions. The bar graph with gray bars represents RC for scatter-free images and the other graphs illustrate RC for images with different fraction of scattered events (stated at the top of each graph) when various reconstruction techniques (different colors of bars, stated at the legend) were used.

As can be seen, neither the uniform nor the b-LOR approach is successful in increasing the RC significantly. Indeed, not only is there no significant increase in the RC, but use of the b-LOR approach has also resulted in a severely degraded RC as the scatter fraction increases. In order to have a more solid discussion on these results and statistically explain the graphs, the RC for each rod in each image was compared with that in a similar LM image using a standard statistical test. The comparison was done by performing a two-tailed t-test as explained in Section 2.4 and the calculated *p*-values are reported in Table 3-3 below.

Table 3-3. *P*-values obtained from the comparison of different rods' RC in reconstructed images of the NEMA NU-4 2008 phantom when comparing to the similar reconstructed images with conventional projection/backprojection for scattered events. *P*-values greater than 0.1 are shown in blue and less than 0.1 are shown in red background.

	Scatter fraction / Reconstruction technique							
Diameter of rod	10% / Uniform	10% / b-LOR	25% / Uniform	25% / b-LOR	50% / Uniform	50% / b-LOR	75% / Uniform	75% / b-LOR
1 mm	0.6972	0.2186	0.8419	0.1005	0.9976	0.1956	0.7665	0.5908
2 mm	0.8073	0.3315	0.8208	0.1676	0.4831	0.1002	0.227	0.1132
3 mm	0.9999	0.6105	0.9983	0.2837	0.7327	0.2832	0.875	0.1616
4 mm	0.5573	0.9995	0.9748	0.2262	0.74	0.1067	0.9317	0.0374
5 mm	0.8491	0.5066	0.8125	0.2109	0.9607	0.1063	0.8635	0.0635

In most cases *p*-values are greater than 0.1, which represents an absence of meaningful changes in the level of RC when either projection/backprojection methods were used in compare with the RC in conventionally reconstructed images. However, when a very high scatter fraction of 75% was used, resolution recovery ability for the large diameter rods deteriorated (*p*-values are 0.0374 and 0.0635 for 4 mm and 5 mm diameter rods, respectively), which is a direct result of blurring out the image.

Scatter reconstruction techniques are not expected to increase the resolution recovery ability due to backprojection over areas. However, in the ideal case, a trade-off between resolution, regularization of the image (reduction in noise level), and accurate quantification could be acceptable.

Figure 3-12 compares the percentage background variability in the uniform part of the phantom for each reconstruction trial.

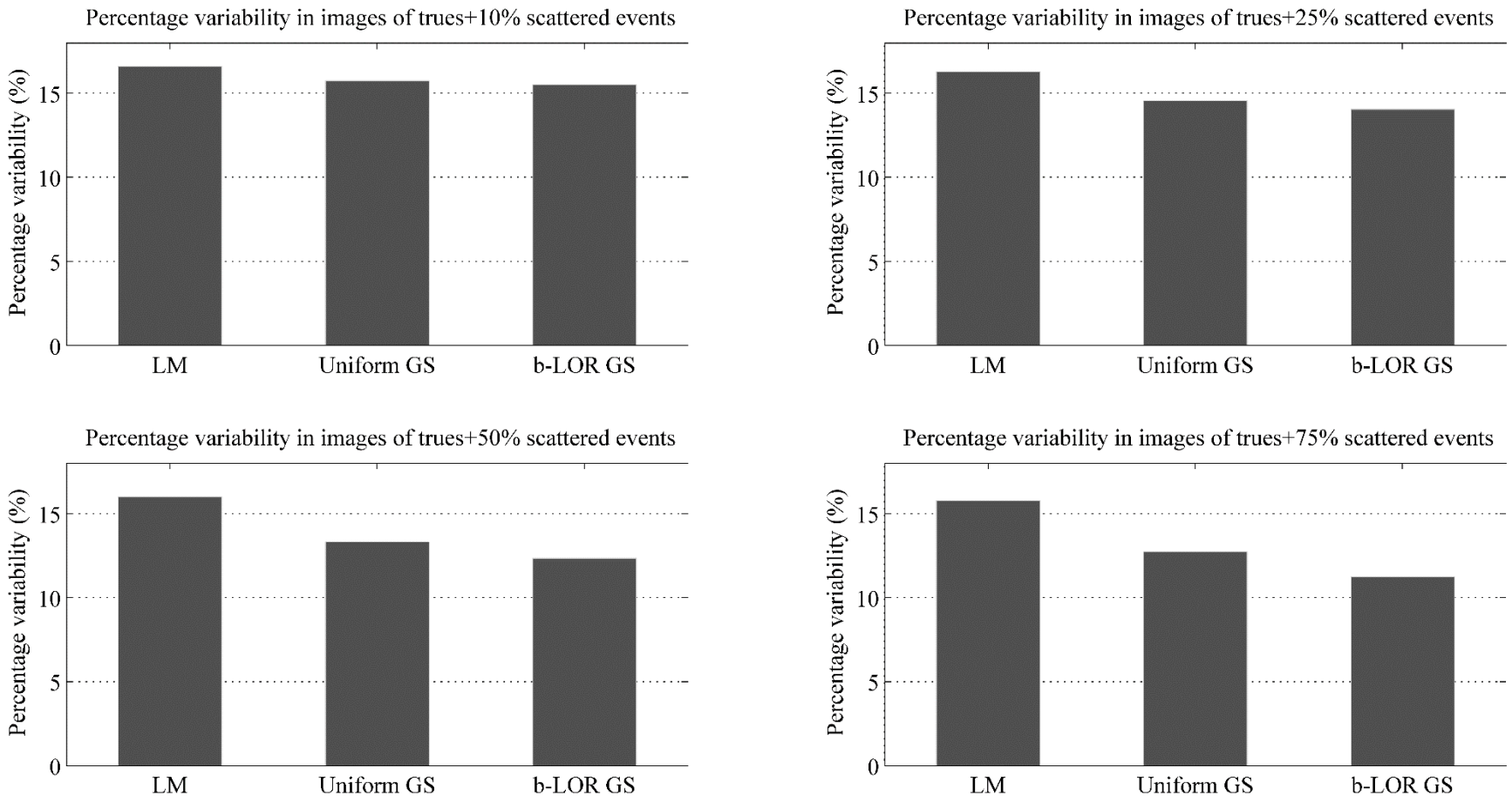

Figure 3-12. Percentage background variability of the uniform part of the NEMA NU-4 2008 image quality phantom in different reconstructed images. Corresponding scatter fraction of each bar graph is stated at the top of it, and the reconstruction technique of each bar is mentioned on the horizontal axis below the bars.

The scatter-free image had a percentage background variability of 16.8%. There is no uncertainty calculation for background variability percentage in a single acquisition based on NEMA guideline (77), hence no error bar on these graphs. These bar graphs show that both the uniform and b-LOR techniques are helpful in reduction of the background variability. The decrease becomes more significant as scatter fraction increases. When 10% scatter fraction was added to unscattered events, the uniform and b-LOR approaches reduce background variability by 5.4% and 6.6%, respectively (these are relative changes with respect to LM images and not absolute difference of background variability). Increasing the scatter fraction to 25%, 50%, and 75% led to a reduction of background variability by 11%, 16.9%, and 19.6% when the uniform approach was used, and 14.1%, 23.1%, and 29.1% when the b-LOR approach was used. The b-LOR approach yielded images with a lower background variability. The reduction of background variability is a direct result of image smoothness due to backprojection over areas. The non-uniformity of the activity distribution seen in the images reconstructed with the uniform projection/backprojection method affects the background variability. Overall, better reduction of background variability in images reconstructed with the b-LOR approach in comparison with images reconstructed with the uniform approach is due to two factors. First, the high degree of blurring in the b-LOR approach generates a more uniform image (regardless of the true activity distribution), and second, the non-uniform activity distribution seen in the uniform projector/backprojector.

Figure 3-13 illustrates calculated spill-over-ratio (SOR) in two cold cylinders in different images of the NEMA NU-4 image quality phantom.

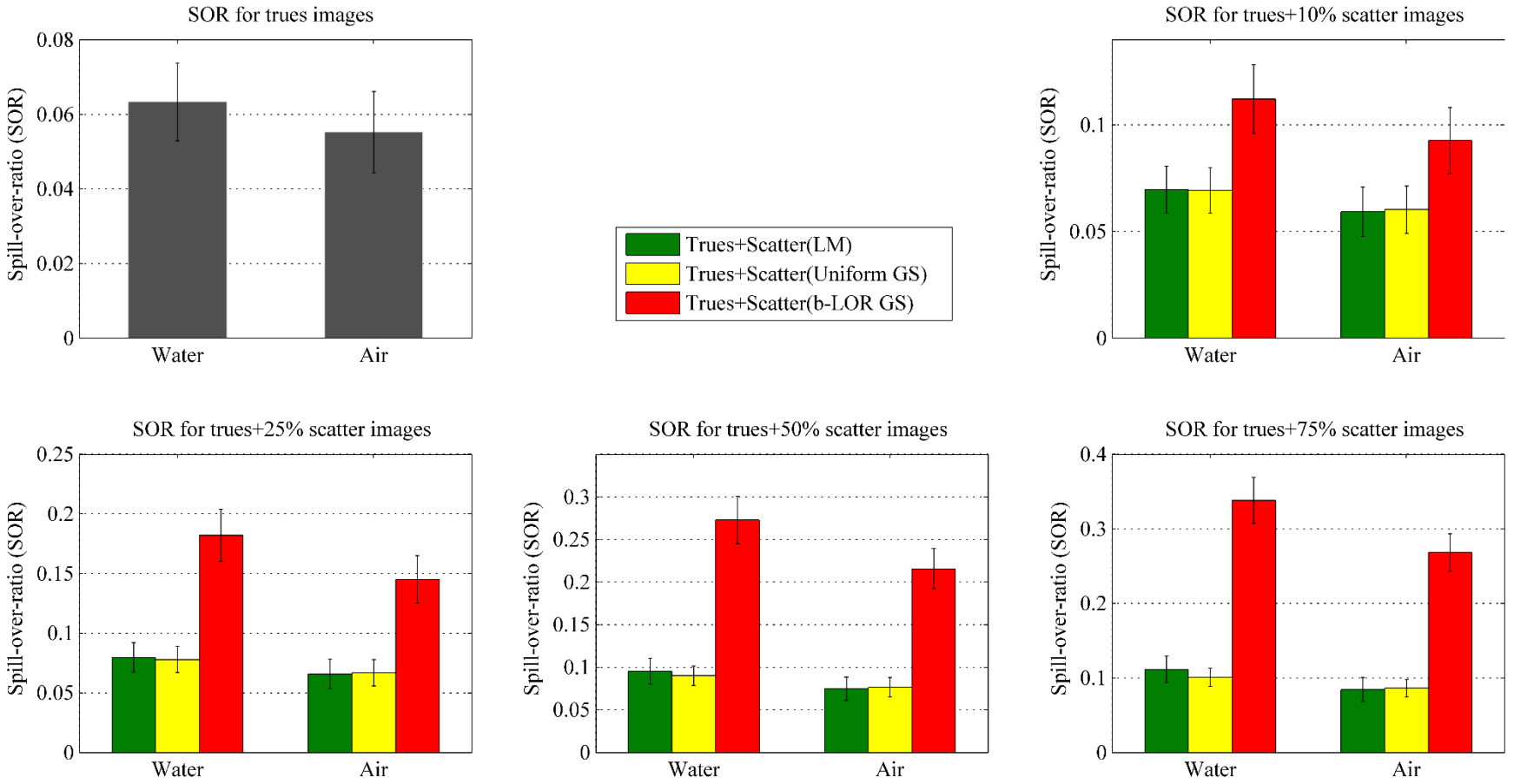

Figure 3-13. Spill-over-ratio (SOR) in different images of the NEMA NU-4 2008 image quality phantom with different scatter fractions in two cylinders filled with air and non-radioactive water. The scatter fraction for each graph is stated at the top of it. The green, yellow, and red bars show SOR in images reconstructed with conventional, uniform, and b-LOR projector/backprojector, respectively. The bar graph with grey bars represents SOR in scatter-free images.

As expected, the SOR in the air-filled cylinder is always lower on average than the water-filled cylinder. More scattering occurs in the water-filled cylinder and the AC helps to recover the contrast of the air-filled cylinder more than the water-filled cylinder. A similar effect was seen in the simple analytical phantom with three hot rods and a cold rod. When compared to images created using a conventional projector/backprojector there is no significant change in SOR when the uniform approach was used, the SOR increases when the b-LOR approach was used. To explain these differences more confidently a two-tailed t-test was done for each image when comparing with conventional LM images. The results of the statistical analysis are shown in Table 3-4.

Table 3-4. *P*-values obtained from the comparison of SOR in reconstructed images of the NEMA NU-4 2008 phantom when comparing to the similar reconstructed images with conventional projection/backprojection method for scattered events. *P*-values greater than 0.1 are shown in blue and less than 0.1 are shown in red background.

	Scatter fraction / Reconstruction technique							
Cylinder	10% / Uniform	10% / b-LOR	25% / Uniform	25% / b-LOR	50% / Uniform	50% / b-LOR	75% / Uniform	75% / b-LOR
Water	0.9502	<0.0001	0.6671	<0.0001	0.2445	<0.0001	0.0381	<0.0001
Air	0.7827	<0.0001	0.7983	<0.0001	0.6682	<0.0001	0.6908	<0.0001

All images reconstructed with the b-LOR approach, have significantly higher residual activity in both water- and air-filled cylinders (*p*-values less than 0.0001). A sample slice reconstructed with true and scattered events with the b-LOR approach, shown in Figure 3-10, explains the graphs, as both cylinders show a high degree of spill-over activity. The increase in SOR when the b-LOR approach was used is directly related to the blurring effect of this method that generates an additive value to all pixels inside the phantom boundary. More residual activity was seen in the water-filled cylinder when the uniform method was applied for the images of unscattered plus 75% scattered events. Although this is the only image with higher SOR than conventionally reconstructed images, there is no evidence of SOR reduction in any other images reconstructed using the uniform method. This implies that neither of the proposed techniques is successful in reducing the residual activity in cold sources, and that the b-LOR approach also degrades the residual activity even for a low ratio of scattered events, such as 10%.

Figure 3-14 shows axial scatter reconstructed middle slices of different parts of the NEMA NU-4 2008 phantom with both proposed techniques and Figure 3-15 shows middle coronal scatter reconstructed slices of the phantom.

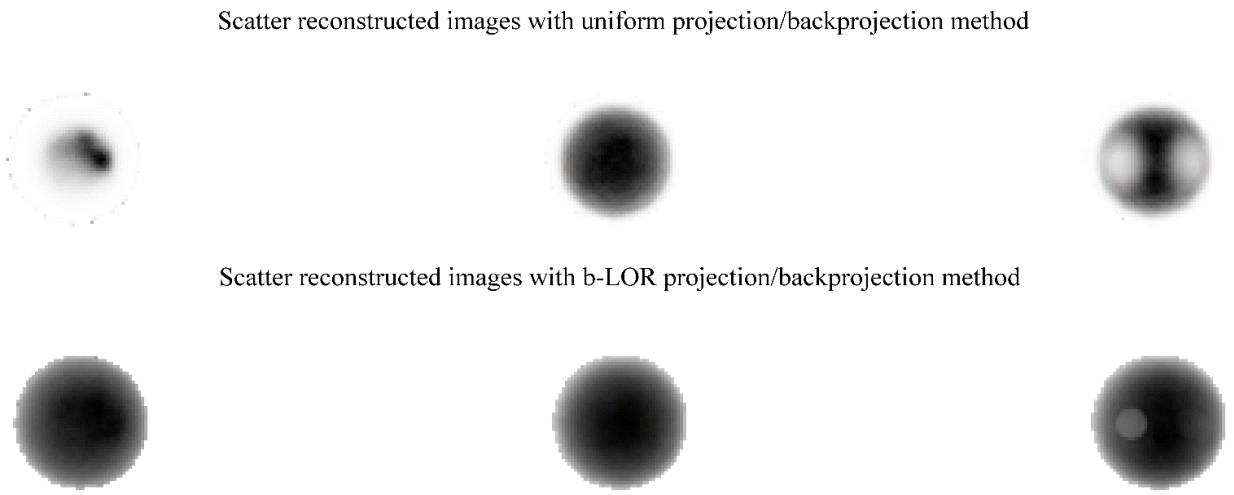

Figure 3-14. Axial scatter reconstructed slices of the NEMA NU-4 2008 image quality phantom. The top row shows images reconstructed with scattered events when the uniform approach was used and the bottom row shows scatter reconstructed images of the phantom when the b-LOR approach was used. The middle slices of the top part, the central part, and the bottom part of the phantom are shown in the left, middle, and the right column, respectively.

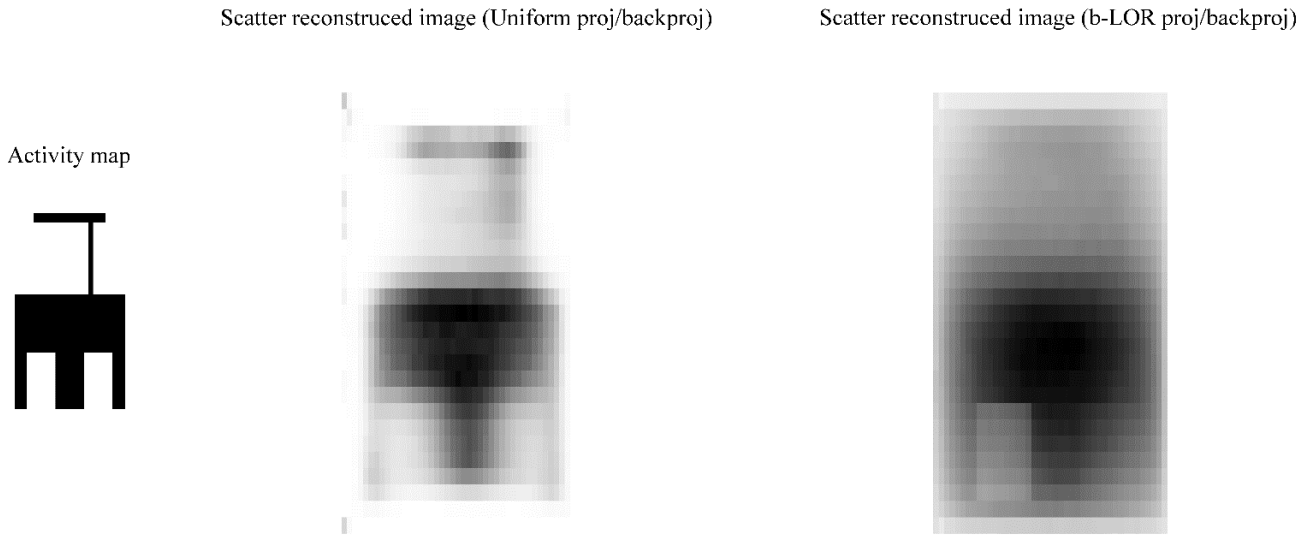

Figure 3-15. Central coronal scatter reconstructed slices of the NEMA NU-4 2008 image quality phantom. The image on the left shows activity map used in GATE simulation, the middle and right hand side images show scatter reconstructed images when the uniform and b-LOR approaches were used, respectively.

Images in these two figures are consistent with the quantitative measurements. All scatter reconstructed images are highly blurred, especially when the b-LOR approach was used, and non-uniformity in the activity distribution can be seen in the middle part of the phantom for both scatter techniques, more so with the uniform projection/backprojection reconstructed images. In the b-LOR scatter reconstructed image, the air-filled cylinder has sharp boundaries as a result of AC, however, this could not prevent high residual activity (high SOR) in the air-filled cold cylinder in the images.

3.4 NEMA NU-2 2007 Image Quality Phantom

Reconstructed images, image quality factors, and results obtained with the NEMA NU-2 2007 image quality phantom are discussed in this section. As mentioned previously, this phantom has four hot spheres and two large water-filled cold spheres with diameters varying between 10 to 37 mm. The ratio of hot-to-background activity was four and an air-filled cylinder at the middle of the phantom was used to evaluate residual activity. Images of the NEMA NU-2 phantom were reconstructed into a 100×100×36 matrix with voxel size of 0.44×0.44×0.72 cm. The MC simulation process (image acquisition) was done only once with a high-resolution voxelized phantom, since both simulation and the image reconstruction steps were very time consuming. The single simulation done for this trial took roughly 8 days and the reconstruction time varied between 75 to 83 hours, depending on the total number of events and whether AC was applied or not. The quantitative analyses to follow do not include any statistical uncertainties, as uncertainty calculations according to NEMA guidelines for the NU-2 phantom would have required multiple image acquisition simulations, which were judged to be too time-consuming (78). The scatter fraction in this phantom was seen to be around 40% (based on the performed GATE simulation), so 9,321,290 unscattered events and 3,740,516 single-scatter events were used in image reconstructions. Scatter reconstructed images were not included in quantitative analysis and reconstructed for demonstration purposes only. Images with scattered events only were reconstructed using 60 subsets, whereas 40 subsets were used to reconstruct all other images (because of slower convergence rate in scatter reconstruction). In addition, images were reconstructed with and without AC to investigate the effect of AC in a large size phantom.

Figure 3-16 shows sample reconstructed axial images of the NEMA NU-2 phantom with various reconstruction techniques with and without AC.

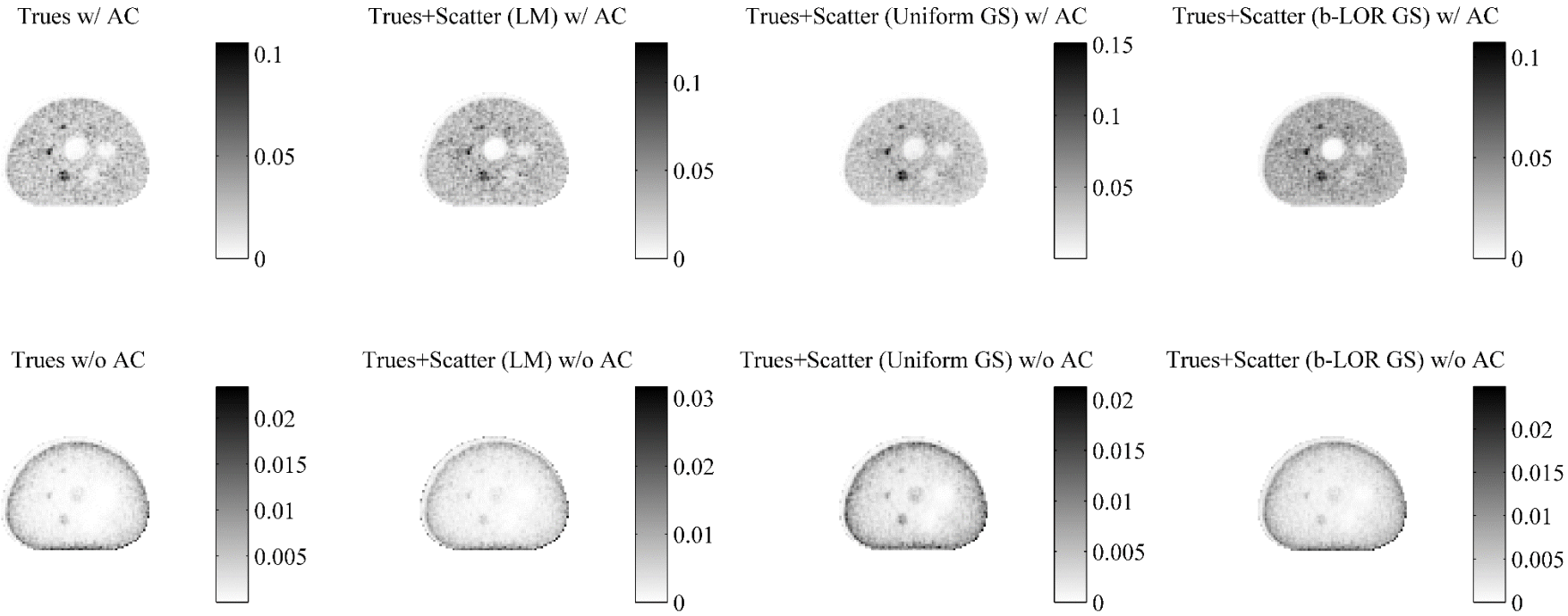

Figure 3-16. Sample reconstructed axial slices of the NEMA NU-2 2007 image quality phantom. From left to right, reconstructed images with unscattered events only, unscattered and scattered events when conventional projection/backprojection technique was used, unscattered and scattered events when the uniform projection/backprojection technique was used, and unscattered and scattered events when the b-LOR projection/backprojection technique was used are shown. The top row shows images with compensation for attenuation effect and the bottom row shows images without attenuation correction.

Images without AC showed poor spatial resolution and low contrast of the hot and cold spheres. Backprojection of scattered events over areas could not recover the contrast, although the image reconstructed with the uniform approach and without AC show somehow better contrast in comparison with other uncorrected images. However, the quality of the attenuation corrected images are still clearly superior to all uncorrected images. Therefore, reconstructed images without AC were excluded from quantitative analysis and are only shown in this figure as samples.

Figure 3-17 illustrates the calculated contrast recovery coefficient (CRC) for four hot spheres in reconstructed scatter-free images.

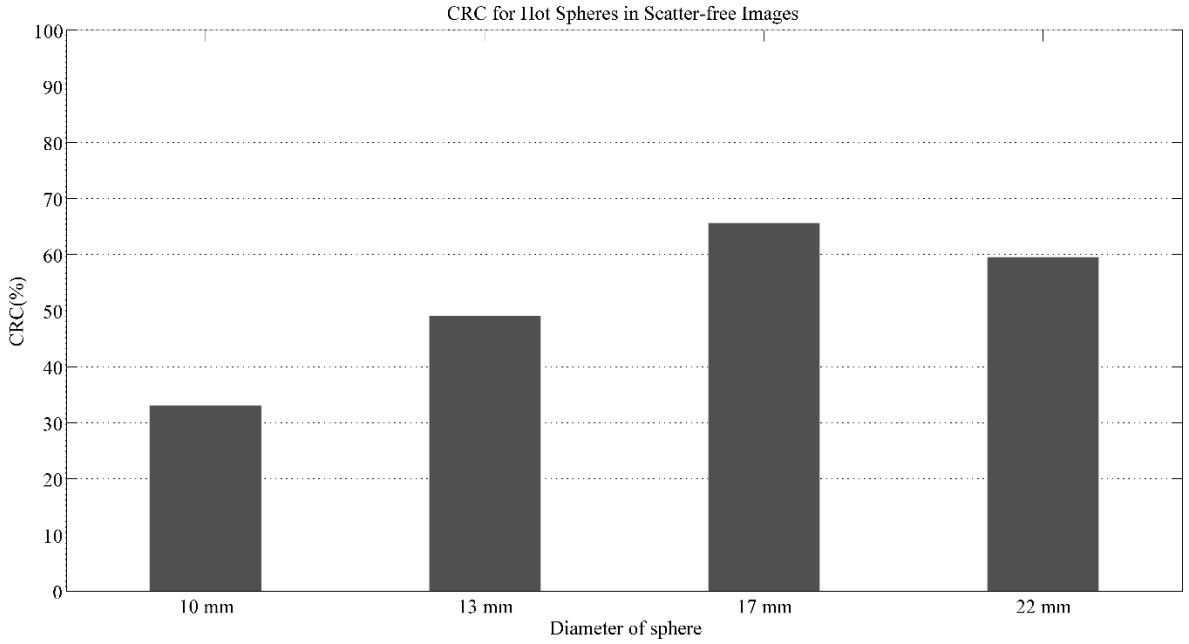

Figure 3-17. Contrast recovery coefficient for hot spheres in reconstructed scatter-free images of the NEMA NU-2 2007 image quality phantom.

As this figure shows, CRC for 10, 13, 17, and 22 mm diameter spheres are equal to 33.2%, 49.1%, 65.6%, and 59.5%, respectively. These values are not to be compared with CRC in other images reconstructed using both unscattered and scattered events, as they had a different convergence level.

Figure 3-18 illustrates calculated CRC for four hot spheres in reconstructed images using all recorded events with various reconstruction techniques. The notation used in the following graphs is the same as that in NEMA NU-4 section.

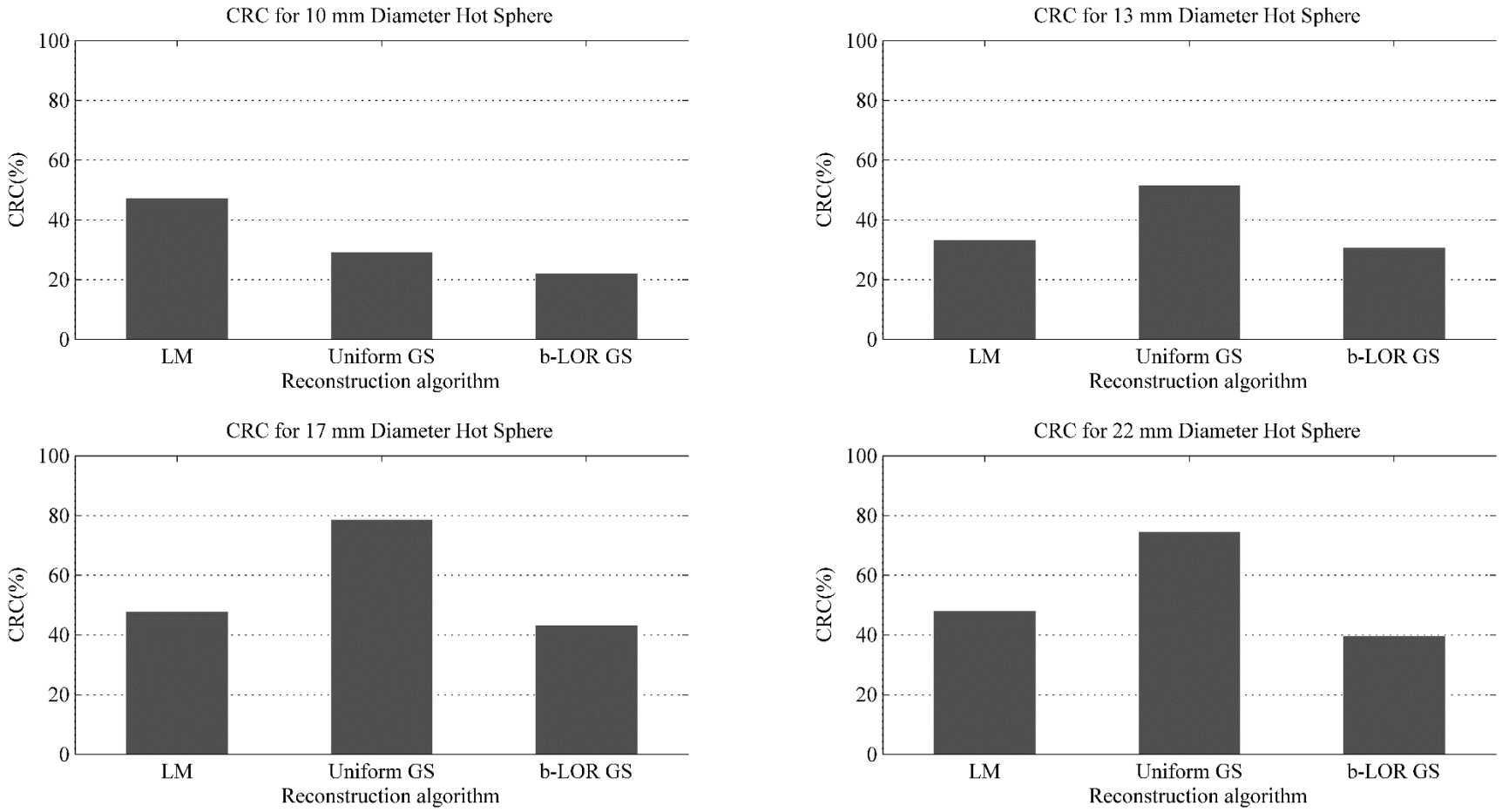

Figure 3-18. Contrast recovery coefficient (CRC) for hot spheres in reconstructed images of the NEMA NU-2 2007 image quality phantom. The diameter of each hot sphere is stated at the top of each graph and the reconstruction technique for each bar is mentioned below each bar.

For 13, 17, and 22 mm diameter spheres, the uniform approach has increased the CRC by 55.3%, 64.6%, and 55.1%, respectively, when compared with conventionally reconstructed images, labeled as "LM" (percentage differences are reported as relative changes to conventionally reconstructed images and not absolute changes in CRC). However, for the smallest hot sphere, the uniform approach has decreased CRC by 38%, which is most likely the effect of noise or due to blurring out the activity because of backprojection over areas. The b-LOR approach, on the other hand, has degraded CRC by 52.8%, 7.2%, 9.4%, and 17.1% for 10, 13, 17, and 22 mm diameter hot spheres, respectively. The decrease in CRC when the b-LOR approach was used could be explained by the blurring effect of this method. The b-LOR reconstructed image shown in Figure 3-16 is also consistent with this measurement.

Figure 3-19 and Figure 3-20 show calculated CRC for 28 and 37 mm diameter spheres filled with non-radioactive water (cold spheres) in scatter-free images and the images reconstructed with all recorded coincidences and various reconstruction techniques, respectively.

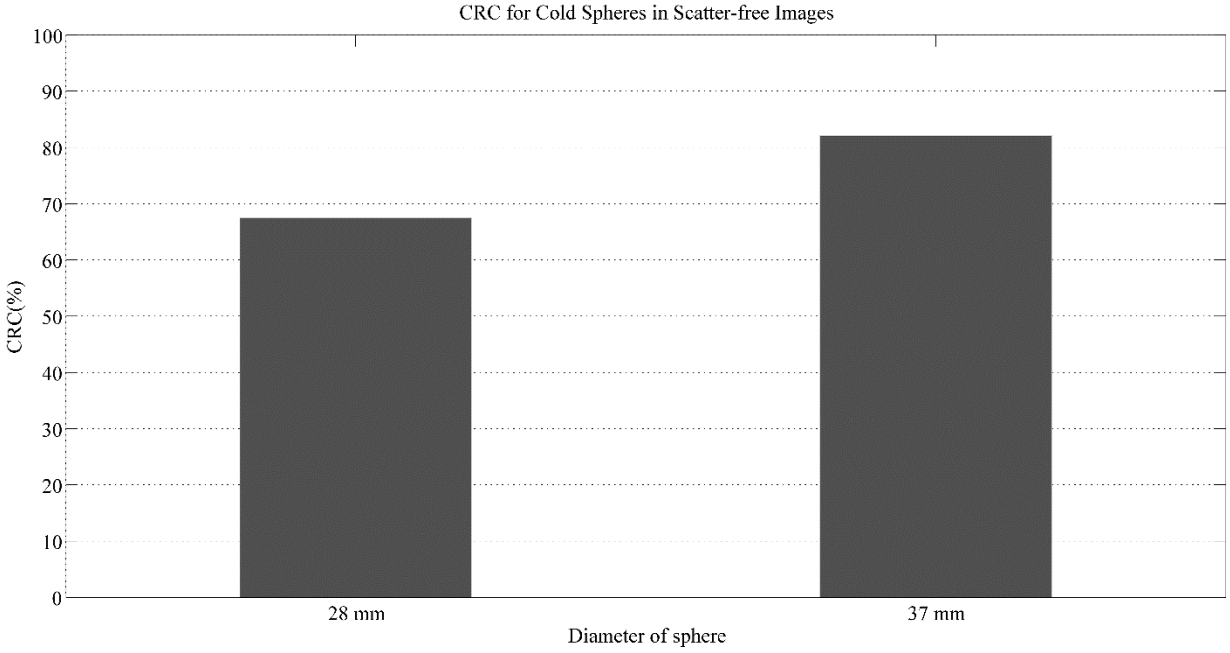

Figure 3-19. Contrast recovery coefficient (CRC) for cold spheres in reconstructed scatter-free images of the NEMA NU-2 2007 image quality phantom.

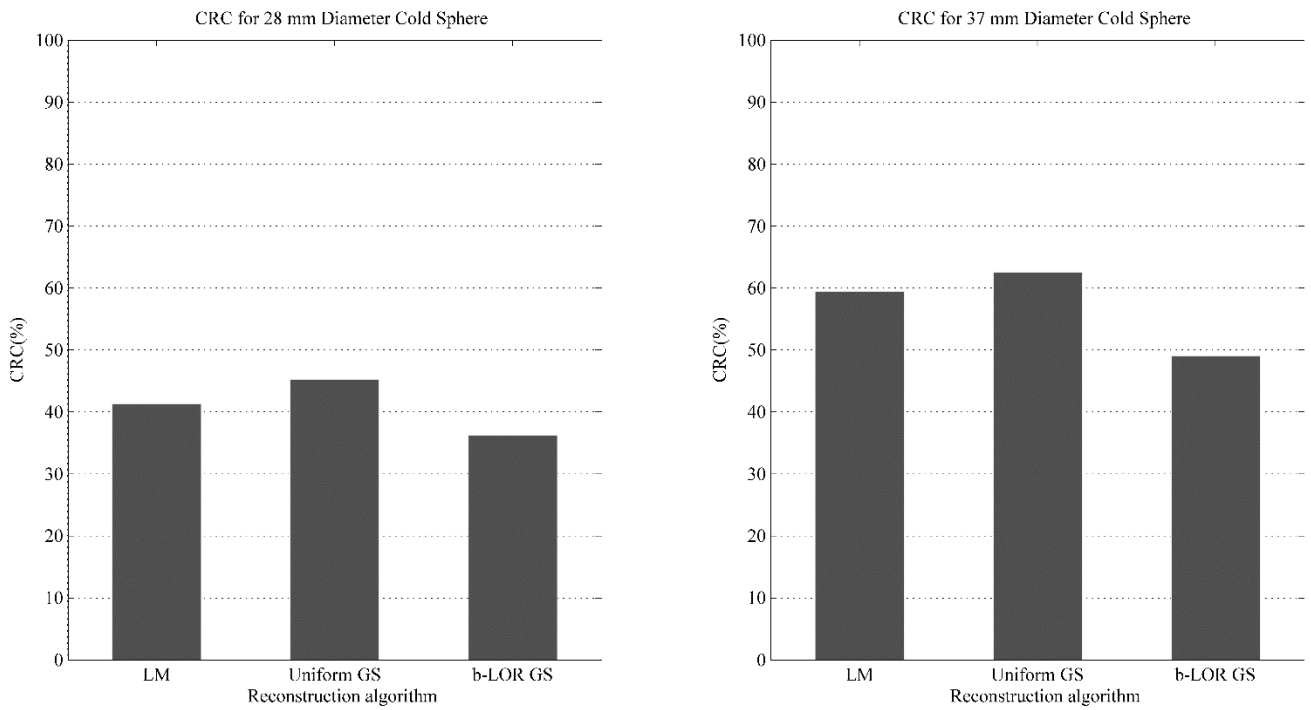

Figure 3-20. Contrast recovery coefficient (CRC) for cold spheres in reconstructed images of the NEMA NU-2 2007 image quality phantom. The diameter of each cold sphere is stated at the top of each graph and the reconstruction technique for each bar is mentioned below it.

The CRC for cold spheres in scatter-free images of the NEMA NU-2 phantom was calculated to be 67.4% and 82.1% for 28 and 37 mm diameter cold spheres, respectively.

Using the proposed uniform projection/backprojection method for scattered events has increased CRC by 9.7% and 5% for 28 and 37 mm diameter cold spheres, respectively. The b-LOR approach, however, has decreased CRC by 12.4% and 17.5% for 28 and 37 mm diameter cold spheres, respectively. The variation in CRC for cold areas is consistent with that for hot areas, however, the increase in CRC for cold spheres when the uniform approach was used is less than the improvement for hot spheres (compare 55.3%, 64.6%, and 55.1% with 9.7% and 5%), which was of course anticipated due to backprojection over areas.

Figure 3-21 shows the results of background variability within defined 60 ROIs with various diameters in the background of reconstructed scatter-free image.

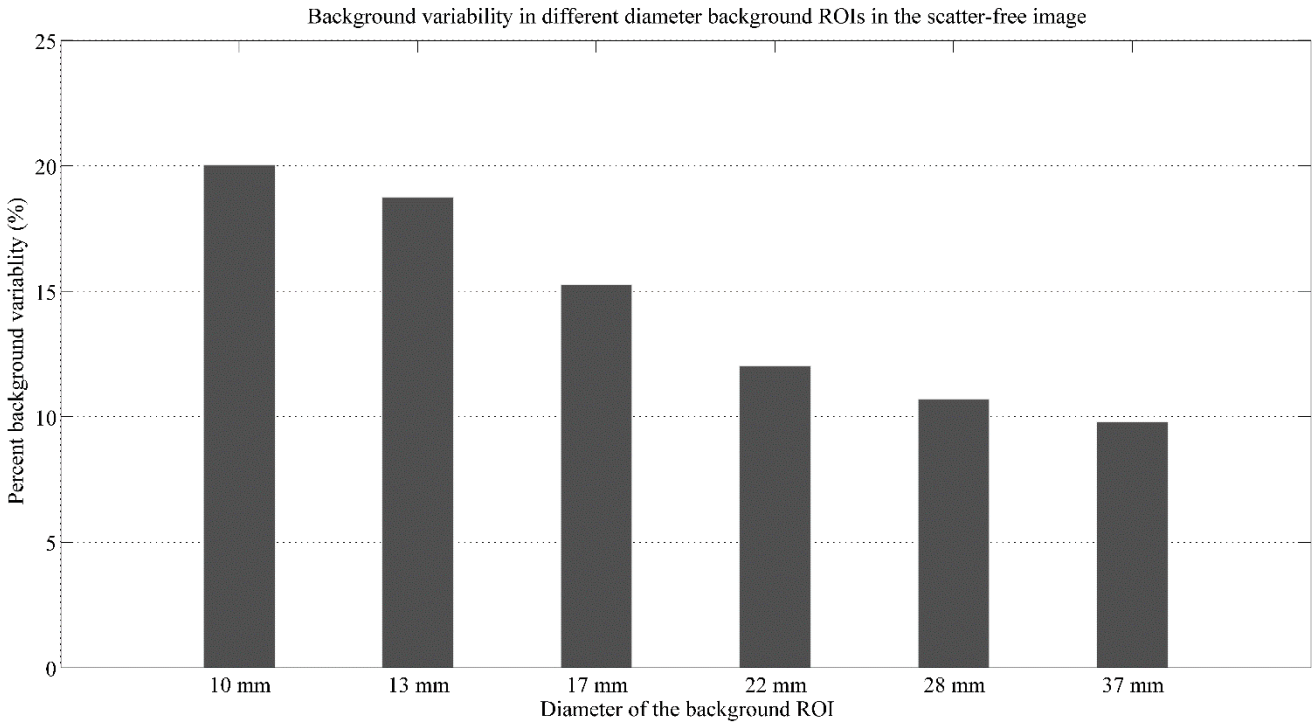

Figure 3-21. Percentage background variability in reconstructed scatter-free images of the NEMA NU-2 image quality phantom. Each bar represents background variability in 60 ROIs with diameters indicated below the bar.

Background variability varies between 20% to 9.8% and decreases as the radius of the ROI increases. This is becasue that random variations in pixel counts (as a result of Poisson decay nature of radioactivity) has a lower impact on larger ROIs, as more pixels are involved in the averaging process, and hence there is a decrease in the standard deviation of pixel counts in ROIs.

Figure 3-22 illustrates calculated background variability for the images reconstructed with all recorded events (unscattered and scattered) and different reconstruction techniques.

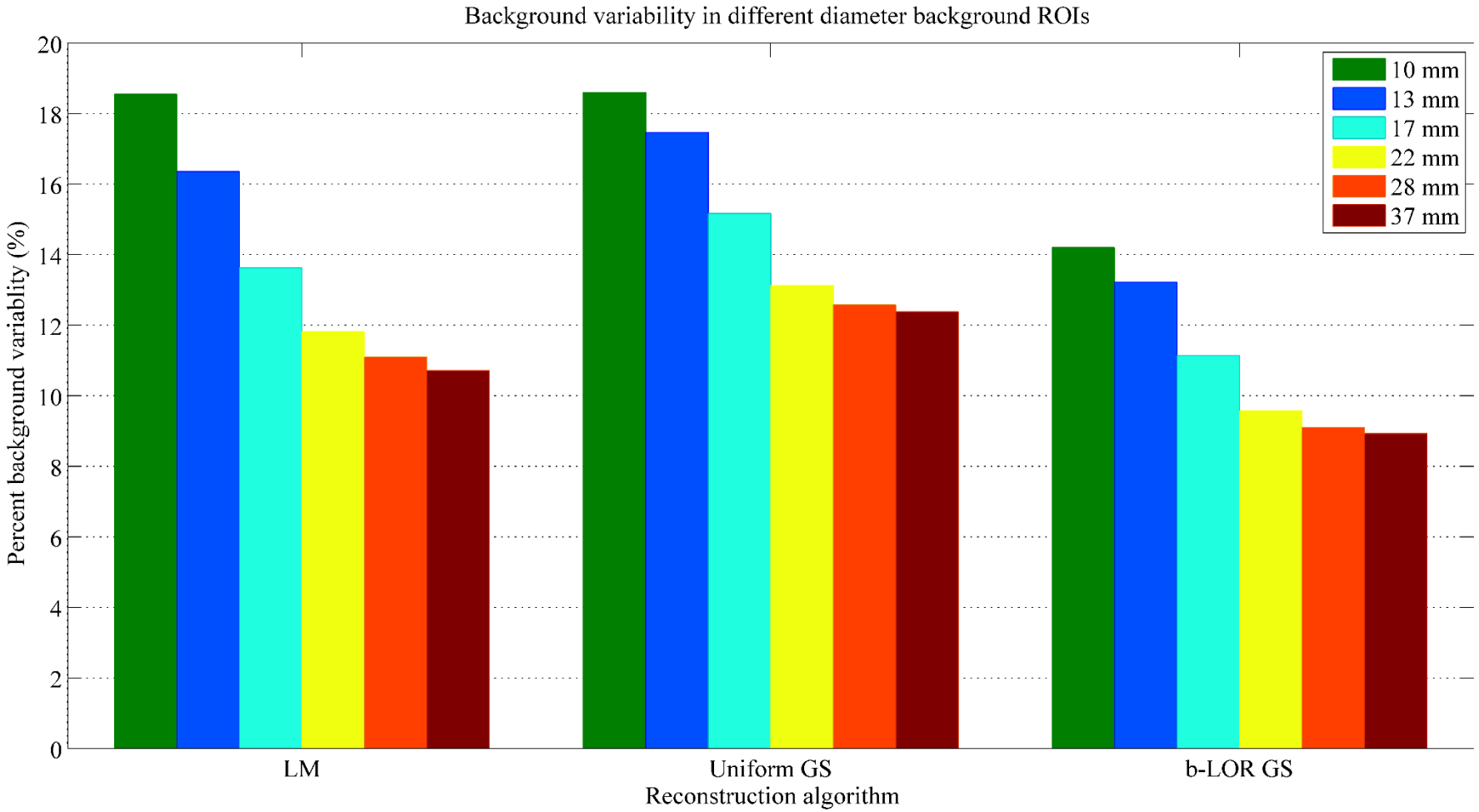

Figure 3-22. . Percentage background variability in reconstructed images of the NEMA NU-2 image quality phantom with different reconstruction techniques. Each set of bars represents a certain reconstruction technique, stated below each set, and each color corresponds to the ROI with a certain diameter, stated in the legend of the graph.

Consistent with Figure 3-21, increasing the diameter of ROIs has led to a decrease in background variability, due to the reduction in standard deviation of pixel counts in ROIs. For 10, 13, 17, 22, 28, and 37 mm diameter ROIs, the background variability has increased by 0.5%, 6.7%, 10.5%, 11%, 13.5%, and 15.9% and decreased by 23.2%, 19.5%, 18.4%, 18.9%, 18%, and 16.5% when the uniform and b-LOR approaches were used, respectively.

The changes observed with the uniform approach are not consistent with the trend previously seen in the NEMA NU-4 background variability analysis. The reason for this inconsistency can be found by investigating the methods used for background variability measurements. In the NEMA NU-4 analysis, a cylindrical volume of interest (VOI) was defined at the central part of the phantom. In the NEMA NU-4 analysis the background variability was defined related to the standard deviation of pixel counts in that VOI, whereas, in the NEMA NU-2 analysis 60 ROIs were drawn (on five axial slices) close to the surface of the phantom, and not in the middle part. Considering the fact that the inhomogeneity seen in the images reconstructed with the uniform approach, has a greater impact near the outer part of the phantom than in the center, one can expect more variation in pixel values in the area close to the periphery of the phantom. This also explains why the relative difference between background variability becomes larger (conventionally reconstructed images versus the uniform approach) as the diameter of background ROIs increases. Indeed, larger ROIs close to the surface of the phantom cover more pixels affected by the non-uniformity property of the uniform approach and leads to higher degradation of background variability. In order to clarify this issue, Figure 3-23 shows the position of ROIs in one single slice and a sample scatter reconstructed image for each of the proposed scatter reconstruction techniques.

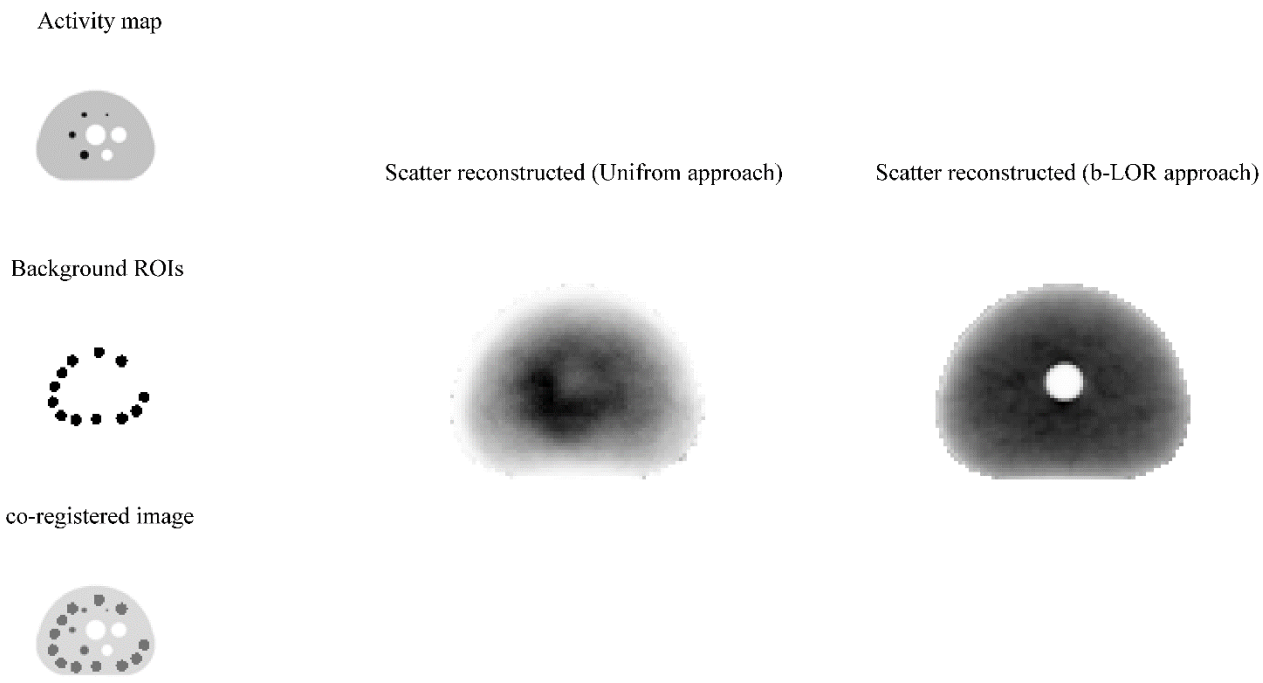

Figure 3-23. Background ROIs and scatter reconstructed images of the NEMA NU-2 2007 image quality phantom. The right column shows predefined activity map, 12 background ROIs with diameter of 28 mm in one slice, and their corresponding co-registered image from top to bottom. Other two images are scatter reconstructed images using uniform and b-LOR projector/backprojector from left to right. Note that the slices shown are the ones passing through middle of spheres (reconstructed images of the shown activity map in this figure).

This inhomogeneity, increasing background variability, is obvious in the scatter reconstructed images using the uniform approach. The same non-uniformity in activity distribution can also be seen in other slices, even far from the hot and cold spheres. As mentioned earlier, the 60 background ROIs were drawn on five different slices (12 ROIs per slice) and are all affected by this inhomogeneity.

All slices of the activity maps and scatter reconstructed images for the NEMA NU-2 phantom are shown in Figure 3-24, Figure 3-25, and Figure 3-26 corresponds to activity map, uniform, and b-LOR approaches, respectively.

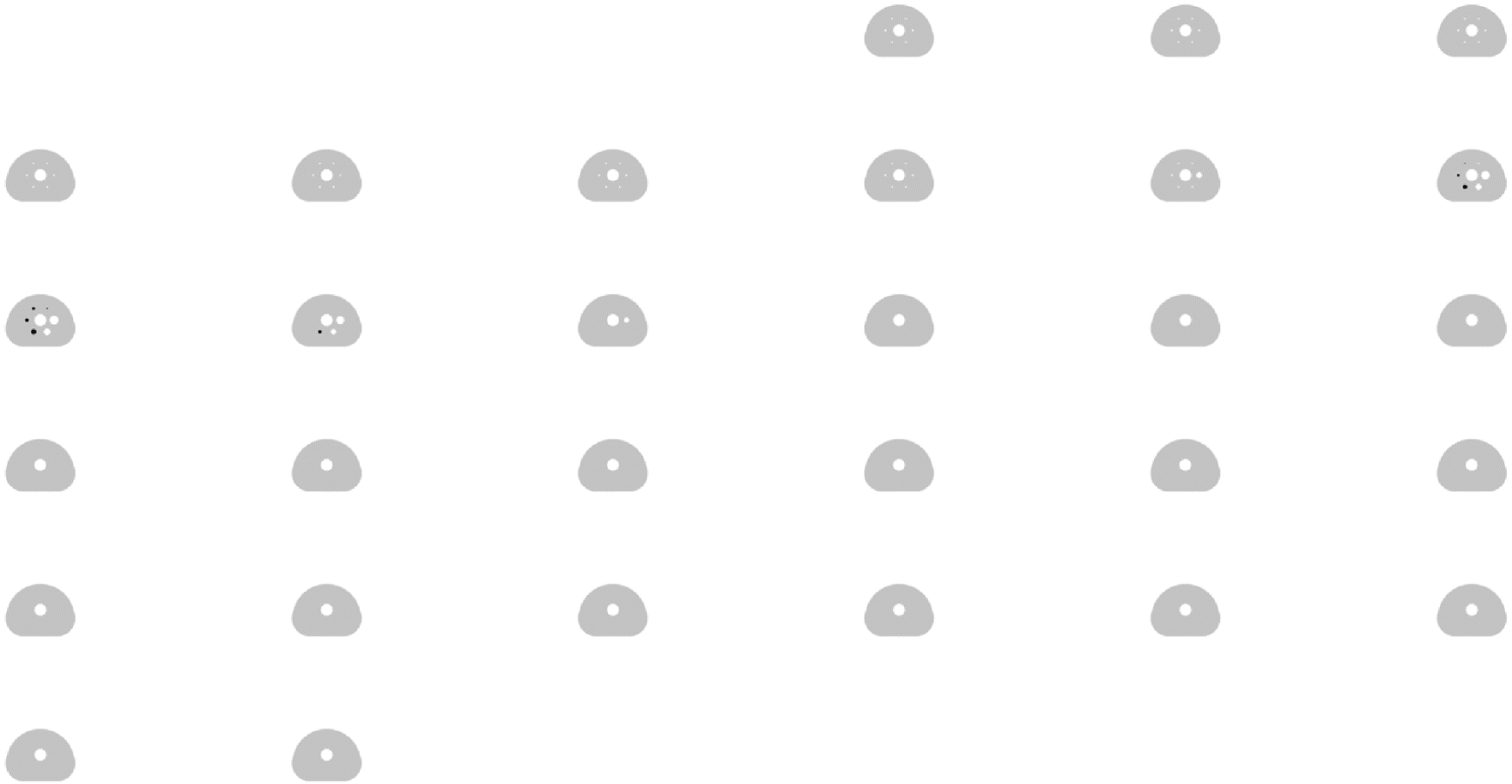

Figure 3-24. All slices of the predefined activity map of the NEMA NU-2 2007 image quality phantom.

Figure 3-25. All scatter reconstructed slices of the NEMA NU-2 2007 image quality phantom using the uniform projection/backprojection method.

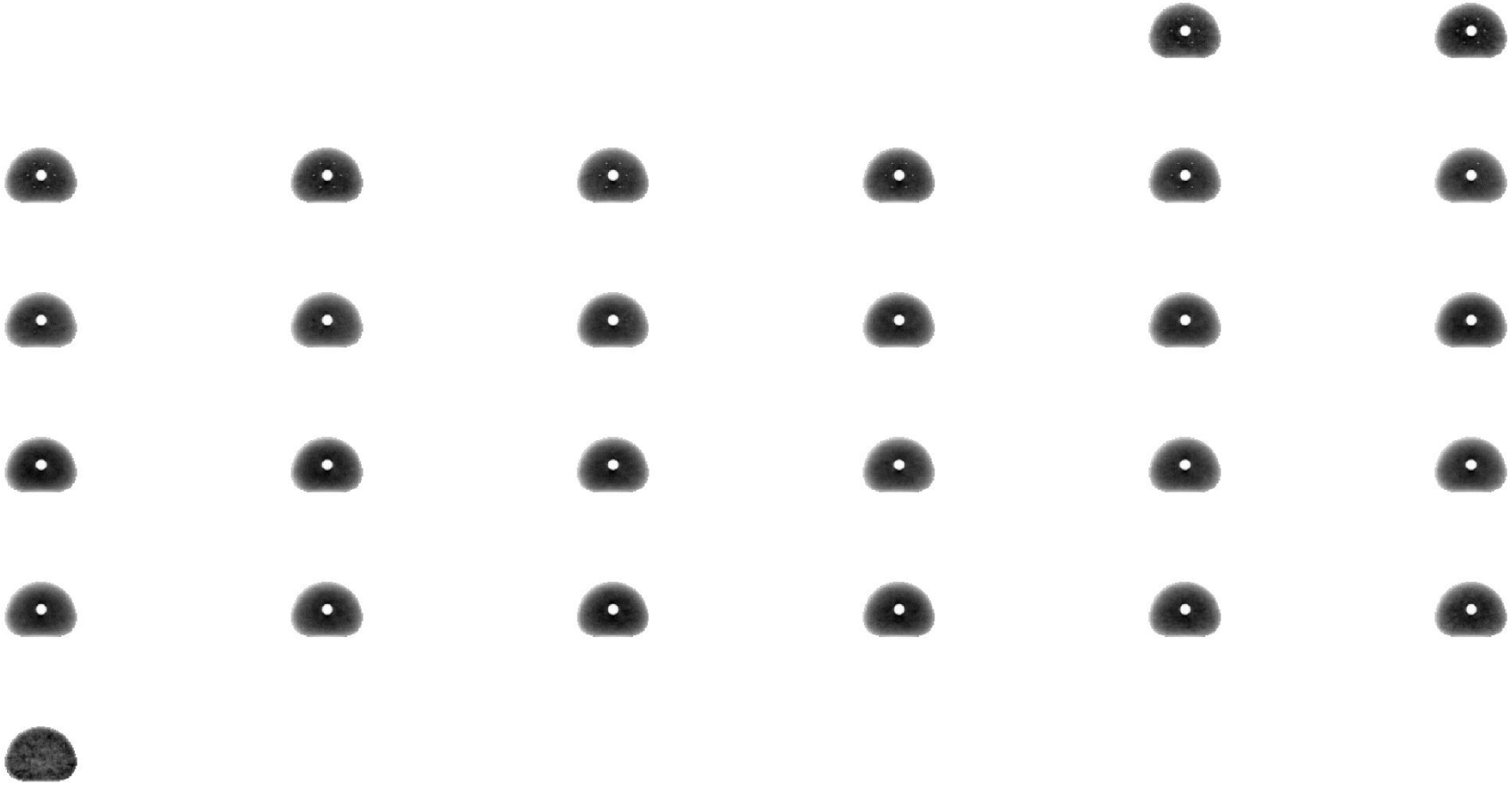

Figure 3-26. All scatter reconstructed slices of the NEMA NU-2 2007 image quality phantom using the b-LOR projection/backprojection method.

While all scatter reconstructed images with the uniform approach demonstrate activity inhomogeneity in the uniform part of the phantom, scatter reconstructed images with the b-LOR method show relatively uniform images and very poor contrast for hot and cold spheres.

The last image quality factor measured for images of the NEMA NU-2 phantom was residual activity percentage (same as SOR) in the lung insert. Mean residual error over all reconstructed slices of scatter-free images was calculated to be 7.9% for the lung insert. Figure 3-27 represents the results for residual error in different reconstructed images of the phantom.

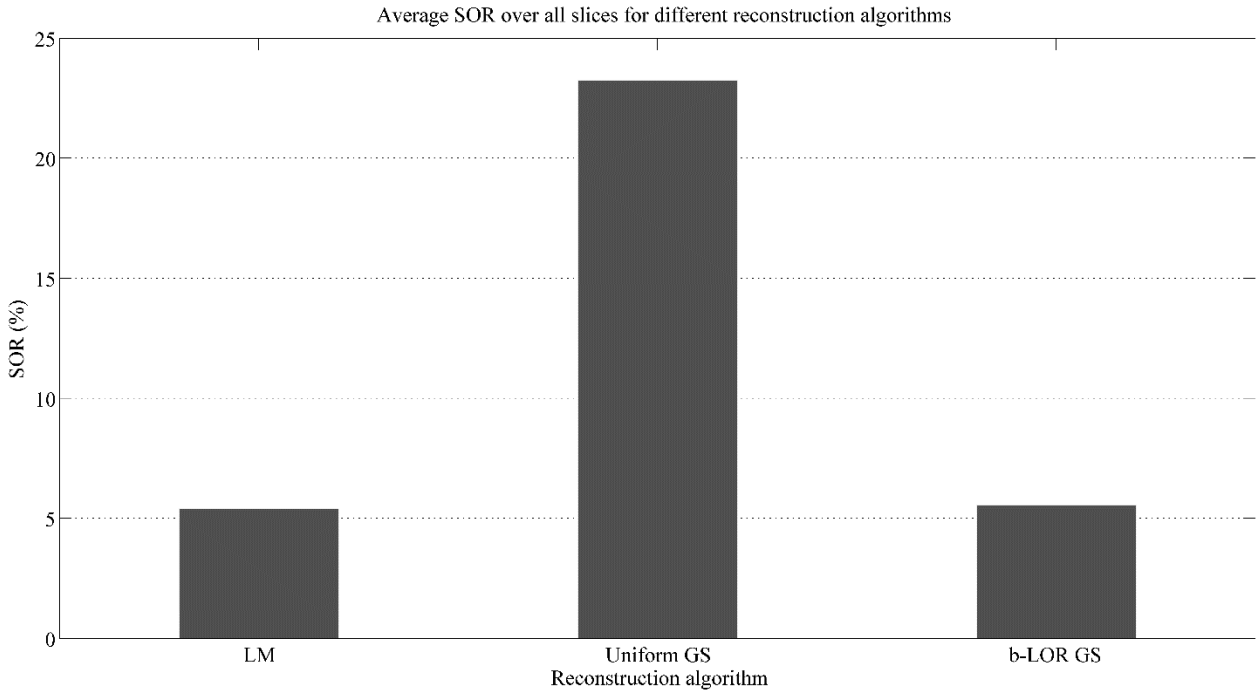

Figure 3-27. Average residual error or SOR over all slices of the NEMA NU-2 image quality phantom images for various reconstruction techniques.

As this figure shows, reconstruction with the uniform projection/backprojection method has led to a severe degradation of residual error by changing the SOR percentage from 5.4% to 23.2%. In other words, the residual error in images reconstructed with the uniform approach is 4.3 times greater than that in conventionally reconstructed images. Images reconstructed with the b-LOR approach, however, did not change the residual error significantly (SOR = 5.6%) when compared with conventionally reconstructed images. Images shown in Figure 3-25 clearly demonstrate poor contrast in the area of the lung insert that is due to backprojection over areas. However, relatively better contrast for the lung insert in b-LOR reconstructed images (Figure 3-26) was seen

which is due to the effect of AC. This is a similar pattern as seen previously in the simple analytical phantom with three hot rods and one cold rod, however, to further clarify this issue, a set of images were reconstructed using scattered coincidences with the b-LOR projection/backprojection technique and without AC. An axial slice of the phantom passing through the spheres is shown in Figure 3-28 when AC was not used and compared with the similar image when AC was used.

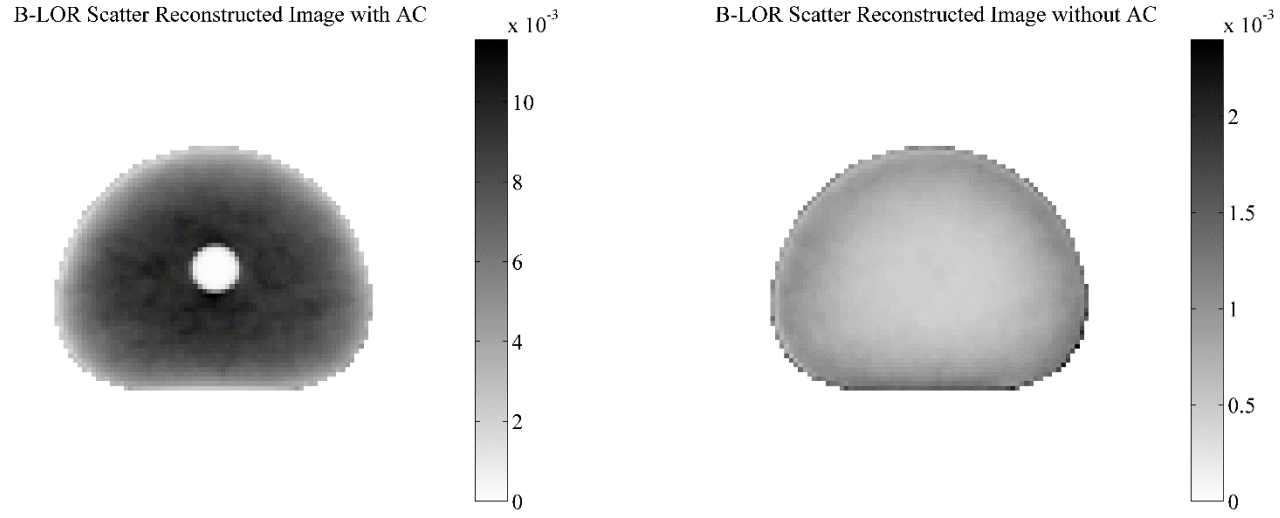

Figure 3-28. Scatter reconstructed images of the NEMA NU-2 2007 image quality phantom with the b-LOR approach with and without compensation for attenuation. The slices shown here are the ones passing through the center of hot and cold spheres.

As images in this figure show, there is no contrast for the lung insert in the uncorrected scatter reconstructed image with the b-LOR approach.

3.5 Further Exploration of the Proposed Techniques

Images of small and large uniform cylindrical phantoms were reconstructed using scatter coincidences with the uniform projection/backprojection approach in different scattering angle windows to investigate the change in previously detected inhomogeneity when scattering angle varies. This exploration was based on the assumption that the proposed scatter reconstruction techniques should approach regular OPL-EM technique when scattering angle approaches zero. A technical challenge here was the very low number of low-angle (below 10°) single-scatter events, so the first scattering angle window was chosen as scattering angles between 0.1° to 20° (corresponding to a minimum scattered photon energy of 482 keV). The other two scattering angle

windows were chosen as 15° to 35° (corresponding to an energy window of 432.7 to 494.1 keV) and 35° to 57.3° (energy window of 350 to 432.7 keV). One million single-scatter events were chosen in each scattering angle window for the small uniform cylindrical phantom and images of each window were reconstructed into a 128×128×9 matrix with 40 subsets when the uniform projector/backprojector operator was implemented into OPL-EM technique.

Figure 3-29 shows the central images of this phantom for the mentioned energy windows with their corresponding normalized horizontal profiles.

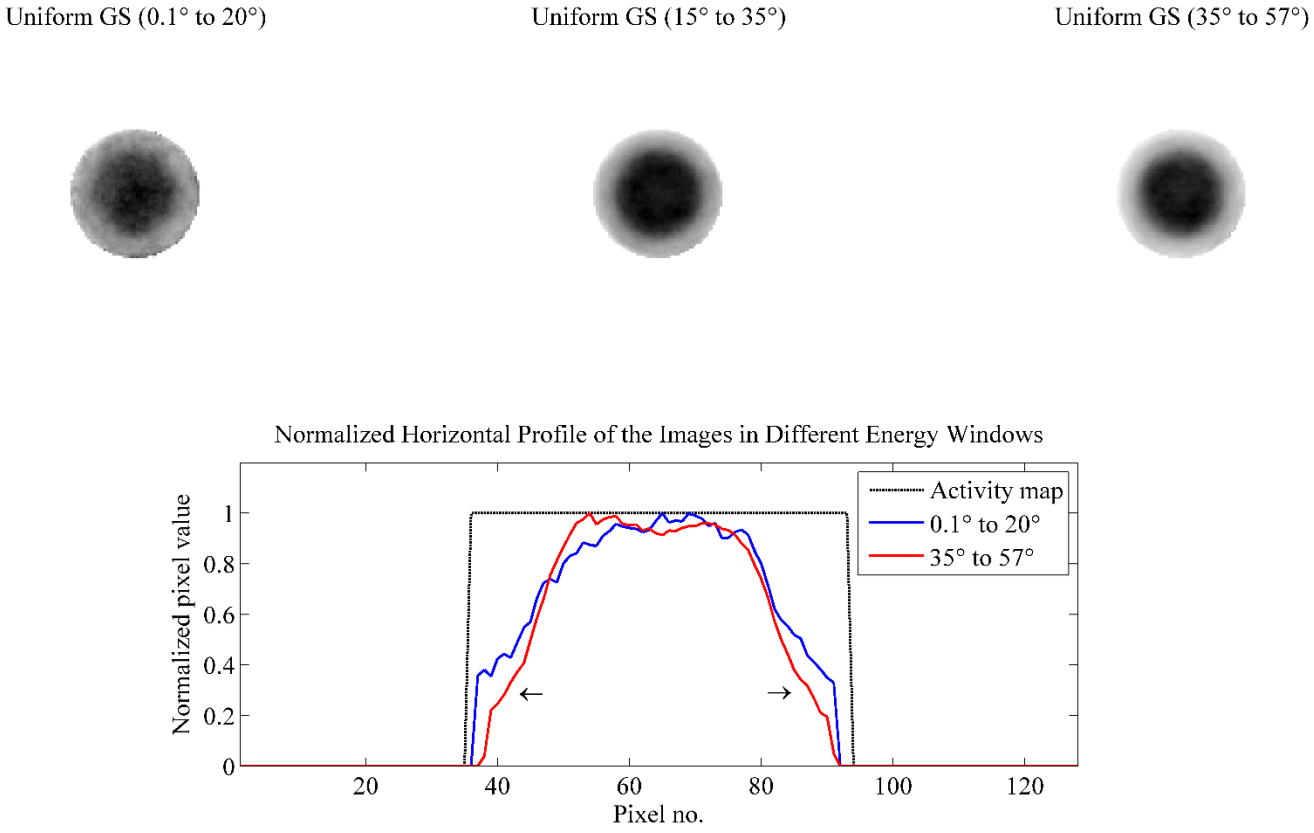

Figure 3-29. Central slice of the small uniform cylindrical phantom reconstructed with scattered photons with various windows of scattering angle using the uniform projection/backprojection method and their normalized profiles. The profile of the second image (reconstructed with scattered photons of 15° to 35° scattering angle) is not shown in the graph to show the difference between other profiles more clearly. In addition, the black dotted line shows the profile of the predefined activity map.

The difference between the central and peripheral area of the images becomes more obvious as the scattering angle increases, which is also shown in the profiles of the images in the area of the two arrows. The profile of the scatter reconstructed image with low scattering angle (blue line) is still non-uniform and far from the true activity map (black line). That is because there is still no-

ticeable difference between backprojection along a line (as in conventional backprojection) and backprojection over an area, even for scattering angles around 20°. For instance, for a single-scatter event with a scattering angle of 20° for the same phantom and PET system, backprojection should be done over an area with a maximum distance of 15 mm from the line connecting two detection points (this is actually the maximum possible length of *Cs* line in Figure A- 2 and is calculated based on equation (1.2) of Appendix A). Additionally, the profile of the image reconstructed with the scatters from 0° to 20° shows more fluctuations in comparison with the other profile that reflects a noisier image. This is also consistent with the assumption that approaching conventional list-mode reconstruction should result in a noisier image than scatter reconstructed image with higher scattering angles.

Scatter reconstructions of the line source in a water-filled cylindrical phantom (explained in Section 2.3.2.2) using different scattering angle windows were also performed to evaluate the assumption that the b-LOR technique should also approach conventional list-mode reconstruction as the scattering angle approaches zero. Through an MC simulation, a total of 578,950 single-scatter events in the window of 0° to 20° were generated. One million single-scatter events were generated in each scattering window of 15° to 35° and 35° to 57°. Images were reconstructed for each scattering angle window separately, and their horizontal profiles were plotted and are shown in Figure 3-30. Since the number of events in the first window was different from that in other windows, images of the first window were reconstructed with 24 subsets. This keeps the number of coincidences in each subset almost the same in the different reconstructions, although, the final images are likely to have different convergence levels. This issue was ignored in this specific comparison since there was no strong requirement for quantitative accuracy.

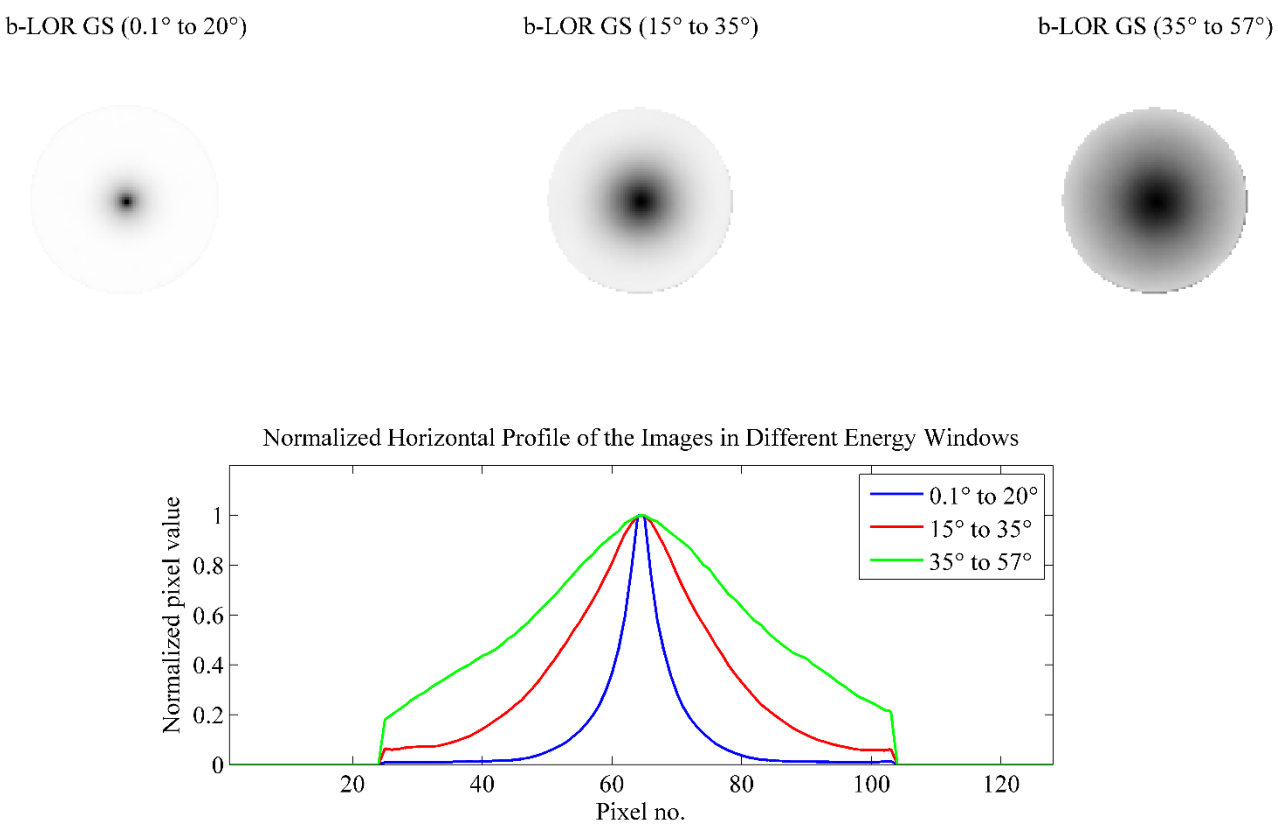

Figure 3-30. Central slice of the line source in cylindrical phantom reconstructed with scattered photons with various windows of scattering angle using the b-LOR projection/backprojection method and their normalized profiles.

Images and profiles shown in this figure clearly show LSF broadening as scattering angle increases and confirms the assumption of approaching conventional list-mode reconstruction as scattering angle decreases.

Furthermore, the blurring is consistent with the images and results mentioned in (2), knowing that the non-TOF reconstruction of scattered events can be assumed as equivalent to TOF reconstruction of scattered events when timing resolution is very poor. Figure 3-31 shows scatter reconstructed images of a cylindrical phantom (30 cm diameter) with six spherical sources of variable diameters (10, 13, 17, 22, 28, 37 mm) in the central plane using TOF information and b-LOR approach (taken from the original paper).

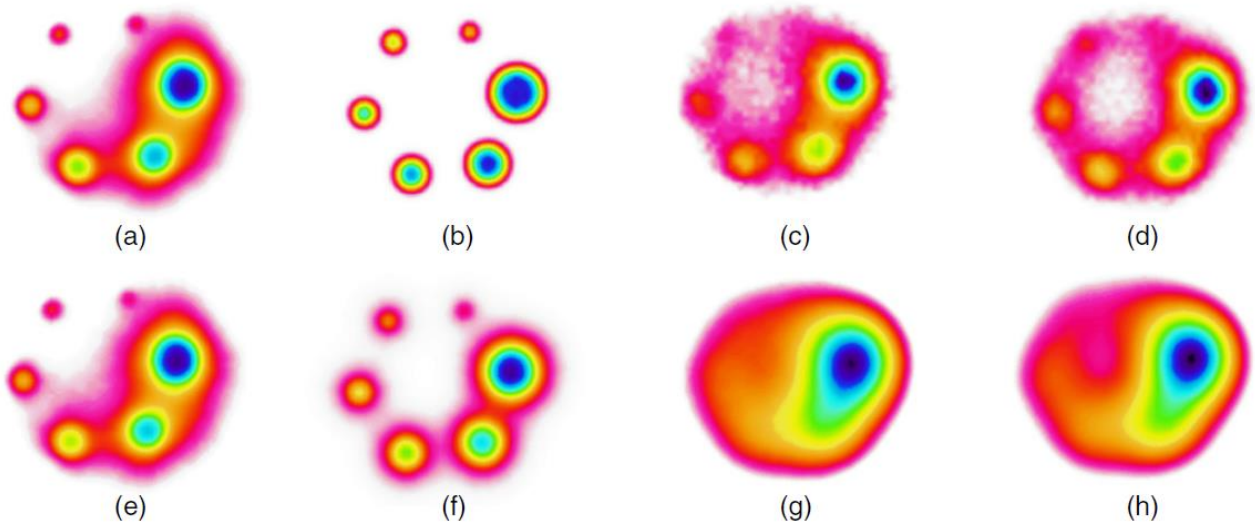

Figure 3-31. Reconstructed images of a 30 cm cylinder with six hot spheres using TOF information and b-LOR approach. An ideal TOF PET system (1 ps time resolution and 0.1% energy resolution) was simulated in production of the images in the top row and a future generation TOF PET (200 ps time resolution and 5% energy resolution) was used for images of the bottom row. (a) and (e) are non-TOF reconstruction of unscattered coincidences, (b) and (f) are TOF reconstruction of unscattered coincidences, (c) and (g) are TOF reconstruction of scattered events with 100 keV energy threshold, and (d) and (h) are TOF reconstruction of scattered events with 435 keV energy threshold. Reprinted by permission of the Institute of Physics (IOP) from (2), Figure 5.

Significant blurring can be seen in TOF scatter reconstruction of scattered coincidences when timing resolution is 200 ps (see (g) and (h) images). Current TOF PET systems have longer timing resolution than 200 ps, and 200 ps is indeed considered as a very good timing resolution for a clinical TOF PET system.

4 Conclusions and Recommendations

In this work, extension of two previously discovered scatter reconstruction algorithms to 3D non-time-of-flight (non-TOF) PET was carried out under ideal circumstances. The first technique was previously developed by our group and published in (1, 69, 70) for 2D non-TOF PET systems. In these papers, a method was explained in which a possible annihilation area for each single-scatter event is defined based on spatial information of photon detection and their corresponding recorded energy. The method was implemented with the assumption that all voxels inside the scattering surface have the same probability for the annihilation event. In order to increase efficiency of this algorithm, the patient outline was also used to further confine the possible annihilation area. In addition, for each scattered event an attenuation correction coefficient was calculated by averaging over all broken-line-of-responses' (b-LORs') attenuation correction coefficients for the scattered event. Extension of this method to 3D non-TOF PET was referred to as "uniform approach" due to uniform backprojection over a possible annihilation area for each scattered event.

The idea of using b-LORs separately and independently was first developed in (2) for ideal and future generation 3D TOF PET systems. In that paper, the authors presented a new method for reconstruction of scattered events in 3D PET using the spatial and temporal information of detected photons along with their corresponding deposited energies in PET detectors. Extension of this method to 3D non-TOF PET systems introduced non-uniform probability distribution (as shown in Figure 2-8 as an example) over the voxels inside the scattering centers.

The non-uniform probability distribution over the voxels inside the scattering center for each single-scatter event is inevitable in the b-LOR approach as the density of b-LOR varies across the area encompassed by the scattering centers. Ignoring photoelectric and multiple Compton scattering inside the imaging object, the annihilation probability for each voxel is a function of the number of *As* lines passing through that voxel, where *A* is the detection point of the unscattered photon and *s* is a point on the scattering surface. Since the number of *As* lines crossing each voxel is a function of the number of possible corresponding scattering centers (*s*), the probability for each voxel can be found by calculating the area of the part of the scattering surface covered by a cone encompassing all *As* lines passing through the voxel. In this argument the effects of the photon's trajectory when hitting PET detectors are ignored. As an example, Figure 4-1 shows the

difference in scattering surface coverage of all *As* lines for two sample pixels inside the scattering centers for a single-scatter event in 2D PET. In this example, the relative number of corresponding scattering centers for the voxels is a function of an angle subtended by the arc comprising the scattering centers. The angle is defined and shown as ω in this figure (the same event as in Figure 2-7 was used in this figure).

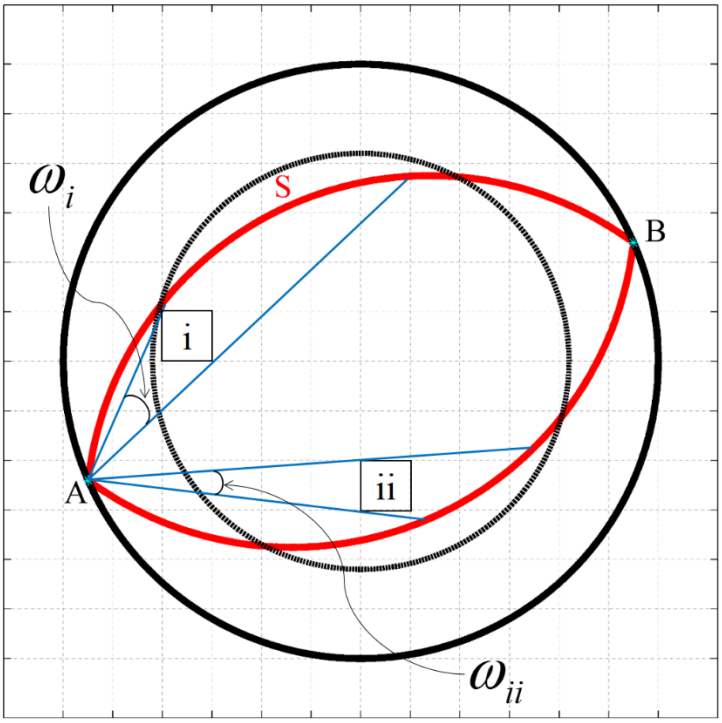

Figure 4-1. Comparing the subtended angles by the arcs comprising the corresponding scattering centers for two pixels for a single-scatter event in 2D PET. The outer solid black circle shows the PET ring and the dotted black circle shows the patient outline. The unscattered photon is detected at *A* while the scattered photon is detected at *B*. ω_i represents the angle covering all possible b-LORs passing through pixel *i*, while ω_{ii} represents the angle covering all possible b-LORs passing through pixel *ii*. Pixels were chosen to be large enough to show the difference clearly.

In this figure, the number of b-LORs (equal to the number of *As* lines) passing through pixel *i* is greater than that for pixel *ii* and the arc subtended by ω_i is greater than the one subtended by ω_{ii}. The number of *As* lines can be related to the inscribed angle of each pixel and the scattering surface, shown as ω_i and ω_{ii}. Although calculation of the probability based on the inscribed angle for each pixel is feasible in 2D PET, it requires more complex and time-consuming mathematical procedures in 3D PET to find the correct probability for each voxel encompassed by the scattering centers. Also, it is vital to consider that the scattering centers should be located inside the pa-

tient outline (assuming that the patient is the only source of scattering). In this work, the same method for sampling b-LORs as explained in (2) was used to estimate the probability based on the chosen b-LORs (a b-LOR per scattering center or each voxel on the scattering surface). However, further investigations are required to verify the accuracy of the generated probability maps. Indeed, the high degree of blurring seen in the images reconstructed with the b-LOR approach is likely to be related to inaccurate mapping of probability because of poor b-LOR sampling. Therefore, more explorations on finding true probability map are required and a more sophisticated mathematical method (or different methods of b-LOR sampling) needs to be found to improve the results of the b-LOR approach. It is worth mentioning that finding the probability maps based on b-LOR sampling has the important advantage of performing independent AC for each b-LOR. Therefore, b-LOR-based approaches are able to adjust the annihilation probability for a spatially variant attenuation map accordingly. In the uniform approach or any other method that is based on direct finding of the annihilation probability for each voxel, however, averaging is inevitable to modify the probability map for a spatially variant attenuation map. The averaging may lead to a compromise in the final generated probability map for each single-scatter event.

Due to a very long reconstruction time, the OPL-EM algorithm was the main reconstruction algorithm in this work. However, convergence to the same image as generated in conventional list-mode reconstructions was not guaranteed. Although changes in the system matrix may greatly affect the convergence rate, quantitative comparisons were only done on the images reconstructed with the same number of events and subsets.

In (69), quantitative changes in the image quality factors were presented when imaging was done in a 2D non-TOF PET system and the reconstruction was done with the aid of the uniform projection/backprojection method with 35% scatter fraction. The authors showed that the CRC for both hot and cold spheres in the NEMA NU-2 phantom has increased by 3 to 11% (absolute change in the CRC) when using the uniform approach. Extension of the uniform approach to 3D in this work showed similar results, as the CRC for all spheres increased by maximum 30%, except for the smallest hot sphere that the CRC decreased by 18% (the percentages here are the absolute changes in the level of CRC to be comparable with the values reported in (69)). However, the change in percentage background variability was not consistent with the results published in (69) for 2D non-TOF PET. The uniform approach in 2D was reported to reduce the percentage

background variability by up to 4% (absolute change), whereas in this work implementation of 3D uniform approach was shown to increase percentage background variability by up to 1.7% (absolute change), due to the inhomogeneity caused by this approach. The most significant inconsistency in extension of the uniform approach to 3D was seen in the measurement of residual activity in the lung insert. While the residual error in the lung insert was decreased by 17% in 2D PET, this approach in 3D PET has significantly increased the residual activity by 17.8% (absolute change) and showed very poor ability to recover contrast for cold areas.

The other investigated approach, b-LOR technique, showed severe blurring effects, most likely as a result of poor probability propagation over the area inside the scattering centers. No improvement in image quality factors was seen in the reconstructed images of standard NEMA image quality phantoms, except a reduction in percentage background variability that was a direct result of blurring (smoothing) images. However, AC seemed to be more accurate in the b-LOR approach than in the uniform approach, since better uniformity was achievable when this technique was used.

The authors in (2) also reported a high degree of blurring when the b-LOR approach was used with poor temporal resolution as shown in Figure 3-31. They also measured spatial full-width half-maximum (FWHM) of a line source in a 20 cm diameter uniform cylinder to be 113 to 128 mm for scatter reconstructed images when temporal resolution was broadened up to 550 ps (compared with 12 mm for the image reconstructed with unscattered coincidences).

Even though quantitative results of standard NEMA phantoms did not turn out to be encouraging, further work is required to investigate possible benefits of scatter reconstruction in 3D non-TOF PET systems. As a beginning step of any future work, we recommend finding the true probability distribution over pixels inside the scattering surface for a single-scatter event, and then find a proper technique of yielding the corresponding probability distribution. For instance, finding a sample probability image for a known single-scatter event in a uniform 2D disk could be done either analytically or by using MC techniques that could be assumed a “reference probability image” for the scattered event and would be helpful to start investigating an image reconstruction technique of finding the probability image. Attenuation correction also needs to be improved if any new scatter reconstruction method is not based on b-LORs, because the calculation

of attenuation correction coefficients based on simple averaging showed overcorrection in the central region of the reconstructed images.

In this project, a novel ray-tracing algorithm for curved lines was also proposed. The ray-tracing algorithm was not implemented in the OPL-EM algorithm used in this work, since the algorithm was finalized towards the end of this work. In order to speed up the reconstruction, implementation of the proposed ray-tracing algorithm is highly recommended for further 3D PET scatter reconstructions, especially if high-resolution reconstructions are required.

Appendix A

The scattering surface in 3D PET may be derived by rotating an arc (as in 2D PET) about the line connecting two detection points (the *AB* line, based on the notation used in Chapter 2). Therefore, in order to derive a mathematical equation for the scattering surface, we first derive the equation of an arc on the scattering surface (this could be any arc) and then extend the formula to the whole scattering surface by rotating the arc about the line. The concept of this rotation is shown in Figure A- 1.

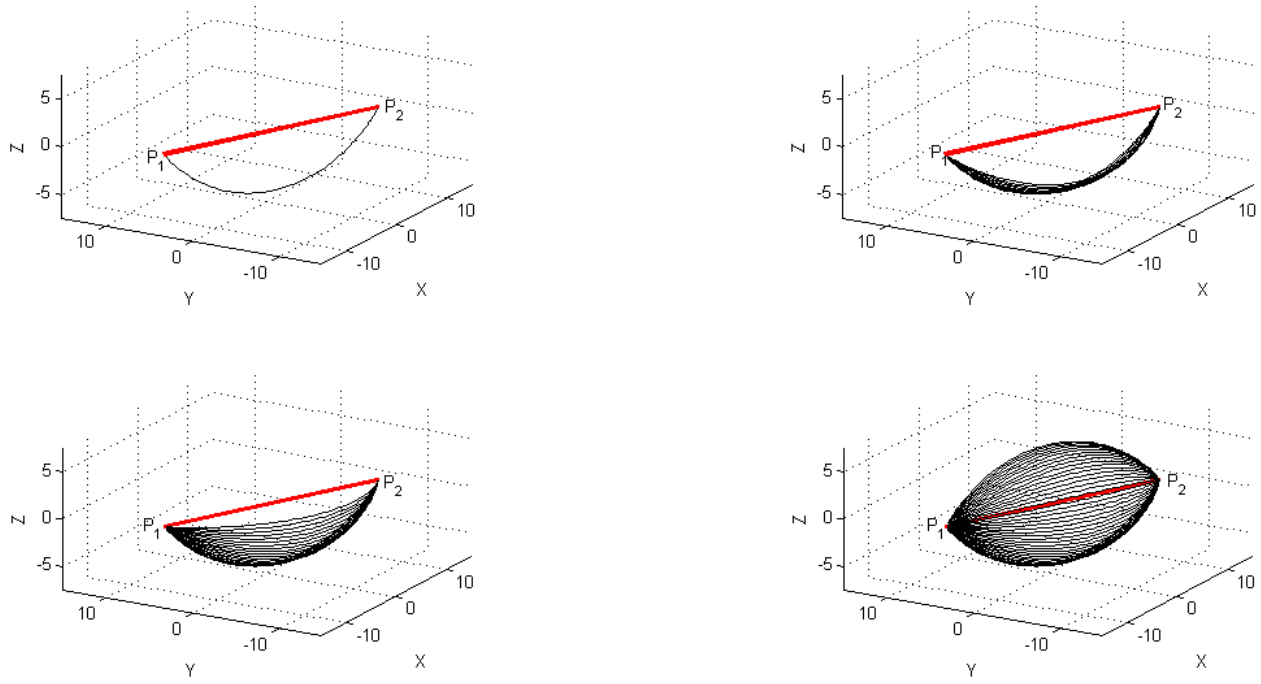

Figure A- 1. Rotation of an arc about the line connecting detection points to derive scattering surface. The left top image shows the arc and other images shows completion of the scattering surface as the arc rotates about the P_1-P_2 line. Note that the points P_1 and P_2 are detection points and analogous to *A* and *B*.

The first step is defining the equation of an arc on the scattering surface. This arc is a segment of a circle and in order to find the equation of the arc, we first derive the equation of the corresponding circle and then constrain the circle to $A - S - B$ arc. Parameters that are to be determined are the radius of the circle, the plane on which the circle lies, and the coordinates of the center of the circle.

Figure A- 2 represents a single-scatter event schematically to define angles and distances required for further derivations. Note that only one side of the scattering arc is shown here, as all other arcs would be generated by rotating this sample arc.

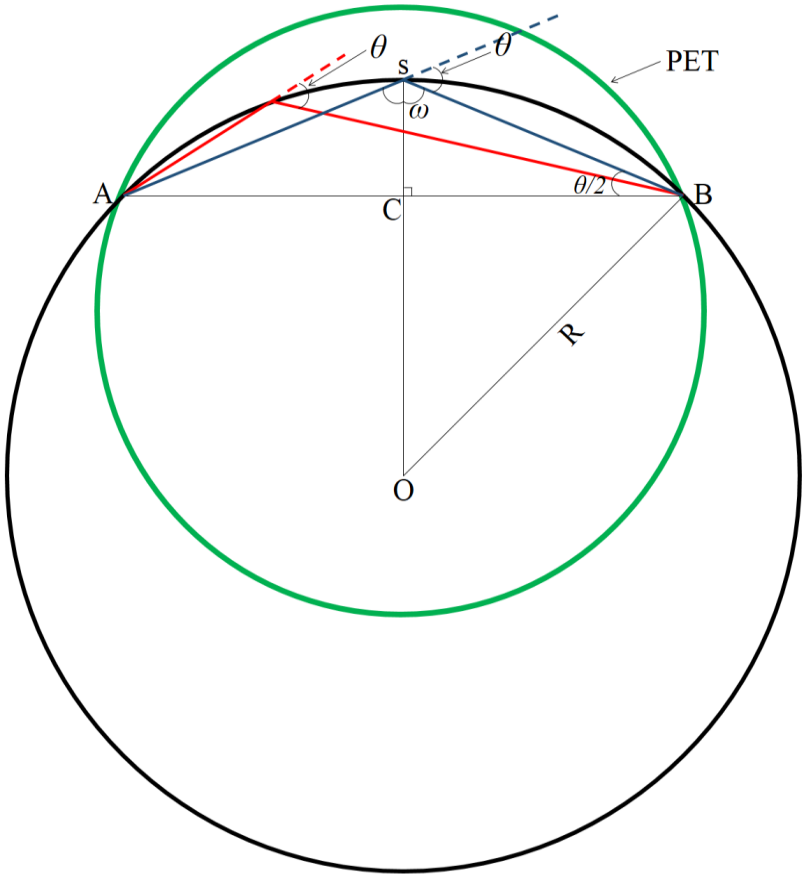

Figure A- 2. Schematic illustration of a single-scatter event. The green circle represents the PET ring and the b-LOR corresponding to the single-scatter event is shown in red. The black circle shows the complete circle of $A - S - B$ arc.

Assuming that the unscattered photon is detected at A and the scattered photon is detected at B with scattering angle of θ, the corresponding b-LOR is shown in red. Any b-LOR, $A - S_i - B$, preserves the angle between $A - S_i$ and $S_i - B$ lines with the same the scattering angle, θ, based on the inscribed angle theorem (80). The scattering point "s" (midway along $A - S_i - B$ arc) is the only point that generates a b-LOR with two equal sides and two equal arcs subtended by the angle ω on both sides of the b-LOR. This b-LOR is shown in blue in Figure A- 2. Therefore, the line AB is divided into two equal parts AC and CB and makes a normal angle between the lines Os and AB, where O is the center of the circle. So the angle ω can be calculated from

$$\omega = \frac{\pi - \theta}{2} \ . \tag{1.1}$$

Therefore, the angle between *sB* and *BC* is equal to $\frac{\theta}{2}$. So length of the line *Cs* can be calculated as

$$Cs = \tan(\frac{\theta}{2}).\mathrm{BC} = \tan(\frac{\theta}{2}).\frac{AB}{2} \ . \tag{1.2}$$

In addition, we have

$$OC = R - Cs \ . \tag{1.3}$$

Replacement of the calculated value for Cs in (1.3) gives us

$$OC = R - \tan(\frac{\theta}{2}).\frac{AB}{2} \ . \tag{1.4}$$

Using the Pythagorean Theorem the relation between the radius of the circle and *OC* can be written as

$$R^2 = OC^2 + BC^2 \ . \tag{1.5}$$

Combining equations (1.4) and (1.5) one can solve the equation for the radius of the circle, *R*, as following

$$\begin{aligned} R^2 &= \left(R - \tan(\frac{\theta}{2}).\frac{AB}{2} \right)^2 + \left(\frac{AB}{2} \right)^2 \\ \therefore R &= \frac{AB}{2\sin(\theta)} \end{aligned} \ . \tag{1.6}$$

It is very important to note that this radius is same for all arcs (comprising scattering surface) on any certain scattering surface. The next step is finding the plane in which the circle lies. Two unit vectors representing directions of two perpendicular axes on the plane is enough for our purpose of defining the circle (i.e. these two unit vectors determine rotation of the circle in 3D with respect to standard XYZ coordinate). It should be considered that the scattering surface is indeed

comprised of an infinite number of arcs (segment of circles) and we are interested in finding the equation for only one of them for the starting point. Therefore, one of the circles can be randomly chosen. In order to do that the first unit vector is to be defined along AB line (which is common to all arcs/circles), namely the unit vector $\vec{p}$. The other unit vector, $\vec{q}$, could be any unit vector that is perpendicular to $\vec{p}$, so it must satisfy

$$\vec{p} \times \vec{q} = 0 \tag{1.7}$$

where × represents a cross product of vectors. Figure A- 3 shows the unit vectors for a sample arc on a scattering surface[6].

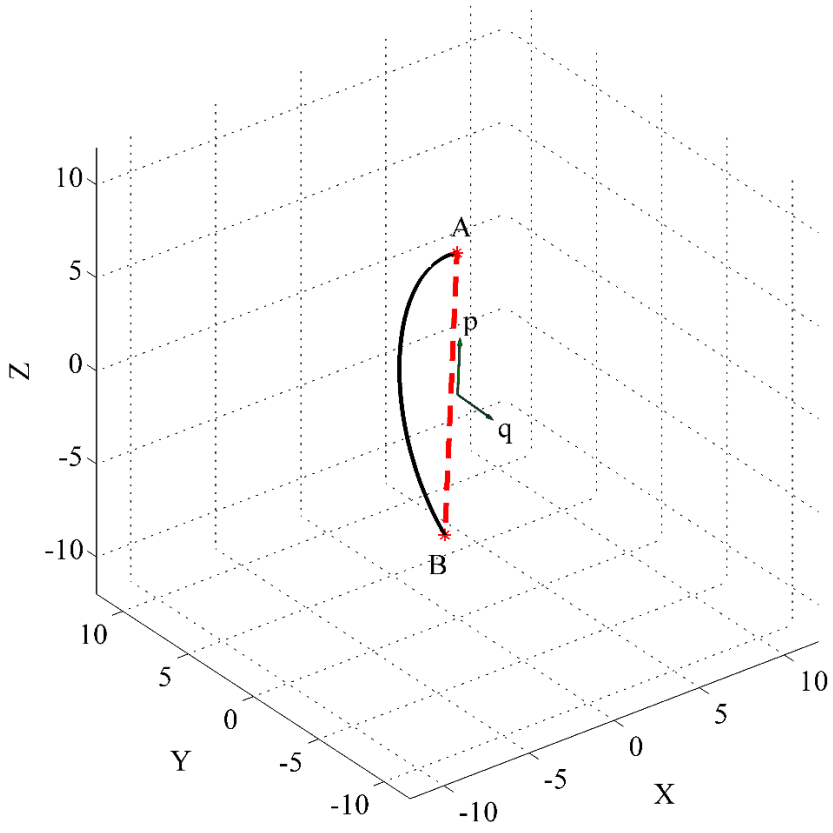

Figure A- 3. Unit vectors $\vec{p}$ and $\vec{q}$ for an arc of a scattering surface. Note that the magnitude of both vectors are exaggerated to clearly show the direction of vectors. Vector $\vec{q}$ shows the direction toward the center of the circle.

[6] Arrow plotting code, written by Eric A. Johnson in 2009 and available at MathWorks file exchange website, was used in production of this graph.

The coordinate of the center of the circle is the last step to complete the data required for the definition of the mathematical equation of the arc. Coordinate of center of the circle varies for different arcs of each scattering surface. However, we are interested in finding the coordinate of the center of the circle in the plane defined by $\vec{p}$ and $\vec{q}$. The center of the circle can be found by shifting the point *C* (midway between two detection points, *A* and *B*) along the direction of the unit vector $\vec{q}$ by the length *OC*. This can be mathematically written as

$$\vec{O} = \vec{C} + OC.\vec{q} \tag{1.8}$$

where *OC* is given by equation (1.4).

Using all this information regarding the circle, the equation of this circle can be defined as

$$\vec{S}(\varphi) = \vec{O} + R.\cos(\varphi).\vec{\mathrm{p}} + \mathrm{R}.\sin(\varphi).\vec{\mathrm{q}} \tag{1.9}$$

where φ is the angle of rotation around the circle and varies between *0* and 2π. In this equation, the vector $\vec{O}$ shifts the coordinate system and the two last terms defines the rotation of the circle with respect to the reference coordinate system and set its radius. Figure A- 4 clarifies the concept of φ.

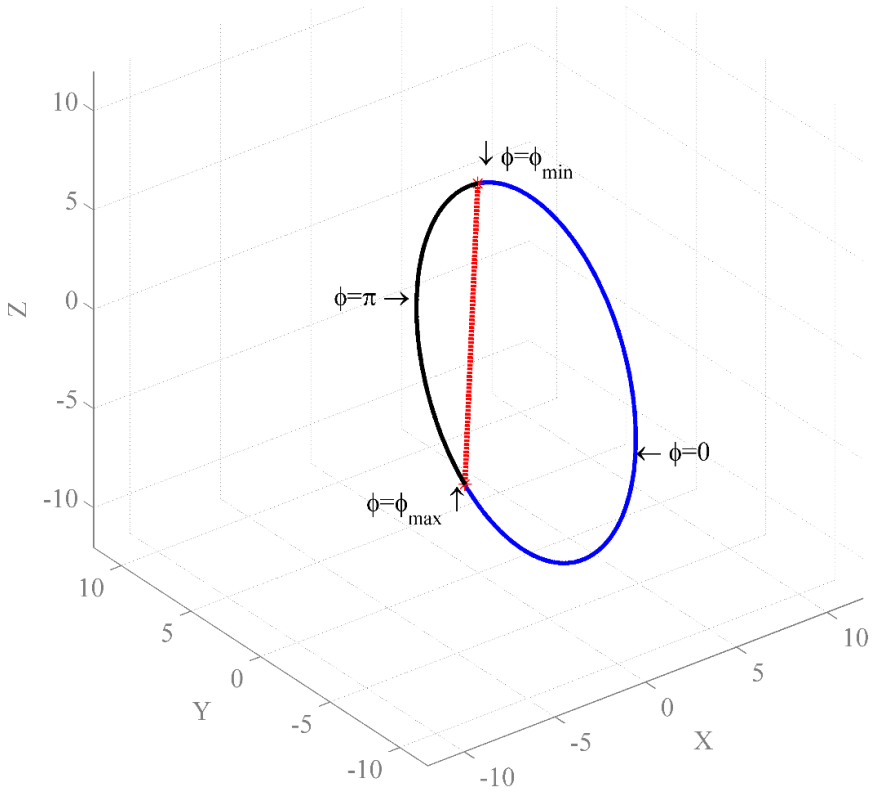

Figure A- 4. Definition of the angle φ for each arc on scattering surface. In this image, the arc is shown in black and the whole circle embracing the arc is shown in blue.

The points of detection, *A* and *B*, are located at two certain angles (φ_{min} and φ_{max}). Constraining the circle to the arc we are interested in could be done by finding these two angles. In other words, a range of φ should be found such that $\varphi_{min} \le \varphi \le \varphi_{max}$. Since φ_{min} and φ_{max} are symmetric with respect to the point $\varphi = \pi$ on the arc, the angle $\angle BOC$ (see Figure A- 2) needs to be calculated. So we can write

$$\begin{aligned} \varphi_{\min} &= \pi - \angle BOC \\ \varphi_{\max} &= \pi + \angle BOC \end{aligned} \quad . \tag{1.10}$$

Since the length of all three sides of the triangle *BOC* were previously calculated, the angle $\angle BOC$ can be simply calculated as

$$\angle BOC = \sin^{-1}\left(\frac{BC}{BO}\right) \quad . \tag{1.11}$$

Replacing *BC* with *AB/2* and *BO* (same as *R*) with equation (1.6) results in the following

$$\angle BOC = \sin^{-1}(\sin(\theta)) = \theta \ . \tag{1.12}$$

This leads to the final step of the definition of each arc by constraining the angle φ. So equation (1.10) can be written as

$$\begin{aligned} \varphi_{\min} &= \pi - \theta \\ \varphi_{\max} &= \pi + \theta \end{aligned} \ . \tag{1.13}$$

The equation for each arc can mathematically be defined exactly same as the equation of each circle embracing the arc (equation (1.9)), however, angle φ is constrained by the φ range defined in equation (1.13).

The final step to define the equation for scattering surface is to rotate the previously defined arc about the *AB* line. This rotation needs to be done in full 2π angle continuously to generate the scattering surface for each single-scatter coincidence. In order to rotate the arc about the *AB* line, a rotation matrix could be defined in a way that rotates the unit vector $\vec{q}$, about the direction of the unit vector $\vec{p}$. The new vector after rotation is still a unit vector, as the rotation does not change the magnitude of the initial vector. Using the general form of rotation about an axis (shown in (81)), the rotation matrix can be defined as

$$\text{Rotation matrix} = \begin{bmatrix} \cos\alpha + p_x^2(1-\cos\alpha) & p_x p_y(1-\cos\alpha) - p_z \sin\alpha & p_x p_z(1-\cos\alpha) + p_y \sin\alpha \\ p_x p_y(1-\cos\alpha) + p_z \sin\alpha & \cos\alpha + p_y^2(1-\cos\alpha) & p_y p_z(1-\cos\alpha) - p_x \sin\alpha \\ p_z p_x(1-\cos\alpha) - p_y \sin\alpha & p_z p_y(1-\cos\alpha) + p_x \sin\alpha & \cos\alpha + p_z^2(1-\cos\alpha) \end{bmatrix} \tag{1.14}$$

where α is the rotation angle, varies between *0* and 2π, and px, py, and pz are the magnitudes of the components of the unit vector $\vec{p}$, such that

$$\vec{p} = p_x\hat{i} + p_y\hat{j} + p_z\hat{k} \ . \tag{1.15}$$

Therefore, for each rotation, a new unit vector $\vec{q}$ is defined as

$$\vec{q} = \vec{q} * (\text{Rotation matrix}) \tag{1.16}$$

where the asterisk shows matrix multiplication operator.

In this manner, the scattering surface can mathematically be defined as

$$\vec{S}(\varphi,\vec{\mathrm{q}}) = \vec{\mathrm{O}} + \mathrm{R}.\cos(\varphi).\vec{\mathrm{p}} + \mathrm{R}.\sin(\varphi).\vec{\mathrm{q}} \tag{1.17}$$

where the angle φ is within the range defined by (1.13) and the vector $\vec{q}$ is all sets of unit vectors that satisfies equation (1.7) and are found by equation (1.16). So, the vector $\vec{S}(\varphi,\vec{\mathrm{q}})$ indicates a point on the scattering surface that is located at angle φ of the arc defined by the unit vector $\vec{q}$.

Appendix B

The general idea behind the ray-tracing algorithm for a curved surface is similar to the idea of Siddon's ray tracing algorithm (71). It starts with modelling the surface mathematically as shown in Appendix A. The assumption of generating a scattering surface by rotating an arc about the line connecting the points of detection is used in this algorithm as well. In this appendix, the algorithm will be explained in detail and pseudo-code of the proposed algorithm will be shown to clarify the steps. The purpose of this algorithm is to find indices of the voxels crossed by the scattering surface for a single-scatter coincidence in a relatively fast manner. Similar to most ray-tracing techniques for a straight line, the length of the segment of the arc within each voxel that it passes through will also be calculated.

In three-dimensional image reconstruction with a matrix size of $N \times N \times N$, normally N^3 voxels are involved in the process of determining which voxels are crossed by a surface. This requires N^3 calculations for each recorded scattered event. The new proposed method first calculates the sides of the rectangular cuboid encompassing the arc inside the reconstruction volume and then intersections of the arc with the planes inside the rectangular cuboid are determined. Therefore, the maximum number of major calculations for each arc (and not for the surface) is reduced to $3N$ rather than N^3. Notations and equations used in this section are consistent with Appendix A, and the algorithm works for scattering angles of less than 90° (corresponds to the photon energy of 255.5 keV and higher).

A pseudo-code is shown below which represents how the proposed algorithm works. In this pseudo-code, the assignment of constant values are shown by an arrow, while variables assigned with an equals sign may change and update with new values in the algorithm. Description of each section is stated in the following followed by the pseudo-code:

- **Line 1 to 2**: The following information should be given as inputs of the function: The position of the coincidence detection, recorded energy of the scattered photon (the energy resolution is assumed to be ideal at all energies), reconstruction matrix size, and the size of FOV along different axes.
- **Line 3 to 23**: Reading the inputs and defining initial values required for the algorithm are done in this part. The scattering angle (θ) can be calculated using equation (1.11) (in

Chapter 1) for a scattered coincidence recorded at *A* and *B*. Unit vectors $\vec{p}$ and $\vec{q}$ are explained in Appendix A. The reconstruction matrix size is $N_X \times N_Y \times N_Z$, and the actual size of the reconstruction volume is FOV_X, FOV_Y, and FOV_Z along *X*, *Y*, and *Z* direction, respectively. Voxel size is shown by *dX*, *dY*, and *dZ*, along *X*, *Y*, and *Z* direction, respectively. In order to rotate the arc efficiently, an optimized degree of rotation is found. To do so, the optimized number of required rotations, such that all voxels crossed by the scattering surface are considered while minimizing repeat processing of voxels, are found. The optimized number of required rotations is calculated by dividing the circumference of a circle with a radius $\tan\left(\frac{\theta}{2}\right)\frac{AB}{2}$ (length of the *Cs* line in Figure A- 2) by the minimum value of *dX*, *dY*, and *dZ* (for 2D reconstructions the rotation angle can be set to π, provided that the two unit vectors $\vec{p}$ and $\vec{q}$ are chosen on *XY* plane). The optimized rotation degree would then be calculated by dividing 2π by this number (line 12). φ_{min} and φ_{max} are defined as explained in Appendix A. The variables in the loop, starting at line 16, are assigned initial values. These variables and their concept are explained in the following. The "*plane*" is a vector containing position of the lateral sides of the reconstruction volume, assuming that the origin of the reference coordinate is at the center of the reconstruction volume.

- **Line 24 to 27**: Each arc is rotated by α using a pre-defined 3×3 rotation matrix ("*rotation_matrix*") until 2π rotation is completed. To do so, one of the unit vectors ($\vec{q}$) is rotated and a new origin (*O*) for the circle is found by using equation (1.8) based on the new origin. The loop in line 27, changes the sides of the reconstruction volume to investigate intersections of the arc with these six planes. This implementation further constrains the angle range ($\varphi_{\min}$ to $\varphi_{\max}$) to a range that is included inside the reconstruction volume (shown by φ'_{min} and φ'_{max}).
- **Line 28 to 83**: For each plane, three possible scenarios will be considered. First, there is no intersection, one intersection, and two intersections between the arc and the plane. Two-intersection scenario may happen for arcs (and not for lines as in Siddon's ray-tracing algorithm). Therefore, each arc might be limited to a segment inside the reconstruction volume, by defining a new φ'_{min} and φ'_{max}. If the arc exits the volume and then returns back, two other variables, namely φ'_{mid} and φ''_{mid}, are introduced such that the

segments between φ'_{min} to φ'_{mid} and φ''_{mid} to φ'_{max} are the parts inside the reconstruction volume and the part between φ'_{mid} to φ''_{mid} is outside the reconstruction volume. In order to evaluate the intersections of each arc with each plane, one should solve the equation (1.9) for solutions within φ_{min} and φ_{max}. The equation might have no, one, or two valid solutions in the specified range (line 29). φ_1 and φ_2 are the possible solutions of the equation (such that φ_1 is the answer with plus discriminant and φ_2 is the answer with minus discriminant, if the equation is solved by conversion into a quadratic equation), which yields $\varphi_2 \geq \varphi_1$. Being in the range of φ_{min} to φ_{max}, changes the flags φ_1*_validity* and φ_2*_validity*. "*j*" is assumed to be a variable that selects different planes (*X*, *Y*, and *Z*) during the whole algorithm. If two intersections happen, various scenarios may occur depending on the position of the detection points and intersections (solutions). Part of the arc can be outside the reconstruction volume and the other part is inside, or two segments of the arc can be inside the reconstruction volume while there is a part in-between which is located outside the reconstruction volume (see Figure B- 1). These scenarios are teased out through lines 36 to 53. Lines 54 to 82, however, evaluates the scenarios of one-intersection only. It is important to note that in the case of one-intersection, the point of intersection should lie on the reconstruction volume to impact on the constraint of the range of φ. The φs corresponding to the found intersections are recorded in sets of φ_X, φ_Y, φ_Z, φ_{mid_X}, φ_{mid_Y}, and φ_{mid_Z}, such that the first column in each set corresponds to the solutions close to the first detection point (*A*), and the second column corresponds to the solutions close to the second detection point (*B*). Figure B- 1 clarifies the concepts of φ_{min}, φ_{max}, φ'_{min}, φ'_{max}, φ'_{mid}, and φ''_{mid}.

- **Line 84 to 87**: If none of the elements in φ_X, φ_Y, φ_Z, φ_{mid_X}, φ_{mid_Y}, and φ_{mid_Z} have updated, then there is certainly no intersection between the arc and the boundaries of the reconstruction volume, so only two states are feasible. First, the arc is completely located outside the reconstruction volume, or the arc is fully encompassed by the reconstruction volume. Therefore, if there is no update in the mentioned variables, one can identify the situation by assessing any point on the arc to determine if the arc is inside or outside the reconstruction volume. If it is outside, then there is no need to continue the algorithm since there is no intersection at all.

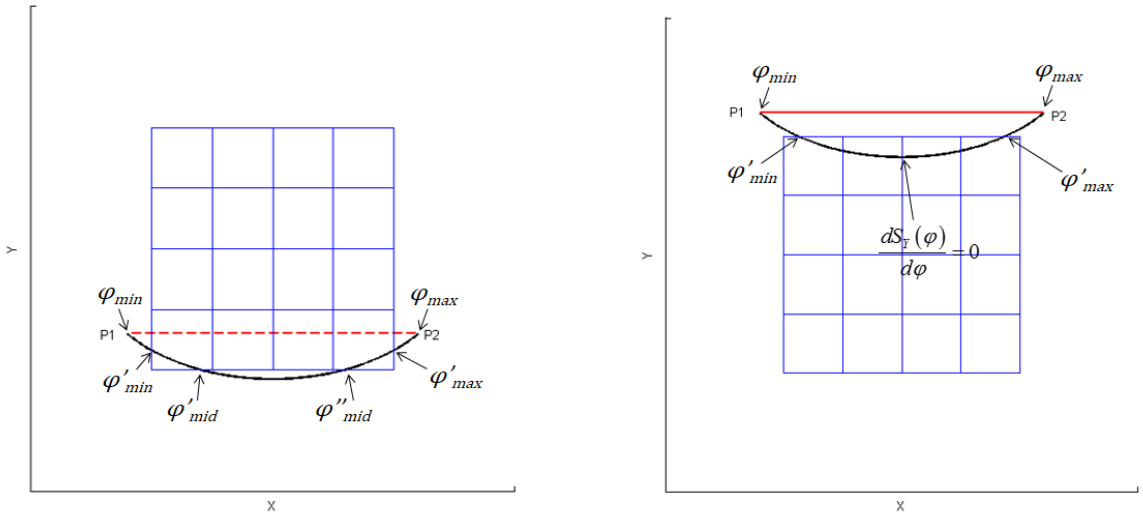

Figure B- 1. The concept of various types of φs defined in the ray-tracing algorithm in two different scenarios. Pixels in the reconstruction area are shown in blue lines. Two points of detection are *P1* and *P2*. The left image contains φ'_{mid} and φ''_{mid} due to the mid-part of the arc being outside the reconstruction area, whereas in the right image there is no exiting and returning back after the ray entered the reconstruction area at φ'_{min}.

- **Line 88 to 91**: New values for minimum, maximum, and middle φs are found and replaced using values found previously in lines 28-83. By updating the new values, only parts of the arcs that are inside the reconstruction volume are considered for the rest of the algorithm. This helps minimizing the number of planes the algorithm needs to deal with.
- **Line 92 to 108**: The rectangular cuboid encompassing the arc is specified in this section. In order to do that, positions of the arc at the points φ'_{min} and φ'_{max} are calculated and compared with the positions where the derivative of the arc ($\frac{dS(\varphi)}{d\varphi}$) are zero (namely, $derivate_{min}$ and $derivate_{max}$) (see Figure B- 1).
- **Line 109 to 125**: A set of φ's along each axis is generated in which information regarding intersections of the arc with planes normal to the axis inside the reconstruction volume is recorded. For instance, a set of solutions (φs) is found and recorded in φ_X, in which each element corresponds to the intersection of the arc with a plane perpendicular to the X-axis. As previously explained, the scenario of two intersections with a plane is possible, which demonstrates exiting and returning back to the plane.

- **Line 126 to 127**: φ'_{min}, φ'_{max}, and the three sets of φs are merged and sorted to form a new set, namely Φ. In this set, each element represents an intersection with a plane, hence the arc has entered to new voxel and therefore the number of elements in this set minus one gives the number of voxels crossed by the arc.
- **Line 128 to end**: The length of the whole arc can be easily calculated since the arc is indeed a fraction of a circle with the radius given by (1.2) ($\text{fraction} = {(\varphi_{\max} - \varphi_{\min})}/{2\pi}$). This is shown in line 128 and is used to calculate the path line (length) in each voxel. The mean value of each two adjacent elements in Φ is calculated and called Φ_{ave}. $S(\Phi_{ave})$ represents the coordinate of a point inside each voxel and using this and a simple transformation (lines 131 to 133) the indices of the corresponding voxel can be found. In addition, the length of the arc in the voxel can be derived by using the length of the whole arc multiplied by the fraction of the arc in the voxel (given by the difference in the two adjacent Φs). Therefore, in each iteration of the final loop, the indices of a new voxel (ind_X, ind_Y, and ind_Z) and length of the arc in that voxel (*path_Length*) are calculated. Once the information of all voxels is gathered, the rotation of the arc will be done and the algorithm starts over from line 18 until 2π rotation is completed.

```
Function Curved_Ray_Tracing{

A, B ← photon detection points;
θ ← scattering angle;
p ← [p_x p_y p_z]; /* unit vector along with the direction of A to B*/
N_x, N_y, N_z ← reconstruction matrix size;
FOV_X, FOV_Y, FOV_Z ← reconstruction cuboid size along different directions;
dX ← FOV_X / N_X;
dY ← FOV_Y / N_Y;
dZ ← FOV_Z / N_Z;
AB ← the distance between the two detection points, A and B;
∝ ← 2 × min(dX, dY, dZ) / (AB×tan(θ/2)); /* Optimized rotation angle */
rotation_matrix ← A 3×3 matrix defined based on equation (1.14) and the calculated ∝;
q = select any random unit vector that satisfies equation (1.7);
φ_min, φ_max ← found based on equation (1.13);
for( j = X and Y and Z){
        φ'_j[0] = φ_min;
        φ'_j[1] = φ_max;
        φ_mid_j[0] = φ_max;
        φ_mid_j[1] = φ_min;
}
/* Side planes of the whole reconstruction volume */
plane ← [-FOV_X/2  FOV_X/2  –FOV_Y/2  FOV_Y/2  - FOV_Z/2  FOV_Z/2];
for( rot = 0; rot < 2π; rot = rot + ∝ ) { /* rotates the arc */
        q = q * rotation_matrix ; /* based on equation (1.16) */
        O = [O_x O_y O_z]; /* center of the circle for each arc - based on equation (1.8) */
        for( i = 0; i < 6; i++){
                j = X or Y or Z if i = 1,2 or i = 3,4 or i = 5,6, respectively;
                φ_1 and φ_2 = solution(s) of equation (1.17) for S_j(φ) = plane[i] ;
                if ( φ_min ≤ φ_1 ≤ φ_max ){
                        set φ_1_validity as true;
                }
                if ( φ_min ≤ φ_2 ≤ φ_max ){
                        set φ_2_validity as true;
                }
                If (both φ_1_validity and φ_2_validity are true){
                        If ( both detection points, A_j and B_j, are within [-FOV_j/2  FOV_j/2]){
                                If ( both S(φ_1) and S(φ_2) are on the reconstruction volume){
                                        φ_mid_j [0] = φ_1 ;
                                        φ_mid_j [1] = φ_2 ;
                                } else if ( S(φ_1) is on the reconstruction volume){
                                        φ'_j[1] = φ_1 ;
                                } else if( S(φ_2) is on the reconstruction volume){
                                        φ'_j[0] = φ_2 ;
                                }
```

```
                    } else {
                        If ( S(φ1) is on the reconstruction volume){
                            φ'j[0] = φ1 ;
                        }
                        If ( S(φ2) is on the reconstruction volume){
                            φ'j[1] = φ2 ;
                        }
                    }
                } else if (φ1_validity is true and S(φ1) is on the reconstruction volume){
                    if (i = 1 or i = 3 or i = 5) {
                        if ( Aj ≥ Bj) {
                            φ'j[0] = φ1 ;
                        } else {
                            φ'j[1] = φ1 ;
                        }
                    } else {
                        if ( Aj ≥ Bj) {
                            φ'j[1] = φ1 ;
                        } else {
                            φ'j[0] = φ1 ;
                        }
                    }
                } else if (φ2_validity is true and S(φ2) is on the reconstruction volume){
                    if (i = 1 or i = 3 or i = 5) {
                        if ( Aj ≥ Bj) {
                            φ'j[0] = φ2 ;
                        } else {
                            φ'j[1] = φ2 ;
                        }
                    } else {
                        if ( Aj ≥ Bj) {
                            φ'j[1] = φ2 ;
                        } else {
                            φ'j[0] = φ2 ;
                        }
                    }
                }
            }
            if ( there is no update in any of the φ's or φ'mid_js and any selected point on the arc is outside
            the reconstruction volume) {
                continue ;
            }
            φ'min ← max(φ'X[0], φ'Y[0], φ'Z[0]) ;
            φ'max ← min(φ'X[1], φ'Y[1], φ'Z[1]) ;
            φ'mid ← min(φ'mid_X[0], φ'mid_Y[0], φ'mid_Z[0]) ;
```

91 $\varphi''_{mid} \leftarrow \max(\varphi'_{mid\_X}[1], \varphi'_{mid\_Y}[1], \varphi'_{mid\_Z}[1])$;
92 for ($j = X, Y, Z$) {
93 if ($A_j \geq B_j$) {
94 $side\_plane_{min\_j} = S(\varphi'_{min})$;
95 $side\_plane_{max\_j} = S(\varphi'_{max})$;
96 } else {
97 $side\_plane_{min\_j} = S(\varphi'_{max})$;
98 $side\_plane_{max\_j} = S(\varphi'_{min})$;
99 }
100 $derivate_{min\_j} \leftarrow \pi + \sin^{-1}(\frac{p_j}{\sqrt{q_j^2 + p_j^2}})$;
101 $derivate_{max\_j} \leftarrow \pi - \sin^{-1}(\frac{p_j}{\sqrt{q_j^2 + p_j^2}})$;
102 if ($\varphi'_{min} \leq derivate_{min\_j} \leq \varphi'_{max}$) {
103 $side\_plane_{min\_j} = \min(side\_plane_{min\_j}, S(derivate_{min\_j}))$;
104 }
105 if ($\varphi'_{min} \leq derivate_{max\_j} \leq \varphi'_{max}$) {
106 $side\_plane_{max\_j} = \max(side\_plane_{max\_j}, S(derivate_{max\_j}))$;
107 }
108 }
109 for($j = X, Y, Z$){
110 $n_j = 0$;
111 for($m = side\_plane_{min\_j}; m \leq side\_plane_{max\_j}; m = m + dj$){
112 φ_1 and φ_2 = solution(s) of equation (1.17) for $S_j(\varphi) = m$;
113 if ($\varphi'_{min} \leq \varphi_1, \varphi_2 \leq \varphi'_{max}$ and $\varphi_1 \leq \varphi'_{mid}$ and $\varphi_2 \geq \varphi''_{mid}$) {
114 $\varphi_j[n_j] \leftarrow \varphi_1$;
115 $\varphi_j[n_j+1] \leftarrow \varphi_2$;
116 $n_j = n_j + 2$;
117 } else if ($\varphi'_{min} \leq \varphi_1 \leq \varphi'_{max}$ and $\varphi''_{mid} \leq \varphi_1 \leq \varphi'_{mid}$) {
118 $\varphi_j[n_j] \leftarrow \varphi_1$;
119 $n_j = n_j + 1$;
120 } else if ($\varphi'_{min} \leq \varphi_2 \leq \varphi'_{max}$ and $\varphi''_{mid} \leq \varphi_2 \leq \varphi'_{mid}$) {
121 $\varphi_j[n_j] \leftarrow \varphi_2$;
122 $n_j = n_j + 1$;
123 }
124 }
125 }
126 $\Phi \leftarrow \{ \varphi'_{min}$, merge and sort$\{ \varphi_X, \varphi_Y, \varphi_Z \}, \varphi'_{max}\}$;
127 $n \leftarrow$ number of elements in the set φ ;
128 $L \leftarrow$ length of the arc $= 2.R.\sin^{-1}(2.\sin(\frac{\theta}{2}))$;
129 for ($i = 0; i < n; i++$) {

130 $\phi_{ave} = \frac{\phi_{i-1} + \phi_i}{2}$;

131 $ind_X = \left\lceil \frac{S_X(\phi_{ave}) + FOV_X/2}{dX} \right\rceil$;

132 $ind_Y = \left\lceil \frac{S_Y(\phi_{ave}) + FOV_Y/2}{dY} \right\rceil$;

133 $ind_z = \left\lceil \frac{S_z(\phi_{ave}) + FOV_z/2}{dZ} \right\rceil$;

134 $path\_\text{Length} = (\phi_i - \phi_{i-1}).\text{L}$;

135 }

136 }

137 end function;

References

1. Sun H, Pistorius S. Evaluation of the Feasibility and Quantitative Accuracy of a Generalized Scatter 2D PET Reconstruction Method. ISRN Biomedical Imaging. 2013;2013:1-11.
2. Conti M, Hong I, Michel C. Reconstruction of scattered and unscattered PET coincidences using TOF and energy information. Phys Med Biol. 2012;57(15):N307-17.
3. Chesler D. Positron tomography and three-dimensional reconstruction technique. Tomographic imaging in nuclear medicine. 1973:176-83.
4. Simon R. Cherry JAS, and Michael E. Phelps. Physics in Nuclear Medicine. 3rd ed: Saunders; 2003.
5. Phelps ME. PET Molecular Imaging and Its Biological Applications: Springer; 2004.
6. Zaidi H, Erwin WD. Quantitative Analysis in Nuclear Medicine Imaging. Journal of Nuclear Medicine. 2007;48(8):1401-.
7. Konik A, Madsen MT, Sunderland JJ. GATE Simulations of Human and Small Animal PET for Determination of Scatter Fraction as a Function of Object Size. IEEE Transactions on Nuclear Science. 2010;57(5):2558-63.
8. Zaidi H, Montandon M-L. Scatter Compensation Techniques in PET. PET Clinics. 2007;2(2):219-34.
9. Ollinger JM. Model-based scatter correction for fully 3D PET. Physics in Medicine and Biology. 1996;41(1):153-76.
10. Bailey DL, Meikle SR. A convolution-subtraction scatter correction method for 3D PET. Physics in Medicine and Biology. 1994;39(3):411-24.
11. Bendriem B, Trebossen R, Frouin V, Syrota A. A PET scatter correction using simultaneous acquisitions with low and high lower energy thresholds. 1993:1779-83.
12. Zaidi H. Scatter modelling and correction strategies in fully 3-D PET. Nuclear medicine communications. 2001;22(11):1181-4.
13. Bentourkia M, Lecomte R. Energy dependence of nonstationary scatter subtraction--restoration in high resolution PET. IEEE transactions on medical imaging. 1999;18(1):66-73.
14. Werling A, Bublitz O, Doll J, Adam L-E, Brix G. Fast implementation of the single scatter simulation algorithm and its use in iterative image reconstruction of PET data. Physics in Medicine and Biology. 2002;47(16):2947-60.
15. Panin VY, Kehren F, Michel C, Casey M. Fully 3-D PET reconstruction with system matrix derived from point source measurements. IEEE transactions on medical imaging. 2006;25(7):907-21.
16. Zaidi H, Koral KF. Scatter modelling and compensation in emission tomography. European journal of nuclear medicine and molecular imaging. 2004;31(5):761-82.
17. Kuhl DE, Edwards RQ, Ricci AR, Yacob RJ, Mich TJ, Alavi A. The Mark IV System for Radionuclide Computed Tomography of the Brain. Radiology. 1976;121(2):405-13.
18. Budinger TF, Derenzo SE, Gullberg GT, Greenberg WL, Huesman RH. Emission computer assisted tomography with single-photon and positron annihilation photon emitters. Journal of computer assisted tomography. 1977;1(1):131-45.
19. Kak AC, Slaney M. Principles of computerized tomographic imaging: Society for Industrial and Applied Mathematics; 2001.
20. Rahmim A, Zaidi H. PET versus SPECT: strengths, limitations and challenges. Nuclear medicine communications. 2008;29(3):193-207.

21. Beyer T, Townsend DW, Brun T, Kinahan PE, Charron M, Roddy R, et al. A combined PET/CT scanner for clinical oncology. Journal of nuclear medicine : official publication, Society of Nuclear Medicine. 2000;41(8):1369-79.
22. Macfarlane DJ, Cotton L, Ackermann RJ, Minn H, Ficaro EP, Shreve PD, et al. Triple-head SPECT with 2-[fluorine-18]fluoro-2-deoxy-D-glucose (FDG): initial evaluation in oncology and comparison with FDG PET. Radiology. 1995;194(2):425-9.
23. Guiberteau FAMaMJ. Essentials of Nuclear Medicine Imaging. 6th ed: ELSEVIER Saunders; 2012.
24. Saha GB. Physics and Radiobiology of Nuclear Medicine: Springer; 2012.
25. Anger HO. Scintillation Camera. Review of Scientific Instruments. 1958;29(1):27-33.
26. Wienhard K, Dahlbom M, Eriksson L, Michel C, Bruckbauer T, Pietrzyk U, et al. The ECAT EXACT HR: performance of a new high resolution positron scanner. Journal of computer assisted tomography. 1994;18(1):110-8.
27. Wang Y, Seidel J, Tsui BM, Vaquero JJ, Pomper MG. Performance evaluation of the GE healthcare eXplore VISTA dual-ring small-animal PET scanner. Journal of nuclear medicine : official publication, Society of Nuclear Medicine. 2006;47(11):1891-900.
28. Badawi RD, Marsden PK, Cronin BF, Sutcliffe JL, Maisey MN. Optimization of noise-equivalent count rates in 3D PET. Phys Med Biol. 1996;41(9):1755-76.
29. Schlemmer HP, Pichler BJ, Schmand M, Burbar Z, Michel C, Ladebeck R, et al. Simultaneous MR/PET imaging of the human brain: feasibility study. Radiology. 2008;248(3):1028-35.
30. Delso G, Furst S, Jakoby B, Ladebeck R, Ganter C, Nekolla SG, et al. Performance measurements of the Siemens mMR integrated whole-body PET/MR scanner. Journal of nuclear medicine : official publication, Society of Nuclear Medicine. 2011;52(12):1914-22.
31. Eugene C. Lin AA. PET and PET/CT: A Clinical Guide. 2nd ed: Thieme; 2009.
32. Turkington TG. Introduction to PET Instrumentation. Journal of Nuclear Medicine Technology. 2001;29(1):4-11.
33. Watson CC. New, faster, image-based scatter correction for 3D PET. IEEE Transactions on Nuclear Science. 2000;47(4):1587-94.
34. Wollenweber SD. Parameterization of a model-based 3-D PET scatter correction. IEEE Transactions on Nuclear Science. 2002;49(3):722-7.
35. Accorsi R, Adam L-E, Werner ME, Karp JS. Optimization of a fully 3D single scatter simulation algorithm for 3D PET. Physics in Medicine and Biology. 2004;49(12):2577-98.
36. Rafecas M, Mosler B, Dietz M, Pogl M, Stamatakis A, McElroy DP, et al. Use of a Monte Carlo-based probability matrix for 3-D iterative reconstruction of MADPET-II data. IEEE Transactions on Nuclear Science. 2004;51(5):2597-605.
37. Chuanyong B, Ling S, Da Silva AJ, Zuo Z. A generalized model for the conversion from ct numbers to linear attenuation coefficients. IEEE Transactions on Nuclear Science. 2003;50(5):1510-5.
38. van Dalen JA, Visser EP, Vogel WV, Corstens FHM, Oyen WJG. Impact of Ge-68/Ga-68-based versus CT-based attenuation correction on PET. Medical Physics. 2007;34(3):889.
39. Chang L-T. A Method for Attenuation Correction in Radionuclide Computed Tomography. IEEE Transactions on Nuclear Science. 1978;25(1):638-43.
40. Mumcuoglu EU, Leahy RM, Cherry SR, Hoffman E. Accurate geometric and physical response modelling for statistical image reconstruction in high resolution PET. 1996;3:1569-73.
41. J. P. Nuclear Medicine Instrumentations: Jones and Bartlett Publishers; 2011.

42. Bailey DL, Townsend DW, Valk PE, Maisey MN. Positron emission tomography: Springer; 2005.
43. Chinn G, Levin CS. A method to reject random coincidences and extract true from multiple coincidences in PET using 3-D detectors. 2008:5249-54.
44. Brasse D, Kinahan PE, Lartizien C, Comtat C, Casey M, Michel C. Correction methods for random coincidences in fully 3D whole-body PET: impact on data and image quality. Journal of nuclear medicine : official publication, Society of Nuclear Medicine. 2005;46(5):859-67.
45. Reader AJ, Julyan PJ, Williams H, Hastings DL, Zweit J. EM Algorithm System Modeling by Image-Space Techniques for PET Reconstruction. IEEE Transactions on Nuclear Science. 2003;50(5):1392-7.
46. Strul D, Bendriem B. Robustness of anatomically guided pixel-by-pixel algorithms for partial volume effect correction in positron emission tomography. Journal of cerebral blood flow and metabolism : official journal of the International Society of Cerebral Blood Flow and Metabolism. 1999;19(5):547-59.
47. Wang H, Fei B. An MR image-guided, voxel-based partial volume correction method for PET images. Med Phys. 2012;39(1):179-95.
48. Qi J. A unified noise analysis for iterative image estimation. Physics in Medicine and Biology. 2003;48(21):3505-19.
49. Erlandsson K, Buvat I, Pretorius PH, Thomas BA, Hutton BF. A review of partial volume correction techniques for emission tomography and their applications in neurology, cardiology and oncology. Phys Med Biol. 2012;57(21):R119-59.
50. Hoetjes N, Velden FP, Hoekstra O, Hoekstra C, Krak N, Lammertsma A, et al. Partial volume correction strategies for quantitative FDG PET in oncology. European journal of nuclear medicine and molecular imaging. 2010;37(9):1679-87.
51. Attix FH. Introduction to radiological physics and radiation dosimetry: John Wiley & Sons; 2008.
52. Saloman EB, Hubbell JH, Scofield JH. X-ray attenuation cross sections for energies 100 eV to 100 keV and elements Z = 1 to Z = 92. Atomic Data and Nuclear Data Tables. 1988;38(1):1-196.
53. Evans RD. The atomic nucleus.
54. Saha GB. Basics of PET Imaging. J Radiol. 2006;87:n719.
55. Bendriem B, Townsend DW. The theory and practice of 3D PET: Springer; 1998.
56. Radon J. On the Determination of Functions from Their Integral Values along Certain Manifolds. IEEE transactions on medical imaging. 1986;5(4):170-6.
57. Liu X, Defrise M, Michel C, Sibomana M, Comtat C, Kinahan P, et al. Exact rebinning methods for three-dimensional PET. IEEE transactions on medical imaging. 1999;18(8):657-64.
58. Daube-Witherspoon ME, Muehllehner G. Treatment of axial data in three-dimensional PET. Journal of nuclear medicine : official publication, Society of Nuclear Medicine. 1987;28(11):1717-24.
59. Defrise M, Kinahan PE, Townsend DW, Michel C, Sibomana M, Newport DF. Exact and approximate rebinning algorithms for 3-D PET data. IEEE transactions on medical imaging. 1997;16(2):145-58.
60. Kaufman L. Implementing and accelerating the em algorithm for positron emission tomography. IEEE transactions on medical imaging. 1987;6(1):37-51.
61. Lange K, Carson R. EM reconstruction algorithms for emission and transmission tomography. Journal of computer assisted tomography. 1984;8(2):306-16.

62. Green PJ. Bayesian reconstructions from emission tomography data using a modified EM algorithm. IEEE transactions on medical imaging. 1990;9(1):84-93.
63. Hudson HM, Larkin RS. Accelerated image reconstruction using ordered subsets of projection data. IEEE transactions on medical imaging. 1994;13(4):601-9.
64. Bruyant PP. Analytic and iterative reconstruction algorithms in SPECT. Journal of Nuclear Medicine. 2002;43(10):1343-58.
65. Barrett HH, White T, Parra LC. List-mode likelihood. JOSA A. 1997;14(11):2914-23.
66. Parra L, Barrett HH. List-mode likelihood: EM algorithm and image quality estimation demonstrated on 2-D PET. Medical Imaging, IEEE Transactions on. 1998;17(2):228-35.
67. Reader AJ, Erlandsson K, Flower MA, Ott RJ. Fast accurate iterative reconstruction for low-statistics positron volume imaging. Physics in medicine and biology. 1998;43(4):835.
68. Reader AJ, Ally S, Bakatselos F, Manavaki R, Walledge RJ, Jeavons AP, et al. One-pass list-mode EM algorithm for high-resolution 3-D PET image reconstruction into large arrays. IEEE Transactions on Nuclear Science. 2002;49(3):693-9.
69. Sun H, Pistorius S, editors. Attenuation correction for a generalized scatter reconstruction algorithm in PET. Nuclear Science Symposium and Medical Imaging Conference (NSS/MIC), 2013 IEEE; 2013.
70. Sun H, Pistorius S. Evaluation of Image Quality Improvements When Adding Patient Outline Constraints into a Generalized Scatter PET Reconstruction Algorithm. ISRN Biomedical Imaging. 2013;2013:1-8.
71. Siddon RL. Fast calculation of the exact radiological path for a three-dimensional CT array. Medical physics. 1985;12(2):252-5.
72. Gillam JE, Solevi P, Oliver JF, Rafecas M. Simulated one-pass list-mode: an approach to on-the-fly system matrix calculation. Phys Med Biol. 2013;58(7):2377-94.
73. Spinks TJ, Miller MP, Bailey DL, Bloomfield PM, Livieratos L, Jones T. The effect of activity outside the direct field of view in a 3D-only whole-body positron tomograph. Physics in Medicine and Biology. 1998;43(4):895-904.
74. Jan S, Santin G, Strul D, Staelens S, Assié K, Autret D, et al. GATE: a simulation toolkit for PET and SPECT. Physics in Medicine and Biology. 2004;49(19):4543-61.
75. Jan S, Benoit D, Becheva E, Carlier T, Cassol F, Descourt P, et al. GATE V6: a major enhancement of the GATE simulation platform enabling modelling of CT and radiotherapy. Phys Med Biol. 2011;56(4):881-901.
76. Constantinescu CC, Mukherjee J. Performance evaluation of an Inveon PET preclinical scanner. Phys Med Biol. 2009;54(9):2885-99.
77. National Electrical Manufacturers Association, NEMA standards publication NU 4-2008: Performance measurements of small animal positron emission tomographs2008.
78. National Electrical Manufacturers Association, NEMA standards publication NU 2-2007: Performance measurements of positron emission tomographs2007.
79. Reinard JC. Communication research statistics: Sage; 2006.
80. Pedoe D. Circles: a mathematical view: Cambridge University Press; 1995.
81. Taylor CJ, Kriegman DJ. Minimization on the Lie group SO (3) and related manifolds. Yale University. 1994.